PROCEEDINGS

OF 13TH INTERNATIONAL CONFERENCE ON COMMUNICATIONS, ELECTROMAGNETICS AND MEDICAL APPLICATIONS (CEMA'18)

Organized by:

FACULTY OF TELECOMMUNICATIONS
TECHNICAL UNIVERSITY OF SOFIA, BULGARIA

NATIONAL TECHNICAL UNIVERSITY OF ATHENS, GREECE,
SCHOOL OF ELECTRICAL AND COMPUTER ENGINEERING

NATIONAL TECHNICAL UNIVERSITY OF ATHENS, GREECE

SCHOOL OF ELECTRICAL AND COMPUTER ENGINEERING

Sofia, Bulgaria
18th – 20th October, 2018

KING 2001, Sofia

Edited by Prof. Dr. Eng. **Dimiter Tz. Dimitrov**

ISSN: 1314-2100

SCOPUS Indexing
http://suggestor.step.scopus.com/progressTracker, ID: 6B4F77263D276412.

Printed in Bulgaria
KING 2001, Sofia

P. Frangos

D. Dimitrov

K. Dimitrov

Dear Colleagues,

It is our privilege to thank all of you for your contributions submitted at 13th regular International Conference on 'Communication, Electromagnetic and Medical Applications' CEMA'18. This is a conference which should help future collaboration in the area of engineering, especially in the area of communication technologies and medical applications. This is an important scientific event not only in Balkan region, but in Europe, also. The International Conference on Communication, Electromagnetism and Medical Applications CEMA'18 is dedicated to all essential aspects of the development of global information and communication technologies, and their impact in medicine, as well. The objective of Conference is to bring together lecturers, researchers and practitioners from different countries, working on the field of communication, electromagnetism, medical applications and computer simulation of electromagnetic field, in order to exchange information and bring new contribution to this important field of engineering design and application in medicine. The Conference will bring you the latest ideas and development of the tools for the above mentioned scientific areas directly from their inventors. The objective of the Conference is also to bring together the academic community, researchers and practitioners working in the field of Communication, Electromagnetic and Medical Applications, not only from all over Europe, but also from America and Asia, in order to exchange information and present new scientific and technical contributions.

Many well known scientists took part in conference preparation as members of International Scientific Committee or/and as reviewers of submitted papers. We would like to thank all of them for their efforts, for their suggestions and advices.

We are extremely grateful to the company INTRACOM Bulgaria for its regular support of our conference.

On behalf of the International Scientific Committee, we would like to wish you successful presentations of your papers, successful discussions and new collaborations for your future scientific investigations.

Engineering and medicine should provide high level of living for all people.

D. Dimitrov
Conference Chairman

P. Frangos
Conference Vice Chairman

K. Dimitrov
Conference Vice Chairman

INTERNATIONAL SCIENTIFIC COMMITTEE

Chairman:

D. TZ. DIMITROV, Technical University of Sofia, Bulgaria

Vice Chairmen:

P. FRANGOS, National Technical University of Athens, Greece
K. L. DIMITROV, Technical University of Sofia, Bulgaria

Members

N. AMPILOVA,	University of Petersburg, Russia
T. AVOYAGI,	Tokyo Institute of Technology, Japan
A. BEKJARSKY,	Technical University of Sofia, Bulgaria
E. BOEMO,	University Authonoma, Barcelona, Spain
R. BRUZGIENE,	Kaunas University of Technology, Lithuania
N. DIB,	Jordan University of Science and Technology, Aman, Jordan
V. DUMBRAVA,	Kaunas University of Technology, Litvania
N. ESCUDEIRO,	ISEP, Porto, Portugal
E. GAGO-RIBAS,	University of Oviedo, Spain
V. GEORGIEVA,	Technical University of Sofia, Bulgaria
G. GOUSSETIS,	Heriot - Watt University, United Kingdom
S. V.HOEYE,	University of Oviedo, Spain
I. ILIEV,	Technical University of Sofia, Bulgaria
F. KLETT,	Franhofer Institute, Ilmenau, Germany
G. KLIROS,	Hellenic Air-Force Academy, Athens, Greece
V. KUKENSKA,	Technical University of Gabrovo, Bulgaria
L. LUBIH,	Technical University of Sofia, Bulgaria
G. MALLET,	University "Sophia Antipolis", Nice, France
G. MATSOPOULOS,	National Technical University of Athens, Greece
M. MARTINS,	Academia Militar da Amadora, DCEE, Portugal
M.– J. MORALES-GONZALES,	University of Valladolid, Spain
L. NARBUTAITE,	Kaunas University of Technology, Lithuania
K. NIKITA,	National Technical University of Athens, Greece
M. NIKOLOVA,	High Naval School, Varna, Bulgaria
A. PANAGOPOULOS,	National Technical University of Athens, Greece
J. PETROVSKA,	Medical University of Sofia, Bulgaria
H. ROTH,	University of Siegen, Germany
S. SAUTBEKOV,	Euroasian University, Astana, Kazakhstan
A. SAVOV,	Medical University of Sofia, Bulgaria
S. SAVOV,	Technical University of Varna, Bulgaria
H.-P. SCHADE,	Technical University of Ilmenau, Germany
I. SOLOVIEV,	University of St. Petersburg, Russia
L. SONG,	Technical University of Harbin, China
G. STAMATAKOS,	National Technical University of Athens, Greece
A. USHEVA,	University of Boston, USA
R. VERDONE,	University of Bologna, Italy

REVIEWERS

BALZANO, Q.	University of Maryland, USA
BEHARI, J.	Jawaharlal Nehru University ,New Delhi, India
BOEMO, E.	Technical University of Madrid, Spain
DIMITROV, D.	Technical University of Sofia, Bulgaria
DONTSCHEWA, M.	University of Applied Sciences, Dorbirn, Austria
GOUSSETIS, G.	Heriot - Watt University, United Kingdom
MALLET, G.	University "Sophia Antipolis", Nice, France
PETROVSKA, J.	Medical University of Sofia, Bulgaria
PRATO, F.	University of Western Ontario, Canada
ROTH, H.	University of Siegen, Germany
SAVOV, A.	Medical University of Sofia, Bulgaria
SCHADE, H-P.	Technical University of Ilmenau, Germany
SONG, L.	Technical University of Harbin, China
USHEVA, A.	University of Boston, USA

REGISTRATION

October, 18th, 09h 30min – 16h

The conference registration desk will be at:
Building of Library, fourth floor
Technical University of Sofia, Bulgaria

CONFERENCE PROGRAM

18th October

OPENING CEREMONY

10h – 10h 30min
The conference registration desk will be at:
Building of Library, fourth floor
Technical University of Sofia, Bulgaria

SCIENTIFIC PROGRAM

18th October

FIRST SESSION

10h 30min – 12h
Building of Library, fourth floor
Technical University of Sofia, Bulgaria

Chairman: Prof. N. Ampilova, St. Petersburg State University, St. Petersburg, Russia

---

1. **SEA STATE CHARACTERIZATION USING EXPERIMENTAL ONE – DIMENSIONAL RADAR SIGNATURES AT X – BAND AND FRACTAL TECHNIQUES**
   G. Pouraimis[1], A. Kotopoulis[1], Th. Lymperopoulos[1], N. Ampilova[2], I. Soloviev[2], E. Kallitsis[1] and P. Frangos[1, 1]School of Electrical and Computing Engineering, National Technical University of Athens, [2]St. Petersburg State University, Math. and Mech. Faculty.

2. **RADIATION OF VERTICAL DIPOLE ANTENNAS OVER FLAT AND LOSSY TERRAIN: A NOVEL EFFICIENT METHOD FOR THE ACCURATE NUMERICAL CALCULATION OF THE SOMMERFELD INTEGRALS IN THE SPECTRAL DOMAIN**
   S. Bourgiotis[1], L. Dimopoulos[1], Th. Lymperopoulos[1], A. Chrysostomou[1], S. Sautbekov[2], P. Frangos[1], [1]School of Electrical and Computer Engineering, National Technical University of Athens, [2]Al-Farabi Kazakh National University, Department of Physics, Almaty, Kazakshtan

3. **APPLICATION OF THE METHOD OF AUXILIARY SOURCES (MAS) TO THE ANALYSIS OF ELECTROMAGNETIC SCATTERING FROM DIELECTRIC SURFACES WITH CURVED WEDGES,**
   Vissarion G. Iatropoulos, Minodora-Tatiani Anastasiadou and Hristos T. Anastassiu, Department of Informatics Engineering, Technological Educational Institute (TEI) of Central Macedonia, Greece

4. **LOCALIZATION OF A SINGLE SOUND SOURCE FROM BINAURAL RECORDINGS**,
   Gergana Vasileva, Ivo R. Draganov, Radiocommunications and Videotechnologies Dept., Faculty of Telecommunications, Technical University of Sofia, Bulgaria

5. **AUTOMATED INFORMATION SYSTEM FOR EVALUATION THE STABILITY OF THE SHIP**,
   Emilia Koleva, Milena Lefterova, Mariya Nikolova,"N. Y. Vaptsarov" Naval Academy, Varna, Bulgaria

Lunch

12h – 13h30min

SECOND SESSION

13h30min – 15h
Building of Library, fourth floor
Technical University of Sofia, Bulgaria

Chairman: Prof. K. Dimitrov, Faculty of Telecommunication, Technical University of Sofia, Bulgaria

---

1. **DETECTING CONTOURS PATHOLOGICAL FORMS IN COLONOSCOPY IMAGES USING A HYBRID METHOD,**
   Veska Georgieva, Plamen Petrov, Technical University of Sofia, Bulgaria, Szilvia Nagy, Brigita Sziová, Széchenyi István University, Hungary

2. **GUI FOR SPLEEN SEGMENTATION FROM ABDOMINAL MRI SEQUENCES,**
   Antonia Mihaylova, Technical University of Sofia, Bulgaria

3. **THE DIGITAL IMAGE CLASSIFICATIONBASED ON CALCULATION OF RENYI DIVERGENCE**,
   V. D. Sergeev, Saint-Petersburg State University, Math. & Mech. faculty, Russia

4. **OBJECT RECOGNITION VIA CCTV BY NEURAL NETWORK USING,**
   Liljana Emilova Docheva, Ivo Nikolaev Dochev, Stoycho Velizarov Manev, Department of Radio communications and Video technologies, Faculty of Telecommunications, Technical University of Sofia, Bulgaria

5. **DEVELOPMENT OF AUDIO – VISUAL MODEL AND ALGORITHM FOR HUMAN CONTROL OF MOBILE ROBOT MOTION WITH COMBINED RECGNITION OF VOICE AND GESTURE COMMANDS**,
   Snezhana Pleshkova, Zahari Zahariev, Aleksander Bekiarski, Shima Dehkharghani, Technical University of Sofia, Bulgaria

Break
15h – 15h30min

THIRD SESSION

15h30min – 17h
Building of Library, fourth floor
Technical University of Sofia, Bulgaria

Chairman: Prof. P. Frangos, School of Electrical and Computing Engineering, National Technical University of Athens, Greece

---

1. **A COMPARATIVE ANALYSIS OF THERMOPILE SENSORS FOR BIOMEDICAL APPLICATIONS,**
   Kalin Dimitrov, Lyubomir Laskov, Faculty of Telecommunications, Technical University of Sofia, Bulgaria

2. **ADVANCED SIGNAL PROCESSING METHODS FOR ANALYSIS OF HIGH DYNAMIC RANGE ACOUSTIC PHENOMENA,**
   T. Trifonov[1,2], I. Simeonov[1], N. Yordanov [1] [1]Vasil Levski National Military University, Veliko Tarnovo, Bulgaria, [2]St. Cyril and St. Methodius University of Veliko Tarnovo, Department of Computer Systems and Technologies, Veliko Tarnovo, Bulgaria

3. **QOS-ENABLED MQTT IMPACT ON RESILIENT COMMUNICATION IN INTERNET OF THINGS SYSTEMS,**
   Paulina Kuojaite[1], Rasa Bruzgiene[1], Lina Narbutaite[2], Tomas Adomkus[3], [1]Faculty of Electrical and Electronics Engineering, Department of Electronics Engineering, [2]Faculty of Informatics, Department of Software Engineering, [3]Faculty of Informatics, Department of Computer Sciences, [1,2,3]Kaunas University of Technology, Lithuania

4. **ON THE ESTIMATION OF MAGNETOTHERAPY CURATIVE SESSIONS EFFECTS**,
   N. Ampilova, F. Uvarichev, I. Soloviev, St. Petersburg State University, Comp. Sci. Dept.

CLOSING CONFERENCE SESSIONS

17h – 17h 30min
Building of Library, fourth floor
Technical University of Sofia, Bulgaria

SOCIAL PROGRAM

- **Conference Dinner**, 19h, October, 18th
- **Trip**, October, 19th.

  More information regarding Conference dinner and trip will be provided during the first day of the Conference (October 18th)

CONTACT US:

http://rcvt.tu-sofia.bg/CEMA/eth.html

Prof. Dr. Dimiter Dimitrov

Faculty of Telecommunication
Technical University of Sofia
8, Kliment Ohridsky str.
1756 Sofia, Bulgaria
Phone:++359 2 9652278
Fax: ++359 2 9652278
E-mail: dcd@tu-sofia.bg

Prof. P. Frangos

National Technical University of Athens
School of Electrical and Computer Engineering
9, Iroon Polytechniou Str. ,
157 73 Zografou, Athens, Greece
Phone : 00 30 210 772 3694
Fax : 00 30 210 772 2281
E-mail : pfrangos@central.ntua.gr

TABLE OF CONTENTS

SEA STATE CHARACTERIZATION USING EXPERIMENTAL ONE – DIMENSIONAL RADAR SIGNATURES AT X – BAND AND FRACTAL TECHNIQUES

G. Pouraimis[1], A. Kotopoulis[1], Th. Lymperopoulos[1], N. Ampilova[2], I. Soloviev[2], E. Kallitsis[1] and P. Frangos[1]

[1]School of Electrical and Computing Engineering, National Technical University of Athens, 9, Iroon Polytechniou Str., 157 73 Zografou, Athens, Greece

Tel. : +30 210 772 3694; FAX : +30 210 772 2281; e-mail : pfrangos@central.ntua.gr
[2]St. Petersburg State University, Math. and Mech. Faculty,

e-mail : n.ampilova@spbu.ru , i.soloviev@spbu.ru

Abstract

This paper presents a novel method of sea state characterization using the 'Mean Fractal Length (MFL)' criterion which is applied to experimental Synthetic Aperture Radar (SAR) one – dimensional signatures (range profiles), provided to our research group by SET 215 Working Group on 'SAR radar techniques'. The MFL criterion uses the 'blanket' technique to provide sea state characterization from SAR radar range profiles. It is based on the calculation of the area of a 'blanket', corresponding to the range profile under examination, and then on the calculation of the corresponding 'Fractal Length' of the range profile. The main idea concerning this proposed technique is the fact that SAR radar range profiles corresponding to different sea states yield different values of 'Fractal Length, FL', namely 'turbulent sea' yields range profiles with larger FL, because of the more 'anomalous behavior' of the range profiles in that case. As a result, a sea state characterization technique for two different sea states (turbulent and calm sea) is presented in this paper.

1. INTRODUCTION

Fractals can describe an unlimited number of complex patterns that resemble in different scales and are used as a mathematical tool for a variety of applications, such as image analysis and sorting, applied electromagnetism, etc. [1]. The indistinguishable structure on different scales is a basic feature of fractals. Accordingly, fractals can illustrate a certain very strong form of geometric complexity across multiple data sets as well as SAR images. Synthetic Aperture Radar (SAR) images can be considered as fractals for a certain range of magnification [1]. In addition, fractal objects have unique properties and features that may be related to their geometric structure [2].

The main objective of this paper is to examine the sea state characterization problem using the 'Mean Fractal Length' (MFL). The MFL criterion is a 'product' of the 'Modified Fractal Signature' (MFS) method, which has been applied in the past to real Synthetic Aperture Radar (SAR) images, using the 'blanket' technique, in order to provide useful information about SAR image classification, as reported by Malamou et. al. [1].

This paper uses the recorded sea clutter radar data which were collected during the 'NEMO 2014' trials in Taranto, Italy, using FFI (i.e. 'Norwegian Institute of Defense', Oslo, Norway) PicoSAR X-band radar as input to a specific SET Working Group. The experiment took place in the Taranto bay in southern Italy on 23 and 24 September 2014. The first day the weather was quite windy, thus creating a rather turbulent sea, in comparison with the second day, during which the sea surface was almost calm.

2. PROBLEM GEOMETRY, EXPERIMENTAL 1D RADAR DATA SETS, THE 'STRIP' FRACTAL TECHNIQUE AND PRELIMINARY NUMERICAL RESULTS USING THE 'STRIP' TECHNIQUE

The geometry of the sea state characterization problem is shown in Fig. 1. Here, a helicopter (with PicoSAR radar inside) rises vertically, while maintaining its steady position (latitude and longitude), and transmits electromagnetic (EM) radar pulses towards the sea. In addition, it records the azimuth angle with high sampling density in grazing angle.

During the experiment, performed by FFI in September 2014 (NEMO trials), the helicopter kept low vertical velocity and negligible horizontal velocity (helicopter movement from down to up). The first day (23/9/2014), the wind speed was reported in

the range of 10 to 12 m/s (rather high wind speed) and the helicopter pilot kept the direction of the antenna beam up-wind (i.e. direction of radar pulses - EM wave propagation in the opposite direction of the wind speed), within a 20° window in the horizontal (azimuthal) direction, as grazing angles θ_g (see Fig. 1) scanned from 3° to 55°. The time of the full grazing angle span was around 5 minutes.

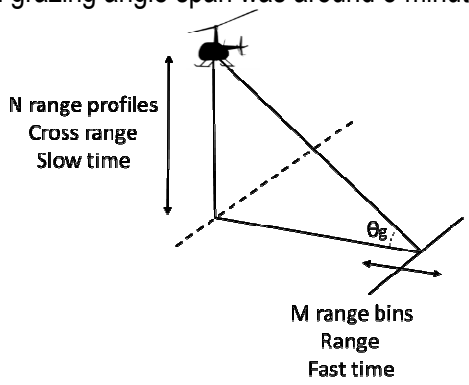

Figure 1. Geometry of sea state characterization problem, where the helicopter rises vertically transmitting PicoSAR radar electromagnetic (EM) pulses towards the sea

During the second day (24/9/2014), the wind speed was very low (1-2 m/s, which sometimes died out locally) and the range of grazing angles was from 4° to 54° with a slight drift in azimuth pointing angle of the bore sight of no more than 20°.

Fig. 2 shows representative radar range profiles (1D radar signatures) from 'Day 1' (23-9-2014, 'turbulent sea') at grazing angles of $\theta_g = 35^0$ (figure on the top), and from 'Day 2' (24-9-2014, 'calm sea'), for $\theta_g = 35^0$ (bottom figure).

As follows from Fig. 2 (i) on 23 September 2014 the grazing angle was chosen, from 35º to 36º (for 'turbulent sea'), with corresponding maximum value of approximately 15,000.

Additionally, as it can be seen from Fig. 2 (ii), during the following day of 24 September 2014, for the same grazing angles of 35º to 36º, but for 'calm sea' in this case, the approximate maximum value of the range profiles was approximately equal to 1,600.

The 'Mean Fractal Length (MFL)' criterion was used for the sea state determination, which computes the mean of the 'Fractal Length' of the range profile, for turbulent and calm sea, and at grazing angles of 35° and 40° as well. The MFL is given by eq. (1):

$$< FL >= \frac{1}{N}\sum_{n=1}^{N}(FL)_n \qquad (1)$$

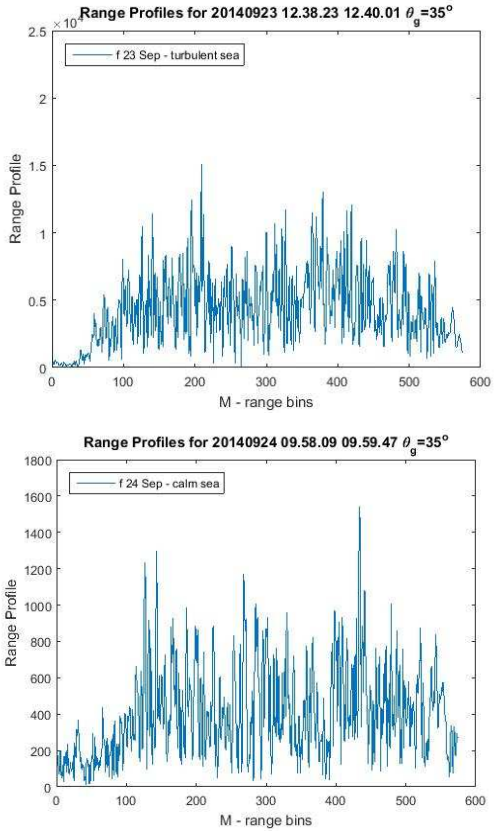

Figure 2. Representative PicoSAR radar range profiles: (i) Day 1, (turbulent sea) grazing angle θg = 35^0, (ii) Similarly, but for Day 2 (calm sea)

In this Section, it remains to explain how the 'Fractal Length, FL' is calculated. For this reason, the 'blanket technique' will be described briefly [1], [3].

First, for measuring the lengths of irregular curves, S. Peleg et. al. used a 'Mandelbrot method' [3]. In this example, the curve is shown at Fig. 3 (inner curve, out of 3 curves). Considering all points with distances to this curve no more than ε, a strip of width 2ε is formed. This strip creates a 'strip' (2D case examined here, or 'blanket', in the corresponding 3D case), above and below the inner curve, as shown at Fig. 3, which means that all points at distance ε cover the curve within a 'strip' of thickness 2ε. According to S. Peleg et. al. [3], the 'upper' and 'lower' curves of the 'strip' are provided by the following equations:

$$\boldsymbol{u_\varepsilon(i,j) = max\{u_{\varepsilon-1}(i,j) + 1, \max_{|(m,n)-(i,j)|\le 1} u_{\varepsilon-1}(m,n)\}} \qquad (2)$$

$$\boldsymbol{b_\varepsilon(i,j) = max\{b_{\varepsilon-1}(i,j) - 1, \max_{|(m,n)-(i,j)|\le 1} b_{\varepsilon-1}(m,n)\}} \qquad (3)$$

Eq. (2) ensures that the new upper curve u_ε is higher at least by one than $u_{\varepsilon-1}$, and also at a dis-

tance of at least one of $u_{\varepsilon-1}$ in the horizontal and vertical directions [3].

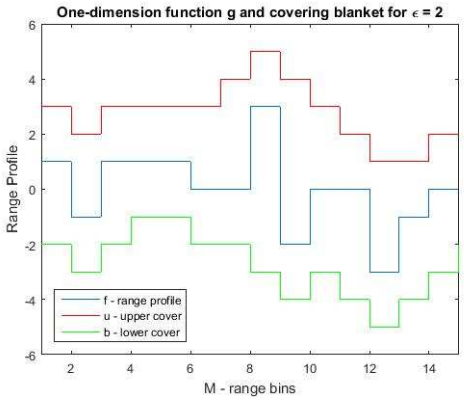

Figure 3. One-dimensional (1D) function g and the 'upper' and 'lower' curves of the strip for iteration number ε=2.

The 'area' υ_ε of the 'strip' is calculated from u_ε and b_ε by :

$$v_\varepsilon = \sum_{i.j} (u_\varepsilon(i,j) - b_\varepsilon(i,j)) \qquad (4)$$

The 'fractal length, FL' $L(\varepsilon)$ of the curve is approximately calculated through the subtraction of the strip areas of radii ε and ε-1 divided by 2, or from the area of the 'strip' divided by 2ε, as shown below :

$$L_\varepsilon = \frac{(A_\varepsilon - A_{\varepsilon-1})}{2} \qquad (5)$$

$$L_\varepsilon = \frac{A_\varepsilon}{2\varepsilon} \qquad (6)$$

The fractal length $L(\varepsilon)$ as a function of the 'resolution' ε (ε=1 corresponds to 'full resolution), for the curve of Fig. 3 [3], is shown at Fig. 4, on a log-log scale (here the plot consists of straight segments, because the curve is ideally fractal. In contrast, the curve would not have to be straight for non - fractal curves [3]).

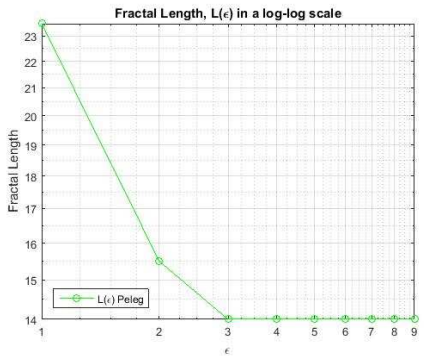

Figure 4. Fractal length L(ε) as a function of resolution ε (ε=1) corresponds to 'full resolution') in log-log scale for one-dimensional (1D) curve g.

In addition, previous research by Malamou et. al. [1], regarding use of the 'Modified Fractal Signature (MFS)' method, which was applied to real Synthetic Aperture Radar (SAR) images, used the 'blanket' technique (in 3D case), to provide useful information for SAR image classification.

The 'Fractal Length technique', as explained above, is now applied to the recorded radar raw data which were provided to us by SET 215 Working Group, as explained above.

The 'upper and lower curves' of the 'radar range profiles' using the Modified Fractal Signature (MFS) method, are indicatively shown at Fig. 5, for different iterations ε = 1 and 20 of the original range profile (here for grazing angle θg = 35°). Note that throughout this Section, ε represents the 'iteration number', or, equivalently, the 'resolution'.

Examining the plots at Fig. 5 it is obvious that as the number of iteration ε increases (i.e. 'resolution' becomes poorer), the covering blankets become more 'extensive'.

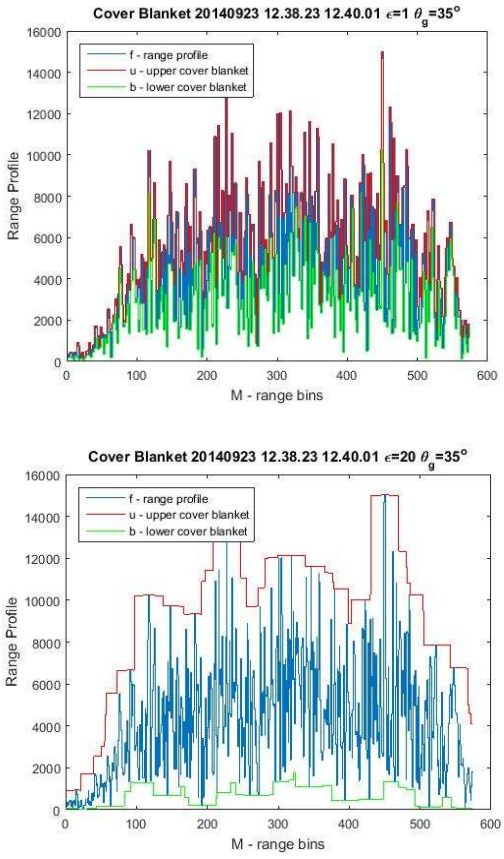

Figure 5. Upper and lower curves for a 'radar range profile' provided to us by FFI, for different scale (iteration) of the MFS method, ε = 1 and 20 respectively (radar range profile used here was for grazing angle θg =35°).

3. SEA STATE CHARACTERIZATION RESULTS USING THE 'MEAN FRACTAL LENGTH (MFL)' CRITERION

The 'Mean Fractal Length (MFL)' criterion is used for characterization of the sea state. The 'Mean Fractal Length (MFL)' Criterion computes the mean of the Fractal Length of the range profile, according to eq. (1).Then, numerical calculations similar to the above were performed, and the results are presented at Fig. 6.

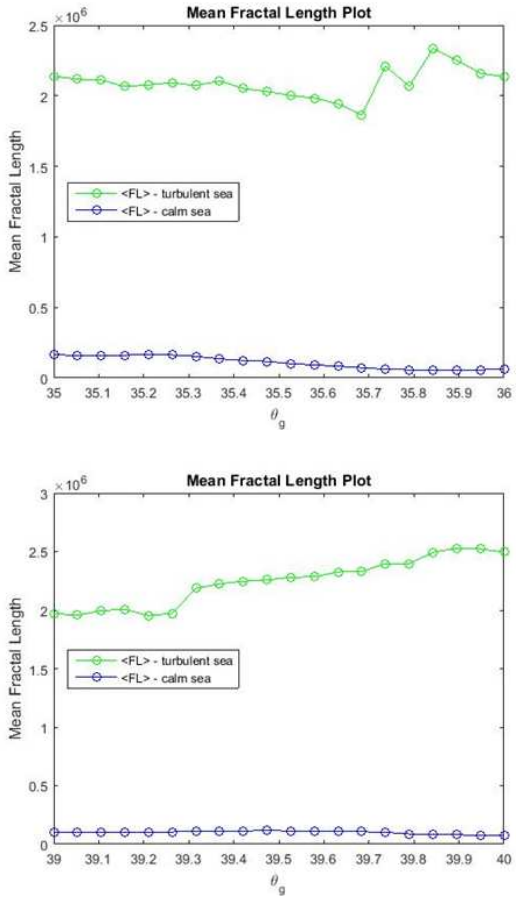

Figure 6. 'Mean Fractal length' (MFL) values of radar range profiles at different sea state [turbulent (green lines) and calm sea (blue lines)], for grazing angles (i) 35° to 36° (upper figure) and (ii) 39° to 40° (lower figure).

The results of Fig. 6 show that the MFL values of radar range profiles during the turbulent sea state are significantly larger than the corresponding values at calm sea, as shown at Table I.

Table I. MFL values results for different sea states

Date / MFL	23 Sep 2014 (turbulent sea)	24 Sep 2014 (calm sea)
θg= 35°- 36°	2,090,761	110,631.9
θg= 39°- 40°	2,241,509	100,038.9

Finally, and similarly to above, the sea state index (SSI) is calculated once again for this case. Once again, the 'MFL value' for calm sea was chosen as the reference value. The corresponding results for SSI are shown at Table II, below.

Table II. MFL sea state index (SSI) for different grazing angles

	SSI
θg = 35°- 36°	18.89
θg = 39°- 40°	22.40

Concluding with the above criterion for sea state characterization by using radar range profiles (1D radar signatures), it is evident, from physical intuition that the 'mean fractal length', (MFL) is a reliable criterion for 'real time' sea state characterization, in practical circumstances (because of the presence of additive noise in 'real life' scenarios, etc.).

4. CONCLUSIONS

To summarize, for the characterization of the sea state from experimental 1D radar signatures (range profiles), the 'mean fractal length' (MFL) criterion was used. The corresponding recorded sea clutter radar data were collected during the 'NEMO 2014' trials in Taranto, Italy, 23-24/9/2014. An X-band PicoSAR airborne radar was used for that purpose by FFI (i.e. 'Norwegian Institute of Defense', Oslo, Norway)

The above criterion was found to be suitable and it can be used for sea state characterization. Other criteria for sea state determination, which are, however, of less importance than that described above, will also be presented during our presentation at the Conference.

5. FUTURE RESEARCH

In our future related research, we intend to concentrate on more accurate sea state characterization using a *variety* of sea surface radar range profiles, i.e. in a variety of sea state conditions.

Finally, sea state characterization using fractal characteristics of SAR radar *images* (i.e. 2D SAR radar signatures) may be used, instead of 1D radar signatures, examined here.

6. ACKNOWLEDGMENT

The authors (GP, AK and PF) would like to thank SET-215 Working Group, and FFI Institute (i.e. 'Norwegian Institute of Defense', Oslo, Norway), in particular, for providing to us the real recorded sea clutter radar data which were collected during the 'NEMO 2014' trials in Taranto, Italy, and are shown in Figs. 2 above.

References

[1] *A. Malamou, C. Pandis, P. Frangos, P. Stefaneas, A. Karakasiliotis, D. Kodokostas, "Application of the modified fractal signature method for terrain classification from synthetic aperture radar images", Electronics and Electrical Engineering Journal, Vol. 20, No. 6, pp. 118–121, 2014. [Online]. Available at: http://dx.doi.org/10.5755/j01.eee.20.6.7281.*

[2] *K. J. Falconer, Fractal Geometry: Mathematical Foundations and Applications, J. Wiley and Sons, 1990.*

[3] *Shmuel Peleg, Joseph Naor, Ralph Hartley, and David Avnir, "Multiple Resolution Texture Analysis and Classification", IEEE Transactions on Pattern Analysis and Machine Intelligence, vol. PAMI-6, No. 4, July 1984. https://doi.org/10.1109/TPAMI.1984.4767557*

[4] *Y. Tang, H. Ma, D. Xi, X. Mao, C. Suen, "Modified Fractal Signature (MFS): A New Approach to Document Analysis for Automatic Knowledge Acquisition", IEEE Transactions on Knowledge and Data Engineering, Vol. 9, No. 5, pp. 747-762, Sept. – Oct. 1997.*

[5] *B. Mandelbrot, The Fractal Geometry of Nature, New York: W. H. Freeman and Company, 1977. http://dx.doi.org/10.1119/1.13295 (http://www.aip.org)*

[6] *D. L. Jaggard, A.D. Jaggard, P. Frangos, "Fractal electrodynamics: surfaces and superlattices", in Frontiers in Electromagnetics, Edited by Douglas Werner and Raj Mittra, IEEE Press, 2000, pp. 1-47.*

[7] *P. Beckmann and A. Spizzichino, The scattering of electromagnetic waves from rough surfaces, Norwood, MA: Artech House, 1987.*

[8] *A. Malamou, A. Karakasiliotis, E. Kallitsis, G. Boultadakis, P. Frangos, "Application of a fully automatic autofocusing algorithm for post – processing of synthetic aperture radar images based on image entropy minimization", Electronics and Electrical Engineering Journal, Vol. 19, No. 6, pp. 95 – 98, 2013. [Online]. Available: http://dx.doi.org/10.5755/j01.eee.19.6.4573.*

[9] *G. Pouraimis, A. Kotopoulis, A. Malamou, E. Kallitsis and P. Frangos, "Characterization of Three - Dimensional Rough Fractal Surfaces from Backscattered Radar Data", Elektronika ir Elektrotechnika, ISSN 1392-1215, VOL. 23, No. 4, 2017, Available: http://dx.doi.org/10.5755/j01.eee*

[10] *A. Kotopoulis, A. Malamou, G. Pouraimis, E. Kallitsis and P. Frangos, "Characterization of Rough Fractal Surfaces from Backscattered Radar Data," Elektronika ir Elektrotechnika, accepted for publication in March 2016, http://dx.doi.org/10.5755/j01.eee.*

[11] *N. Ampilova and I. Soloviev, "On digital image segmentation based on fractal and multifractal methods", CEMA'15 Conference Proceedings, pp. 14-17, Sofia, Bulgaria, 2015.*

RADIATION OF VERTICAL DIPOLE ANTENNAS OVER FLAT AND LOSSY TERRAIN: A NOVEL EFFICIENT METHOD FOR THE ACCURATE NUMERICAL CALCULATION OF THE SOMMERFELD INTEGRALS IN THE SPECTRAL DOMAIN

S. Bourgiotis[1], L. Dimopoulos[1], Th. Lymperopoulos[1], A.Chrysostomou[1], S. Sautbekov[2] and P. Frangos[1]

[1]School of Electrical and Computing Engineering, National Technical University of Athens,
9, Iroon Polytechniou Str., 157 73 Zografou, Athens, Greece
Tel. : +30 210 772 3694; FAX : +30 210 772 2281;

e-mail : pfrangos@central.ntua.gr

[2] Al-Farabi Kazakh National University, Department of Physics, Almaty, Kazakshtan

e-mail : sautbek@mail.ru

Abstract

In this paper, the integral expressions of the well-known 'Sommerfeld Radiation Problem', derived by our research group entirely in the spectral domain – as opposed to most classical formulations – are re-evaluated. Numerical integration has revealed various disadvantages regarding the accuracy as well as convergence times of existing formulas. This resulted in their limited practical validity, constrained in the low frequency regime. However, through a proper variable transformation it is possible to convert them into more compact formulas, which overcome the flaws of previous expressions. As a result, convergence times are significantly reduced and, even more important, the new expressions allow for the calculation of the total received EM field of a radiating dipole above flat lossy ground, at almost an arbitrarily chosen level of accuracy. Simulation results, presented herein, indicate the effectiveness and correctness of the proposed method, which can be easily implemented in a general – purpose computer code platform.

1. INTRODUCTION

The 'Sommerfeld radiation problem' is a well-known problem in the area of propagation of electromagnetic (EM) waves above flat and lossy ground [1]. The original Sommerfeld solution to this problem is provided in the physical space by using the 'Hertz potentials' [1]. An equivalent solution to the problem is achieved by working in the spectral domain. In that perspective, in [2] the authors derived simple 1-D integral expressions for the received EM field, which compared to the classical Sommerfeld formulation, do not require taking the potential's derivative, in order to calculate the received field. They also allow the application of asymptotic techniques, like the Stationary Phase Method [3], leading to well-known analytic formulas, applicable in the high frequency regime.

However, accurately evaluating Sommerfeld integrals is not a trivial task. Particularly, it is true that the integral expressions of [2] are generalized integrals, extending from minus infinite to plus infinite and with the integrands presenting singularities, along the integration path. For that reason, the residue theory, along with approximation techniques like the method of Saddle Points, is so widely used by most researchers in the literature in their attempt to evaluate Sommerfeld integrals [4], [5]. However, there is always an accuracy issue that arises when a pole point resides close to the path of integration and even evaluating those integrals purely numerically, required expensive commercial software [5].

In this paper we show that using an appropriate variable transformation it is possible to convert the generalized integrals of [2] into fast converging formulas. Particularly, the integral expression describing the received EM field, is broken down into two parts, one easily computed definite integral and an integral of semi-infinite range. However, the integrand of this second generalized integral, becomes a fast decaying exponential function, resulting in very fast convergence times.

Simulations and comparisons with known literature results [6] are given. Moreover, comparing the new results, with those obtained in [7], which refer to the evaluation of the original integral expressions of [2], without performing the variable transformation, introduced in this paper, indicate the accuracy and the effectiveness of the method.

2. PROBLEM GEOMETRY

The problem geometry is shown in Fig. 1 and described extensively in [1], [2], [4 – 7]. In summary, *p* represents the dipole moment of a radiating vertical Hertzian Dipole at frequency *f*, located at altitude x_0, above infinite, flat and lossy ground, σ being its ground conductivity. Here (ε_1,μ_1), (ε_2,μ_2) represent the constitutive parameters of the air and ground respectively, with ε_0=8,854x10^{-12}F/m being the absolute permittivity in vacuum or air.

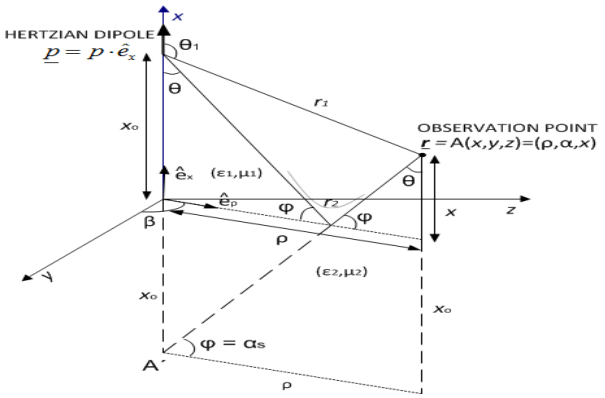

Figure 1. Geometry of the problem

3. DISADVANTAGES CONCERNING THE NUMERICAL INTEGRATION OF THE ORIGINAL SPECTRAL DOMAIN REPRESENTATION FOR THE RECEIVED EM FIELD

In [2], [4] it is shown that the scattered electric field at the receiver's position, above the ground level (x>0) can be expressed by:

$$\underline{E}^R = -\frac{ip}{8\pi\varepsilon_0\varepsilon_1}\int_{-\infty}^{+\infty}\underline{f}(k_\rho)dk_\rho \qquad (1)$$

where:

$$\underline{f}(k_\rho) = \left(\kappa_1\hat{e}_\rho - |k_\rho|\hat{e}_x\right)\, k_\rho |k_\rho| \cdot$$

$$\cdot\frac{\varepsilon_2\kappa_1 - \varepsilon_1\kappa_2}{\kappa_1\left(\varepsilon_2\kappa_1 + \varepsilon_1\kappa_2\right)}\mathrm{H}_0^{(1)}\left(k_\rho\rho\right)e^{i\,\kappa_1(x+x_0)} \qquad (2)$$

and:

$$\kappa_1 = \sqrt{k_{01}^2 - k_\rho^2}\,,\ \kappa_2 = \sqrt{k_{02}^2 - k_\rho^2} \qquad (3)$$

In (2), (3) $H_0^{(1)}$ is the Hankel function of first kind and zero order and k_{01}, k_{02} the wave numbers of propagation in the air and lossy ground respectively.

Expressions (1) – (3) expose the following difficulties when coming to numerically evaluate the respective integral:

- The range of integration extends from $-\infty$ to $+\infty$, resulting in potential errors for large evaluation arguments, despite the fact that the phase factor of (2), i.e. $e^{i\,\kappa_1(x+x_0)}$ gets exponential decaying with respect to k_ρ.
- The Hankel function exhibits a singularity at $k_\rho = 0$ and although it is proved that this singularity does not break the integral's convergence [7], it can affect the accuracy of the numerical integration results, when implemented in the computer.
- As seen from (2), $k_\rho = k_{01}$ is another singularity of the integrand and consequently a sufficient small range around it must be excluded when numerically evaluating (1). As mentioned in [7], doing so may severely affect the accuracy of the results.

4. RE-FORMULATING THE INTEGRAL REPRESENTATION FOR THE EM FIELD

Eq. (1) may be written as:

$$\underline{E}^R = -\frac{ip}{8\pi\varepsilon_0\varepsilon_1}(I_1 + I_2 + I_3) \qquad (4)$$

where,

$$I_1 = \int_{-k_{01}}^{+k_{01}}\underline{f}(k_\rho)dk_\rho \qquad (5a)$$

$$I_2 = \int_{k_{01}}^{+\infty}\underline{f}(k_\rho)dk_\rho \qquad (5b)$$

$$I_3 = \int_{-\infty}^{-k_{01}}\underline{f}(k_\rho)dk_\rho \qquad (5c)$$

For I_1, we perform the following variable transformation: $k_\rho = k_{01}\sin\alpha$, which obviously maps the $[-k_{01},\ +k_{01}]$ range in the k_ρ domain to [-π/2 , π/2] of angle α. With this transform it also holds true:

$$\kappa_1 = k_{01}\cos\alpha,\ \kappa_2 = \sqrt{k_{02}^2 - k_{01}^2\sin^2\alpha} \qquad (6)$$

Applying the above mentioned variable transform to (5a) and with the use of (2),(6), the expression for I_1 becomes:

$$I_1 = k_{01}^3 \int_{-\pi/2}^{+\pi/2} \left(\cos\alpha\,\hat{e}_\rho - |\sin\alpha|\,\hat{e}_x\right)\sin\alpha\,|\sin\alpha| \cdot R_{\parallel}(\alpha)\cdot H_0^{(1)}(\rho\,k_{01}\sin\alpha)\,e^{i\,k_{01}(x+x_0)\cos\alpha}\,d\alpha \quad (7)$$

$$\text{with: } R_{\parallel}(\alpha) = \frac{\varepsilon_2 k_{01}\cos\alpha - \varepsilon_1\sqrt{k_{02}^2 - k_{01}^2\,\sin^2\alpha}}{\varepsilon_2 k_{01}\cos\alpha + \varepsilon_1\sqrt{k_{02}^2 - k_{01}^2\,\sin^2\alpha}} \quad (8)$$

Expression (7) may be further broken down into two integrals:

$$I_1 = k_{01}^3 \left\{ \int_0^{+\pi/2} \left[\left(\cos\alpha\,\hat{e}_\rho - \sin\alpha\,\hat{e}_x\right)\sin^2\alpha\cdot R_{\parallel}(\alpha)\cdot H_0^{(1)}(\rho\,k_{01}\sin\alpha)\,e^{ik_{01}(x+x_0)\cos\alpha}\right]\cdot d\alpha - \int_{-\pi/2}^{0} \left[\left(\cos\alpha\,\hat{e}_\rho + \sin\alpha\,\hat{e}_x\right)\sin^2\alpha\cdot R_{\parallel}(\alpha)\cdot H_0^{(1)}(\rho\,k_{01}\sin\alpha)\,e^{ik_{01}(x+x_0)\cos\alpha}\right]\cdot d\alpha \right\}$$

Finally, observing from (8) that $R_{\parallel}(-\alpha) = R_{\parallel}(\alpha)$ and using the properties of the Hankel function:

$$H_0^{(1)}(z) + H_0^{(2)}(z) = 2\,J_0(z) \quad (9)$$

$$H_0^{(1)}(z\cdot e^{i\pi}) = -H_0^{(2)}(z) \quad (10)$$

it is easy to show that:

$$I_1 = 2\,k_{01}^3 \int_0^{\pi/2} \left[\left(\cos\alpha\,\hat{e}_\rho - \sin\alpha\,\hat{e}_x\right)\cdot \sin^2\alpha\cdot R_{\parallel}(\alpha)\cdot J_0(\rho\,k_{01}\sin\alpha)\cdot e^{i\,k_{01}(x+x_0)\cos\alpha}\right] d\alpha \quad (11)$$

with J_0 being the zero order Bessel function.

For I_2 and I_3, a similar approach is followed. This time the variable transformations, $k_\rho = k_{01}\cosh\alpha$ and $k_\rho = -k_{01}\cosh\alpha$ are used respectively, which both map the original ranges of integration in k_ρ, i.e. $[k_{01},\ +\infty]$ and $[-\infty, -k_{01}]$ to $[0,\ +\infty]$ of variable α. Moreover, in both cases:

$$\kappa_1 = ik_{01}\sinh\alpha,\ \kappa_2 = \sqrt{k_{02}^2 - k_{01}^2\cosh^2\alpha} \quad (12)$$

Consequently, applying a similar reasoning, as with I_1 and also using (9), (10), it is easy to combine the results for I_2 and I_3 as following:

$$I_2 + I_3 = \frac{2k_{01}^3}{i}\int_0^{\infty} \left[\left(i\sinh\alpha\,\hat{e}_\rho - \cosh\alpha\,\hat{e}_x\right)\cdot\cosh^2\alpha\cdot R_{\parallel}'(\alpha)\cdot J_0(\rho\,k_{01}\cosh\alpha)\cdot e^{-k_{01}(x+x_0)\sinh\alpha}\right] d\alpha \quad (13)$$

where:

$$R_{\parallel}'(\alpha) = \frac{i\varepsilon_2 k_{01}\sinh\alpha - \varepsilon_1\sqrt{k_{02}^2 - k_{01}^2\,\cosh^2\alpha}}{i\varepsilon_2 k_{01}\sinh\alpha + \varepsilon_1\sqrt{k_{02}^2 - k_{01}^2\,\cosh^2\alpha}} \quad (14)$$

From (4), (11), (13), the expression for the scattered electric field becomes :

$$\underline{E}^R = -\frac{ipk_{01}^3}{4\pi\varepsilon_0\varepsilon_1}\left\{ \int_0^{\pi/2}\left[\left(\cos\alpha\,\hat{e}_\rho - \sin\alpha\,\hat{e}_x\right)\cdot\sin^2\alpha\cdot R_{\parallel}(\alpha)\cdot J_0(\rho\,k_{01}\sin\alpha)\cdot e^{i\,k_{01}(x+x_0)\cos\alpha}\right] d\alpha - i\int_0^{\infty}\left[\left(i\sinh\alpha\,\hat{e}_\rho - \cosh\alpha\,\hat{e}_x\right)\cdot\cosh^2\alpha\cdot R_{\parallel}'(\alpha)\cdot J_0(\rho\,k_{01}\cosh\alpha)\cdot e^{-k_{01}(x+x_0)\sinh\alpha}\right] d\alpha \right\} \quad (15)$$

5. COMPARISONS – NUMERICAL RESULTS

The new integral form, given by (15), facilitates the numerical evaluation of the EM field, since it overcomes the major drawbacks of expressions (1) – (3), outlined in section 3. Particularly:

- The Hankel function, $H_0^{(1)}$, is substituted by the zero order Bessel function, J_0, which has no singularity, whatsoever.
- The integrand has no singularity at $k_\rho = k_{01}$, hence no need to exclude any range around k_{01} is required.
- The result is expressed as the sum of two integrals, one bound definite integral, ranging from [0, π/2] and an improper integral extending from [0, $+\infty$]. However, due to the presence of $e^{-k_{01}(x+x_0)\sinh\xi}$, the second integrand is a fast decaying function, practically making the integral a bound limits one that is fast converging and easily evaluated in the computer.

The above justifications are validated by simulation results.

The top graph of Fig. 2 depicts the numerical evaluation for the scattered electric field, using (15). It is compared (bottom graph) against the equivalent results of [7], in which the computation was based on the original integral form, given by (1) – (3). In both cases, numerical integration (NI) data are represented by the solid lines of Fig. 2. The parameters for the simulation (i.e. transmitter – receiver heights, ground parameters, operating freq. etc) are given in the bottom plot of Fig. 2.

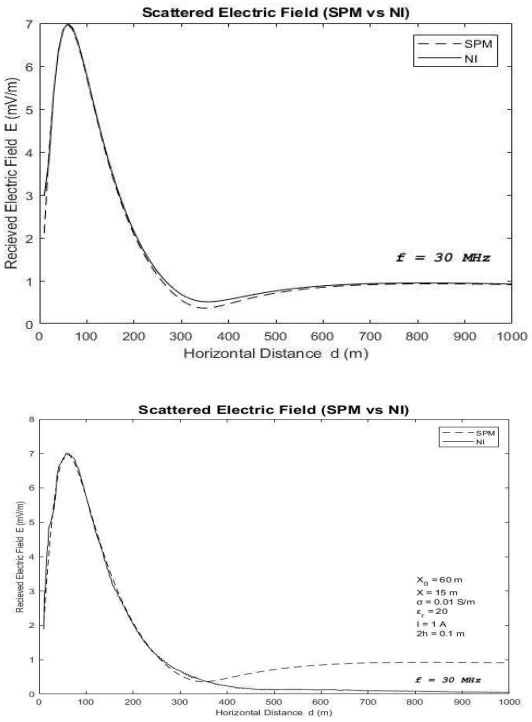

Figure 2. Comparison of Numerical Integration results for the scattered field using : (i) redefined integral expressions (upper figure), (ii) earlier derived spectral integral expressions (lower figure)

Along with the NI results, the high frequency approximation data, obtained after the application of the SPM method to the integral expressions for the Electric field [2], are shown as well (dashed lines). As mentioned in [7], SPM formulas are expected to be accurate in the far field, i.e. at least at distances over 10 – 15 wavelengths, or above 100 – 150m, for the 30MHz case and the problem parameters shown in Fig. 2. Therefore, using the SPM data as the baseline, it is obvious that only the numerical evaluation of (15) achieves the required accuracy. On the contrary, numerical computation of (1) – (3) fails to describe the electric field and this may be attributed to the reasons analyzed in Section 3 above.

In Fig. 3 (top graph), the components of the total received field, for a *Low Frequency (LF) scenario*, are shown. For the direct (LOS) field and the Space Wave, analytic formulas exist, as used in [7]. The scattered field was numerically computed via (15).

Due to the small antenna heights and the long distances involved (~10km), the space wave is expected to diminish [3]. As a result, the link is established primarily by means of the Surface Wave, which is defined as the remaining field, after subtracting the space wave from the total field [5]. This is actually verified in Fig. 3, with the Total Field curve being very close to the Surface Wave results. As a confirmation of the validity of the results, our Surface Wave calculations are compared with the respective Norton formulas [6]. The respective curves are almost identical!

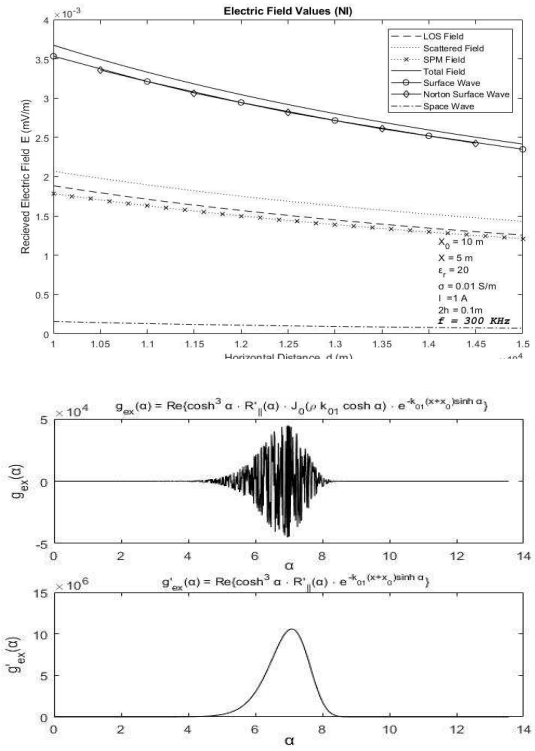

Figure 3. Numerical evaluation of the EM field at the '*low Frequency regime*'

The bottom half of Fig. 3 displays the behavior of the integrand, $g_{ex}(\alpha)$ (actually the real part of the x-directed component), of the second integral expression of (15). It is evident that this integrand is confined in a small window of the integration variable α, outside of which and especially for large values of α, it actually becomes equal to zero. This is attributed to the behavior of the exponential function of the integrand, $e^{-k_{01}(x+x_0)\sinh\alpha}$. Due to the presence of the sinh function in the exponent, it is a vastly decreasing factor, making the whole integrand almost zero for even modest values of α. The bottom line is that the generalized integral of (15) becomes a practically bound limits one, easily and quickly evaluated in the computer.

The oscillations in $g_{ex}(\alpha)$ originate from the behavior of the Bessel function J_0. Its effects on the integrand are visible by comparing the two bottom graphs of Fig. 3. Due to these oscillations, most of the effect of $g_{ex}(\alpha)$ is cancelled, which is why the relative large values of $g_{ex}(\alpha)$ (~10^4) are not reflected in the final field values (~10^{-5})

The simulation of Fig. 3 is now repeated at Fig. 4 for a *high frequency scenario* in the VHF/UHF band. Again, the source and observation points are located close to the ground level and the electric field values at various distant observation points are calculated.

As shown in Fig. 4, in this case the observed Surface Wave is negligible, a result also predicted by Norton [6]. Consequently, the Space Wave almost completely describes the total received field and hence the SPM method, an asymptotic method that converges to the space wave formulas [2], [7], is validated in this high frequency case, despite the small grazing angle (angle φ of Fig. 1) of the scenario [7]. Finally, notice in the bottom graph of Fig. 4 how quickly, $g_{ex}(\alpha)$ vanishes, making thus the convergence of (15) very fast.

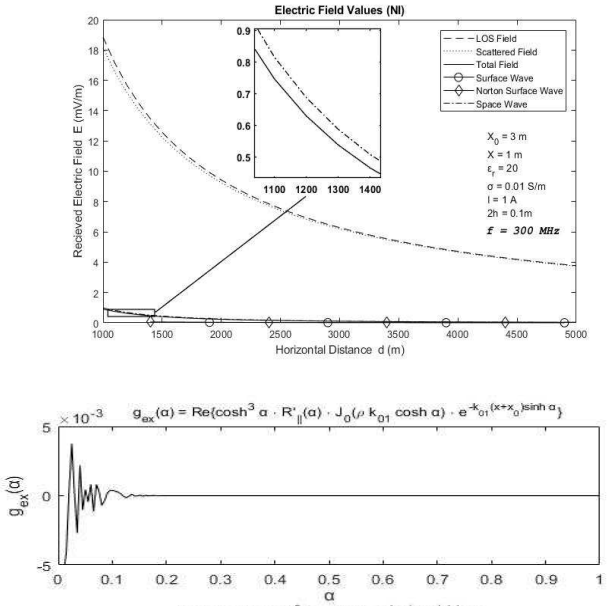

Figure 4. Numerical evaluation of the EM field at the VHF/UHF band ('high frequency regime')

As a final validation, the field values (*this time for the magnetic field*) for the scenario of Fig. 2 (i.e. frequency f=30 MHz) are shown in Fig. 5. Again, it seems there is a very good match between our calculations with the respective Norton's results [6].

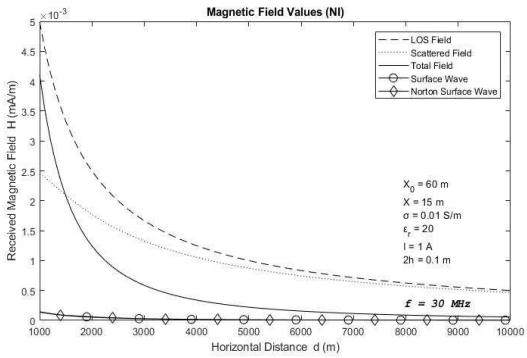

Figure 5. Magnetic field components at the frequency of 30MHz

6. CONCLUSION

In this paper we continue our previous research work on the solution of the 'Sommerfeld radiation problem' in the spectral domain. Using an appropriate variable transformation, it is shown that the disadvantages of the previous integral expressions for the EM field are effectively addressed. The EM field is now expressed as an integral formula, which is easy and fast to evaluate in the computer, using a general purpose computer code suite, as opposed to commercially specialized software, used in the literature [5].

Details about the algorithm, used and the specifics of the implementation code will be given in the accompanying Journal paper, currently prepared by our research team. For the time it is enough to say that the results, presented herein, were obtained with a required relative accuracy level of 10^{-3}, although in most of the cases the achieved, estimated accuracy was less than 10^{-5} (meaning that the algorithm might accept further improvements for even faster computation times). With this setting, only a few seconds or even parts of a second (depending on the case) were just enough to estimate the EM field, at each reception point (horizontal distance from the source). Higher accuracy levels are addressable by the algorithm (e.g. the algorithm was run with a 10^{-10} setting) requiring, however, larger convergence times. Nevertheless, from a visualization perspective, the captured graphs differed imperceptibly from the ones shown here.

References

[1] *A. N. Sommerfeld, "Propagation of Waves in Wireless Telegraphy", Ann. Phys., 28, pp. 665–736, March 1909; and 81, pp. 1135–1153, December 1926.*

[2] *K. Ioannidi, Ch. Christakis, S. Sautbekov, P. Frangos and S.K. Atanov, "The radiation problem from a vertical Hertzian dipole antenna above flat and lossy ground: novel formulation in the spectral domain with closed-form analytical solution in the high frequency regime", International Journal Antennas and Propagation, Hindawi Ed. Co., Special Issue 'Propagation of electromagnetic (EM) waves over terrain' (PEWT), vol. 2014.*

[3] *C. A. Balanis, Antenna Theory: Analysis and Design, New York: J. Wiley and Sons Inc., 1997, Appendix VIII: Method of Stationary Phase, pp. 922–927.*

[4] *Seil Sautbekov, Sotiris Bourgiotis, Ariadni Chrysostomou and Panayiotis Frangos, 'A Novel Asymptotic Solution to the Sommerfeld Radiation Problem: Analytic field expressions and the emergence of the Surface Waves', 'Progress in Electromagnetics Research M' Journal ('PIER M'), Vol. 64, pp. 9-22, 2018.*

[5] *T. K. Sarkar et. al., "Electromagnetic Macro Modelling of Propagation in Mobile Wireless Communication: Theory and Experiment", IEEE Antennas and Propagation Magazine, Vol. 54, No. 6, pp. 17–43, Dec. 2012.*

[6] *K. A. Norton, "The Propagation of Radio Waves Over the Surface of the Earth", Proceedings of the IRE, 24, pp. 1367–1387, 1936; and 25, pp. 1203–1236, 1937.*

[7] *A. Chrysostomou et. al., "Radiation of a Vertical Dipole Antenna over Flat and Lossy Ground: Accurate Electromagnetic Field Calculation using the Spectral Domain Approach along with Redefined Integral Representations and corresponding Novel Analytical Solution", Electronics and Electrical Engineering Journal, Vol. 22, No. 2, 2016.*

APPLICATION OF THE METHOD OF AUXILIARY SOURCES (MAS) TO THE ANALYSIS OF ELECTROMAGNETIC SCATTERING FROM DIELECTRIC SURFACES WITH CURVED WEDGES

Vissarion G. Iatropoulos, Minodora-Tatiani Anastasiadou, Hristos T. Anastassiu

Department of Informatics Engineering
Technological Educational Institute (TEI) of Central Macedonia,
End of Magnisias Str., GR-62124 Serres,
GREECE
hristosa@teiser.gr

Tel.: +30 23210 49376
Fax: +30 23210 49128

Abstract

The Method of Auxiliary Sources (MAS) is applied to Transverse Magnetic (TM) plane wave scattering from infinite, dielectric, non-smooth cylinders. The geometry of the scatterer is assumed to include curved wedges, defined as intersections of circular arcs, for the first time in literature. The auxiliary surface is shaped in various patterns, to study the effect of its form on the MAS accuracy. In addition to the standard, conformal shape, several deformations are tested, where the auxiliary sources are allowed to approach the tip of the wedge. It is demonstrated that such a procedure leads to significant improvement of the numerical results accuracy. Comparisons of schemes are presented, and the optimal auxiliary source location is proposed.

1. INTRODUCTION

The Method of Auxiliary Sources (MAS) [1] is a numerical technique that has successfully been invoked in computational electromagnetics, in a wide range of radiation and scattering phenomena [2]. MAS is somewhat similar to the Point Matching version of the Method of Moments (MoM), however the auxiliary current sources are not located on the surface boundaries, but inside the radiator/scatterer. The method has been shown to be mathematically rigorous, since the basis functions set used in the field expansions has been proven to be complete [3], which is not always easy to prove in MoM. Moreover, unlike MoM, MAS does not face singularity problems, it avoids time-consuming numerical integration at every stage of the solution, and its algorithmic implementation is much more straightforward.

Although MAS has been utilized in several problems with various geometries and materials, further research is necessary to determine the optimal source location for arbitrary configurations. Particular complications arise when the outer boundary of the scatterer contains wedges, i.e. when the analytical expression of the boundary is not differentiable. In that case, it has been observed that the solution accuracy is depleted, because the boundary condition close to the wedge tip is hard to satisfy adequately. To apply MAS to such configurations, a set of auxiliary sources (AS's) is situated on a fictitious surface, which is generally conformal to the actual boundary, except in the neighborhood of the tips. In the areas surrounding the wedges, the AS's are densely packed and located very close to the tips, to account for the edge effects, as suggested in [4]. Similar strategies were employed in the case of a scattering problem associated with coated Perfectly Electric Conducting (PEC) surfaces including wedges [5], where the surface was modeled via the Standard Impedance Boundary Condition (SIBC) [6].

Although this deformation of the auxiliary surface has proven efficient for straight wedges, in particular forming right angles, no evidence is known from the literature about its applicability to arbitrarily shaped wedges. The aim of this paper is to investigate whether MAS accuracy is enhanced through this deformation, when the wedge is shaped as an intersection of circular arcs with non-coincident centers. The scatterer is thus defined as a dielectric, infinite cylinder, with eye-shaped cross-section. The auxiliary surface is generally maintained as conformal to the scattered boundary, except in the neighborhood of the wedge tips, where various deformation schemes are employed, and accuracy comparisons are drawn.

The format of the paper is as follows: Section 2 quickly recapitulates the mathematical formulation of MAS for dielectric scatterers, illuminated by a transverse magnetic (TM) polarized plane wave. Section 3 proposes several algorithms for the deformation of the auxiliary surfaces close to the wedge tips. Section 4 includes several numerical results for the eye-shaped scatterer and checks the satisfaction of the boundary condition. Finally, section 5 summarizes the method and draws useful conclusions.

A $+j\omega t$ behavior is assumed and suppressed throughout the paper.

2. MAS FOR EYE-SHAPED DIELECTRIC SCATTERERS

We assume a dielectric, infinitely long cylinder with cross section that resembles an eye (Fig. 1a). The dielectric is assumed to be linear, homogeneous and isotropic. The geometry of the scatterer, depicted in blue, comprises two circular arcs with identical radii equal to ρ, but with different centers. In particular, the Cartesian coordinates of the upper arc are given by

$$x_u = \rho cos\varphi,\ y_u = \rho sin\varphi - d \qquad (1)$$

whereas those of the lower arc are given by

$$x_l = \rho cos\varphi,\ y_l = \rho sin\varphi + d \qquad (2)$$

where φ is the azimuth angle and $\pm d$ is the vertical displacement of each arc center, taken equal to the arc apothem (see Fig. 1b). Obviously, φ does not range in the entire $[0,2\pi)$ interval, but is limited by the arc width itself, given by $\varphi_{arc} = 2\arccos\frac{d}{\rho}$. The scatterer is illuminated by a TM plane wave impinging from azimuth angle equal to φ_{inc}. Therefore the incident electric field $\boldsymbol{E}_{inc}$ is given by

$$\boldsymbol{E}_{inc}(x,y) = E_0 \exp\{jk_0(xcos\varphi_{inc} + ysin\varphi inc\boldsymbol{z} \qquad (3)$$

where E_0 is the amplitude of the incident electric field and k_0 is the free space wavenumber. The incident magnetic field $\boldsymbol{H}_{inc}$ is given by

$$\boldsymbol{H}_{inc}(x,y) = -\frac{E_0}{\zeta_0}(\sin\varphi_{inc}\hat{\boldsymbol{x}} - \cos\varphi_{inc}\hat{\boldsymbol{y}}) \exp\{jk_0(xcos\varphi_{inc} + ysin\varphi_{inc})\} \qquad (4)$$

where ζ_0 is the free space intrinsic impedance. To solve the scattering problem via MAS, two sets of AS's are defined, each one of multitude N, as shown in Fig. 1a. In standard MAS formulation both inner and outer auxiliary surfaces are conformal to the scatterer boundary. The electric field due to the n^{th} inner AS, located at point $\boldsymbol{r}_n$ and radiating in the outer space is

$$E_{sn}(\boldsymbol{r}) = \hat{\boldsymbol{z}}E_n H_0^{(2)}(k_0|\boldsymbol{r} - \boldsymbol{r}_n|) \qquad (5)$$

where E_n is the corresponding unknown weight, $(n = 1,2,\dots,N)$, and $H_0^{(2)}$ is the Hankel function of zero order and second kind. The corresponding magnetic field of the n^{th} auxiliary source is obviously proportional to the curl of (5), given explicitly in [5]. Similar expressions hold for the outer AS's, radiating in the inner space of the scatterer, except for k_0 and ζ_0, which have to be replaced by k and ζ respectively, corresponding to the scatterer's dielectric properties. The total scattered E field is expressed as superposition of the fields in (5) and the H field accordingly. By applying the boundary conditions for both fields at N collocation points (CP's) (x_m, y_m) $(m = 1,2,\dots,N)$ of the scattering boundary (blue dots in Fig. 1a), we cast a linear system of equations

$$[\boldsymbol{Z}]\{\boldsymbol{I}\} = \{\boldsymbol{V}\} \qquad (6)$$

where $\{\boldsymbol{I}\}$ is the column vector of the unknown weights E_n, $[\boldsymbol{Z}]$ is a square matrix of size $2N \times 2N$ with elements determined by the interaction between AS's and CP's and $\{\boldsymbol{V}\}$ is the column vector of the incident E and H fields calculated at the CP's.

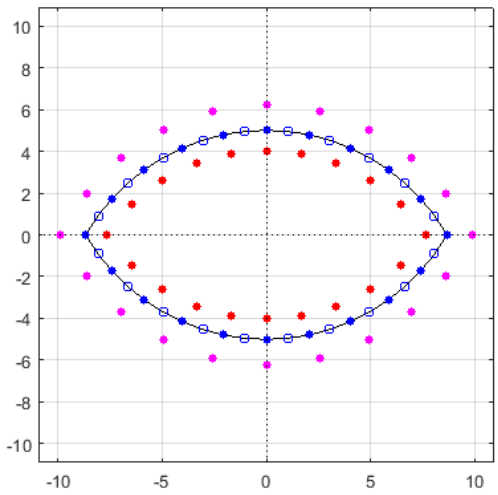

Fig. 1. a) Geometry of the scatterer (in blue) including inner auxiliary sources (AS's) (red) and outer auxiliary sources (AS's) (magenta). Blue dots stand for collocation points (CP's) and blue circles for midpoints (MP's).

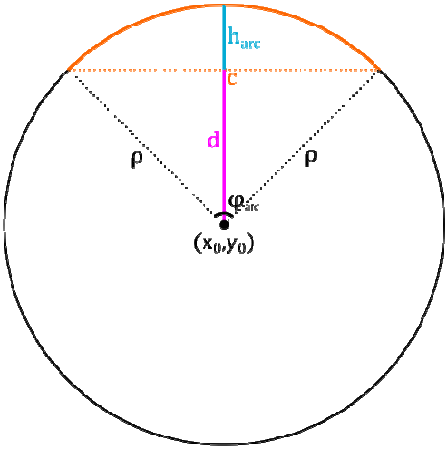

Fig. 1. b) Construction of the geometry.

3. IMPROVEMENT OF THE AUXILIARY SURFACE LAYOUT

As mentioned in [4],[5], MAS becomes less accurate when the auxiliary surfaces are conformal to boundaries including wedges. Specifically, satisfaction of the boundary condition at midpoints (MP's) (see Fig. 1a) close to the tips is no longer adequate. To overcome this complication, the auxiliary surface may be deformed so that AS's not only approach the tips closely, but become denser in the tip neighborhood as well. AS's may approach CP's following several patterns. In this work, two basic patterns were tested. Let M be the number of AS's to be moved. Let ρ_m be the polar radius of the m^{th} AS $(m = 1,2,\dots,M)$, let g be the maximum polar radius distance between the m^{th} AS and the m^{th} CP. Finally, let s be the proximity factor, defined in $[0,1]$, so that 0 corresponds to no approach and 1 corresponds to maximum approach (resulting in coincident AS's and CP's). Then, the schemes proposed for the auxiliary surface deformation are defined as follows:

$$\rho'_m = \rho_m + gs\left(\frac{m}{M}\right)^{\nu} \qquad (7)$$

where $\nu = 1$ for simple and $\nu = 2$ for progressive reach. The deformation effect is graphically described in Figs. 2,3.

Furthermore, as proposed in [5], AS's, and CP's accordingly, should become denser close to the wedge tip. Again, there is no unique way to accomplish this. In this work, the scheme implemented multiplies the polar angle φ_m of the m^{th} AS location by a factor D_m, $0 < D_{start} \le D_m \le 1$, where D_{start} is user-defined. For example, in the first quadrant of the 'eye', D_m is defined to be close to 0 for AS's near the wedge tip, and close to 1 for AS's close to the vertical axis. For progressive densification, the scheme proposed is: $\varphi'_m = \varphi_m D_m^2$. Moreover, additional AS's may be superimposed to the already existing ones close to the tips, if necessary (see Fig. 4)

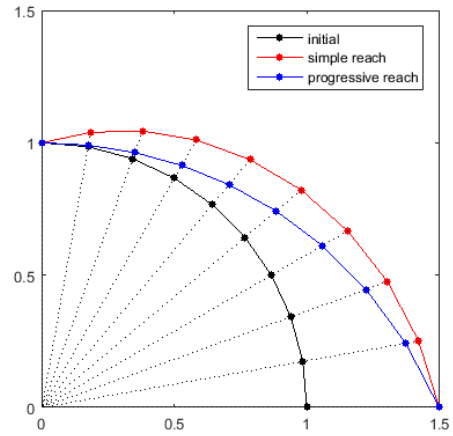

Fig. 2. Polar radius increase from 1 to 1.5 according to the proposed schemes

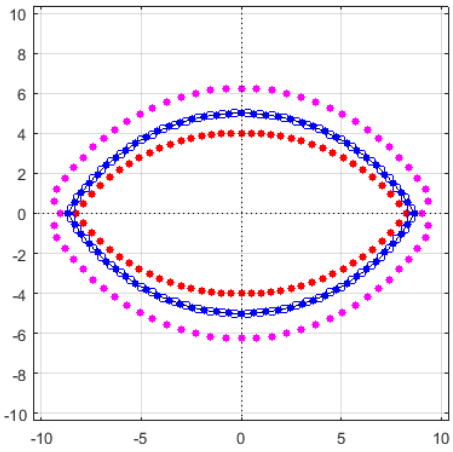

Fig. 3. Deformation of the auxiliary surface: all inner AS's are allowed to approach the CP's, whereas only 1/8 of the outer AS's are allowed to do so

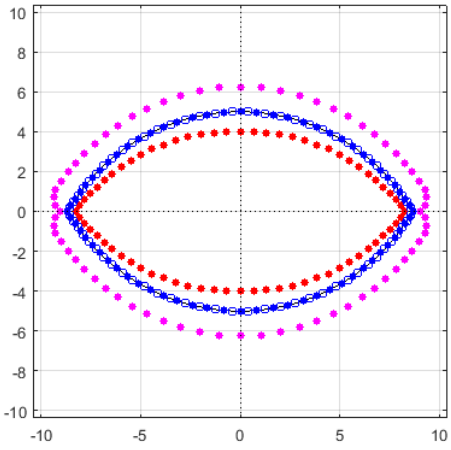

Fig. 4. Combination of tip approach and densification of the AS's

4. NUMERICAL RESULTS

To test the efficiency of the method, a scatterer is defined by radius $\rho = 3\lambda$, arc displacement $d = 1.5\lambda$, dielectric relative permittivity $\varepsilon_r = 2.56$, incidence angle $\varphi_{inc} = 0$, and originally $N = 160$ CP's, hence 160 inner and 160 outer AS's. Solution of the problem without any deformation yields the results of Fig. 5. The upper left subplot depicts the quantified error in the boundary condition (BC) of the E field along the boundary stretch, i.e.

$$\Delta E_{bc} = \frac{|\hat{\boldsymbol{n}} \times (\boldsymbol{E}_{in} - \boldsymbol{E}_{out})|}{E_0} \qquad (8)$$

where $\hat{\boldsymbol{n}}$ is the normal unit vector on the boundary, pointing outwards, and $\boldsymbol{E}_{in}, \boldsymbol{E}_{out}$ are the electric fields just inside and just outside the scatterer respectively. Similarly, the upper right subplot depicts the quantified error for the H field, and the lower plot illustrates the bistatic Radar Cross Section (RCS) in terms of the polar angle. It is obvious that the BC error is relatively significant in the immediate vicinity of the wedge tips.

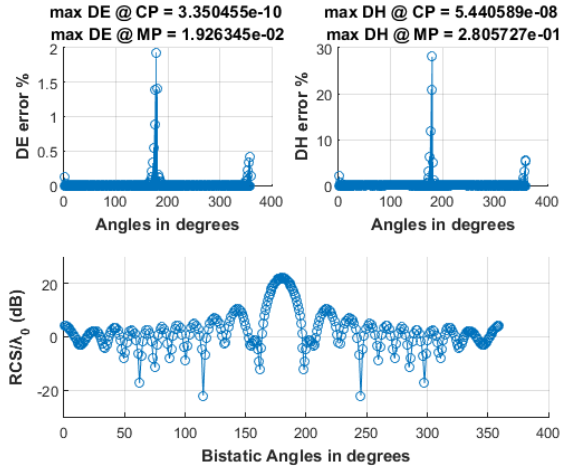

Fig. 5. Results for standard, conformal auxiliary surfaces

To improve satisfaction of the BC, the deformation scheme proposed above was implemented. After several trials, the following parameters were finally invoked: The portion of AS's to be displaced was $1/5$ for the inner and $1/8$ for the outer ones. The proximity factor was set equal to $s = 0.75$ for the inner and $s = 0.65$ for the outer AS's, while $D_{start} = 0.80$. No extra AS's were added, since their presence proved to be unimportant.

The results are shown in Fig. 6. The maximum E field error at MP's was reduced from $1.92 * 10^{-2}$ to $3.71 * 10^{-3}$ and the maximum H field error from $2.8 * 10^{-1}$ to $1.95 * 10^{-2}$. Although the RCS pattern is only slightly affected, more pronounced improvement is expected for larger scatterers.

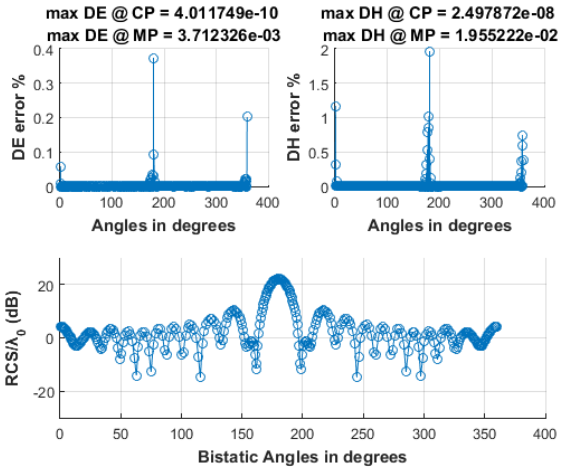

Fig. 6. Results for improved, non-conformal auxiliary surfaces

5. CONCLUSION

The Method of Auxiliary Sources (MAS) was applied to scattering from a dielectric cylinder with curved wedges. Since the BC error close to the wedge tips is significant for standard, conformal auxiliary surfaces, deformation of the latter was proposed. In the vicinity of the tips, both inner and outer AS's approached the CP's, and their distribution was also allowed to become denser. The BC error was proven to decrease significantly for both the E and the H field, yielding more accurate RCS results.

The authors wish to acknowledge financial support by the Special Account for Research Funds of the Technological Educational Institute of Central Macedonia, Greece, under grant SAT/IE /141/11/18-6-2014/80093.

References

[1] *R. S. Popovidi-Zaridze and Z. S. Tsverikmazashvili, "Numerical study of a diffraction problem by a modified method of non-orthogonal series", Zh vychisl. Mat. mat. Fiz., 17, 2, 1977, pp. 384-393.*

[2] *D. I. Kaklamani and H. T. Anastassiu, "Aspects of the Method of Auxiliary Sources (MAS) in Computational Electromagnetics", IEEE Antennas and Propagation Magazine, vol. 44, no. 3, June 2002, pp. 48-64.*

[3] *V. D. Kupradze, "On the approximate solution of problems of mathematical physics", Usp. mat. nauk, 22, no 2 (134), 1967, pp. 59-107.*

[4] *S. Eisler and Y. Leviatan, "Analysis of Electromagnetic Scattering from metallic and penetrable cylinders with edges using a Multifilament Current Model", IEE Proceedings, vol. 136, Pt. H, No. 6, Dec. 1989, pp. 431-438.*

[5] *H. T. Anastassiu, D. I. Kaklamani, D. P. Economou and O. Breinbjerg, "Electromagnetic Scattering Analysis of Coated Conductors with Edges Using the Method of Auxiliary Sources (MAS) in Conjunction with the Standard Impedance Boundary Condition (SIBC)", IEEE Trans. on Antennas and Propagation, vol. 50, no. 1, Jan. 2002, pp. 59-66.*

[6] *T. B. A. Senior and J. L. Volakis, Approximate Boundary Conditions in Electromagnetics, IEE Press, 1994.*

LOCALIZATION OF A SINGLE SOUND SOURCE FROM BINAURAL RECORDINGS

Gergana Vasileva, Ivo R. Draganov

Radiocommunications and Videotechnologies Dept.
Faculty of Telecommunications, Technical University of Sofia
8 Kliment Ohridski Blvd., 1756 Sofia, Bulgaria

e-mail: gergana_v95@abv.bg, idraganov@tu-sofia.bg

Abstract

In this paper is investigated the possibility of localizing a single sound source from binaural recordings using only low cost components and computationally light weighted applications. Interaural time difference and interaural intensity difference are in the basis of estimating the azimuth angle of the source equally distanced from the listener during testing. Low, mid and high frequencies are being generated by precise generator to analyze the accuracy of localization by the arranged environment. Positive results are being observed in comparison to more sophisticated methods demanding more resources.

1. INTRODUCTION

Binaural recordings have been used for a long time as a mean for producing more realistic experience in listeners close to the real environment where the sounds were recorded. Some recent studies suggest that they are also applicable for accurate sound source localization.

Minnaar et al. [1] discovered that here is a significant difference in audio recordings of this type when made from real human heads and artificial ones. Head-related transfer function in each case seems to be different. Considering both the interaural time differences and the interaural level differences Raspaud et al. [2] achieve better accuracy of the source localization. Further they propose an average parametric model based on personal estimates of these parameters. The model proved useful up to 6 kHz and its accuracy significantly decreases for azimuth angles approaching -90º and +90º respectively. Joint error averages vary between 3.35 and 11.34 by the type of sound.

More complex sound scenes, consisting of numerous sparse-spectrum sources, have been decomposed by Deleforge et al. [3] following by their localization with the use of acoustic space learning. Robot heads were used for the recordings and then dimensionality reduction via non-linear processing was applied. The mean angular error is changing between 3º and 12º. Deleforge and Horaud [4] also proposed simpler approach to the 2D localization problem by establishing a connection between sources' positions and interaural information registered in space with larger number of dimensions. Deviation of the angular error here rises up to 14º as or the azimuth detection with the increase of the training set density.

Hammershøi et al. [5] posed attention not only to the medium of sound propagation and elements for recording in relation to the personal hearing properties but also to the chain for playback. Inter-individual parameters were considered while making a correction prior to headphone reproduction. Deviation in the median-plane localization varied between 25% and 47% depending on the type of the head while recording.

Mandel et al. [6] use expectation-maximization on a model for present sources separation from the scene in order to localize them. Selective points from the spectrogram of the recorded signals after clustering indicate their presence. Separated signals have SNR 1.6 dB and and PESQ 0.27 greater than other proven techniques.

Coherence within binaural recordings and the sensitivity of human hearing with regard to the interaural time difference, especially at the presence of noise, seemed to play a role in the localization of sound sources as Rakerd and Hartmann [7] show. Their study suggests that correction should be made to the stored signals modeling the whole chain of elements leading to reproducing.

Joris and Yin [8] found that internal delays occurring due to the change in waveform of the sound from one and the same sources reaching both ears plays also a role in the localizing process. So interaural

correlation should also be employed in the model used for binaural recording.

In addition to all the above mentioned effects which need to be considered in the channel modelling of binaural recordings, Baumgartner et al. [9] pay attention to the localization of sources in sagittal-plane. Thus, it becomes possible to discriminate their position within front and back subspace. It is considered that similar approaches may have role in some medical applications [12].

In this paper, a simplified experimental setup is proposed for binaural recording followed by single source localization, cheap enough to be implemented on a wider scale for mass-user applications. In Section 2 description of the proposed methodology is given followed by experimental results in Section 3 with comparison to other implementation used in practice and related discussion. Then, a conclusion is made in Section 4.

2. METHODOLOGY DESCRIPTION

Influence over the process of a sound source localization (Fig. 1) have both the interaural time difference (ITD) and the interaural intensity difference – IID). The first factor is a sequence of the different length of the paths the sound wave is travelling to both ears. The second difference follows from the shadowing effect of the listener's head over one of the ears along the sound propagation direction.

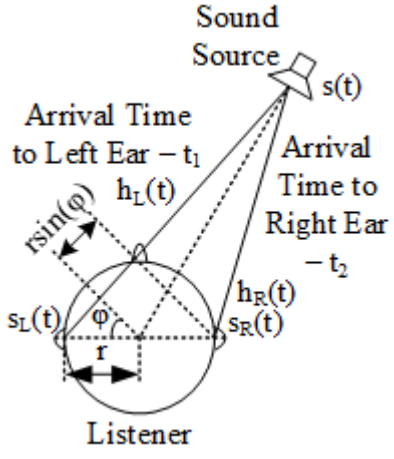

Fig. 1. Geometric model of the sound scene

On that basis, the interaural phase delay – IPD could be defined:

$$\Delta t = \left(\frac{r}{v}\right) 2\sin(\varphi), \qquad (1)$$

where v is the peed of the sound in the surrounding medium. It is obvious that $\Delta t = t_1 - t_2$. Decreasing of the frequency of the emitted signal leads to comparability between the wavelength and the distance from the source to the listener and from a given pint it could be considered that:

$$2\sin(\varphi) \approx \varphi + \sin(\varphi). \qquad (2)$$

The average diameter of the head $2r$ relates to the frequency below which the information for the spatial configuration interpreted by the user about the source is obtained mainly due to the ITD:

$$f_s = \frac{v}{2r} = \frac{340}{0.25} \approx 1.5\ kHz. \qquad (3)$$

Only the azimuth angle could be estimated taking into account (1)-(3) of the source in relation to the head – a result from the presence of ITD and IID.

In order to model the propagation channel and the transform by the hearing apparatus it is needed to introduce the Head-Related Impulse Response – HRIR. It is different for each ear. If for the left and right ear of a particular listener $h_L(t)$ and $h_R(t)$ denote the respective responses then $H_L(f)$ and $H_R(f)$ will be their representation in frequency domain. Sound wave pressure for the left and right ear in time domain could be represented by $s_L(t)$ and $s_R(t)$ at a source emission $s(t)$. Then:

$$s_{L,R} = h_{L,R}(t) * s(t) = \\ = \sum h_{L,R}(t - \Delta t)s(t)\Delta t \qquad (4)$$

Which in frequency domain is transformed to:

$$S_{L,R}(f) = \mathcal{F}\{h_{L,R}(t) * s(t)\} = \\ = H_{L,R}(f)S(f). \qquad (5)$$

HRTF can be found experimentally by changing the azimuth angle of the source with regard to the position of each ear using the following expression:

$$H_{L,R}(f,\varphi) = S_{L,R}(f,\varphi)/S(f,\varphi), \qquad (6)$$

where $S_{L,R}(f,\varphi)$ is calculated from the Fourier transform of the registered by microphone signal $s_{L,R}(t)$ in the position corresponding to the left and right ear separately. These microphones are located within the pinna of a dummy head which is a part of the experimental testing described in the next section. Calibrated generator connected with a loud-

speaker acts as a signal source with the option of changing the generated frequency *f* and level *s(f)*. The typical setup includes testing inside the far field (> 1m) of the source in which case *s(f)* decreases inversely with the distance to the microphone. The levels inside both ears then are expected to be closer. At distances less than a meter this difference considerably increases for the whole sound range.

Given a binaural recording, it becomes possible for a human to localize a sound source from a virtual sound space. The recording of the one channel $s_{L1}(t)$ is played through a headphone placed in the left year and the other – $s_{R1}(t)$ – by a headphone in the right year. The generated sound signals which affect the ear drums of both ears are $s_{l2}(t)$ and $s_{r2}(t)$ respectively. It is required that $s_{L2}(t) = s_{L1}(t)$ if HRTF has been properly estimated. In frequency domain the following expression holds:

$$\boldsymbol{S_{L1}(f) = S(f).H_M}(\mathrm{F})\,.\boldsymbol{H_L}(\mathrm{F})\,.\boldsymbol{H_S}(\mathrm{F}), \quad (7)$$

where $S_{L1}(f)$ is the spectrum of $s_{L1}(t)$, $H_M(f)$ – is the transfer function of the microphone from the left ear during recording, $H_S(f)$ – the transfer function of the loudspeaker playing the role of a sound source during the experimental testing.
ANALOGOUS TO THAT:

$$\boldsymbol{S_{L2}(f) = S_{L1}(f).H_{HPHL}(f).H_{CL}(f)}, \quad (8)$$

where $H_{HPHL}(f)$ is the transfer function of the headphone from the left ear and $H_{CL}(f)$ – that of a correcting filter applied during playback. Letting $s_{L1}(f) = s_{L2}(f)$ leads to:

$$\boldsymbol{H_{CL}(f) = 1/H_{HPHL}(f)}. \quad (9)$$

The transfer function of the correcting filter for the right ear $H_{CR}(f)$ could be found in the same way in order to apply the correction prior to the emission. In our study we employ the techniques described in [5] for finding all the transfer functions described above. Then, localizing the source from the recordings is done by using the relations presented in [10]. The general flowchart of all processing steps is given in Fig. 2.

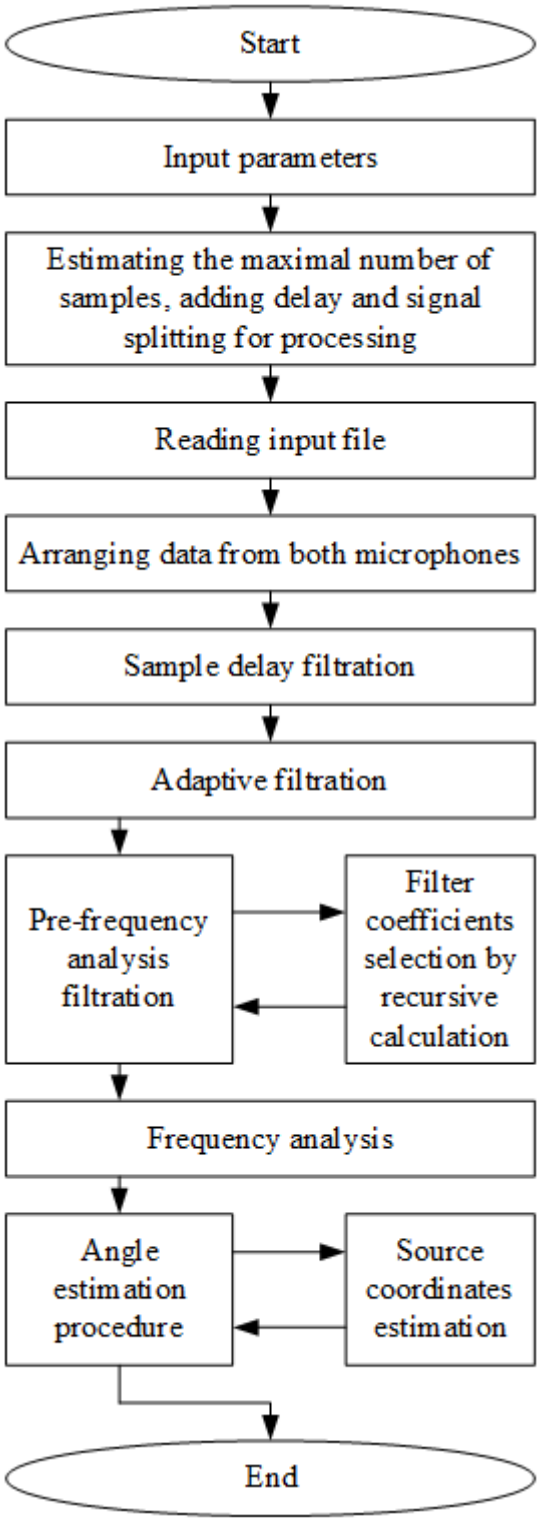

Fig. 2. Sound source localization algorithm

3. EXPERIMENTAL RESULTS

In order to accomplish the assigned task the model shown in Fig. 3 is used.

Instead of a human head, a mannequin head of approximately the same size is selected. The ear canal of the manikin is punctured and the two microphones are placed there. In Fig. 4, the head is

located at a distance of 50 cm from the speaker and rotated at an angle of 0 degrees to it.

Fig. 3. Head of a dummy imitating human head

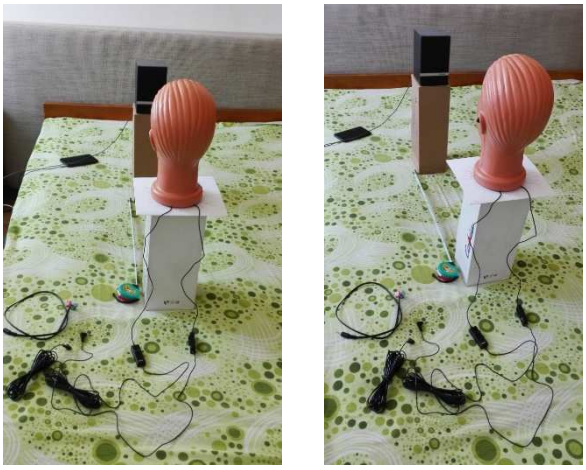

Fig. 4. Placement of the model

In order to obtain two channels (left and right) for the stereo signal, the microphones are connected by a circuit using three-way cable (Fig. 5).

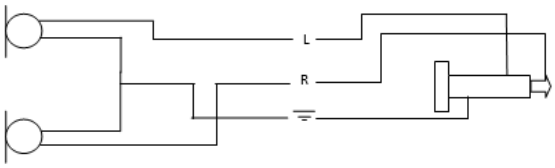

Fig. 5. Electrical circuit of a three-way cable

The three-way cable (Fig. 6) is connected to a computer for recording by the GoldWave program [11].

Recordings are made for signals with frequencies (400 Hz, 500 Hz, 700 Hz, 1 kHz, 2 kHz), and the head is located at (0, 5, 10, 15, 20, 25, 30) degrees to the speaker (the source of the sound signal). The speaker distance is 50 cm and 100 cm.

The sensitivity of the microphones is +/- 3 db (-65 db) with operational range from 50 Hz to 16 kHz and impedance of 900 Ω.

Fig. 6. Three-way cable

In the first experiment, when the sound source is located at 0.5 m from the dummy head the absolute estimation error of the azimuth angle changes for virtually all tested frequencies (Fig. 7). Most notably, the change occurs for 400 Hz with 18.48º on average. For higher frequencies the variation within testing range is smaller and closer one to the other – 8.87º.

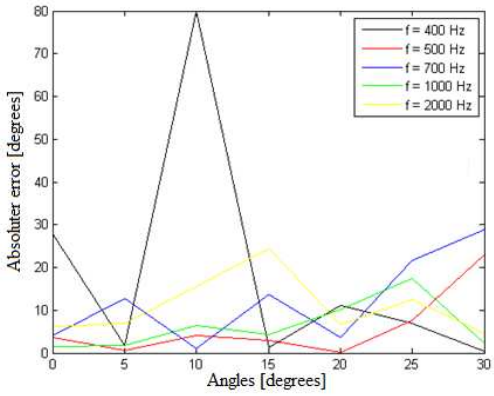

Fig. 7. Absolute estimation error of the orientation angle at 50 cm distance

The relative error for all the cases at 0.5 m is given in Fig. 8. The mid frequency of 1 kHz produces smallest error, equal to 6.32º.

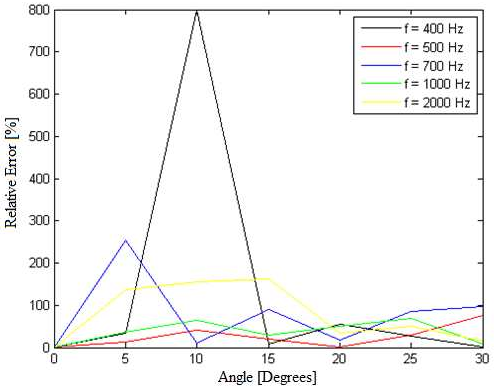

Fig. 8. Relative estimation error of the orientation angle at 50 cm distance

Testing at 1 m distance from the sound source gives smaller accuracy of localizing it (Fig. 9).

The relative estimation error in the latter case is presented in Fig. 10.

With the exception of the mid frequency of 1 kHz and the lower one of 400 Hz, all the others tend to increase the error – with 11.39º. The mean absolute error of the first two frequencies is 6.86º.

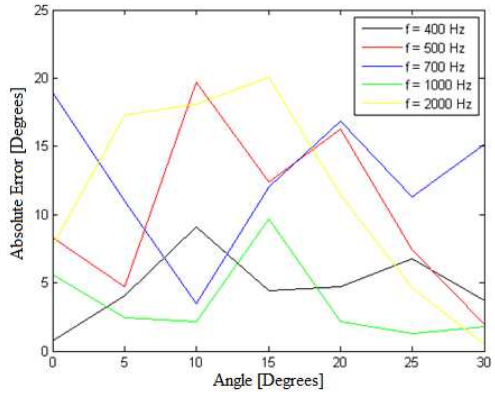

Fig. 9. Absolute estimation error of the orientation angle at 100 cm distance

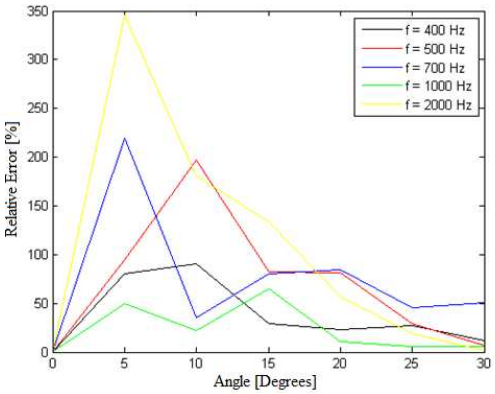

Fig. 10. Relative estimation error of the orientation angle at 100 cm distance

The probabilistic approach for localizing sound sources in [2] gives for mid frequencies error in azimuth angle from 3º to 4º when rotating the sound detector system from 0º to 30º. Given the more sophisticated approach suggested in that study and hardware used the average difference of 2º obtained within our approach seems negligible.

4. CONCLUSION

Binaural sound brings considerably more information than ordinary stereo recording. This gives a more realistic sense of the real environment in which the recording is made. The recordings made are also sufficient to locate a sound source after program processing, but with some frequency and directional limitations. For more accurate localization, it would take longer recording time for more precise analysis. The deviations in the results are due to the lateral noises, the presence of standing waves, and the relatively short length of the analyzing windows.

References

[1] *MINNAAR, Pauli, et al. Localization with binaural recordings from artificial and human heads. Journal of the Audio Engineering Society, 2001, 49.5: 323-336.*

[2] *RASPAUD, Martin; VISTE, Harald; EVANGELISTA, Gianpaolo. Binaural source localization by joint estimation of ILD and ITD. IEEE Transactions on Audio, Speech, and Language Processing, 2010, 18.1: 68-77.*

[3] *DELEFORGE, Antoine; FORBES, Florence; HORAUD, Radu. Acoustic space learning for sound-source separation and localization on binaural manifolds. International journal of neural systems, 2015, 25.01: 1440003.*

[4] *DELEFORGE, Antoine; HORAUD, Radu. 2D sound-source localization on the binaural manifold. In: Machine Learning for Signal Processing (MLSP), 2012 IEEE International Workshop on. IEEE, 2012. p. 1-6.*

[5] *HAMMERSHØI, Dorte; MØLLER, Henrik. Binaural technique—Basic methods for recording, synthesis, and reproduction. In: Communication Acoustics. Springer, Berlin, Heidelberg, 2005. p. 223-254.*

[6] *MANDEL, Michael I.; WEISS, Ron J.; ELLIS, Daniel PW. Model-based expectation-maximization source separation and localization. IEEE Transactions on Audio, Speech, and Language Processing, 2010, 18.2: 382-394.*

[7] *RAKERD, Brad; HARTMANN, William M. Localization of sound in rooms. V. Binaural coherence and human sensitivity to interaural time differences in noise. The Journal of the Acoustical Society of America, 2010, 128.5: 3052-3063.*

[8] *JORIS, Philip; YIN, Tom CT. A matter of time: internal delays in binaural processing. Trends in neurosciences, 2007, 30.2: 70-78.*

[9] *BAUMGARTNER, Robert; MAJDAK, Piotr; LABACK, Bernhard. Assessment of sagittal-plane sound localization performance in spatial-audio applications. In: The technology of binaural listening. Springer, Berlin, Heidelberg, 2013. p. 93-119.*

[10] *KWOK, Ngai M., et al. Sound source localization: microphone array design and evolutionary estimation. In: Industrial Technology, 2005. ICIT 2005. IEEE International Conference on. IEEE, 2005. p. 281-286.*

[11] *GoldWave - Audio & Video Editing Software and Fun Games, https://www.goldwave.com/, Last access Sept. 14th, 2018.*

[12] *IANTOVICS, Barna László. Agent-based medical diagnosis systems. Computing and Informatics, 2012, 27.4: 593-625.*

AUTOMATED INFORMATION SYSTEM FOR EVALUATION THE STABILITY OF THE SHIP

Emilia Koleva[1], Milena Lefterova[2], Mariya Nikolova[3]

N. Y. Vaptsarov NAVAL ACADEMY
73 V. Drumev St., Varna 9026, BULGARIA

E-mail: emilia_f@abv.bg[1]; mconsult.field@gmail.com[2]; mpn@abv.bg[3]

The paper is funded under the EU Project BG05M2OP001-2.009-0037-C01 "Support for the development of PhD students, post-doctoral students, young scientists and teachers from Naval Academy – Varna"

Abstract

The purpose of this paper is to present Automated Information System (AIS) used to evaluate the stability of a ship. The system is based on a new method for direct check of the ship's stability using the limited curves for the applicate of the center of gravity $\overline{KG}$ and the initial metacentric height $\overline{GM}$. The software provides an opportunity for buoyancy and stability evaluation of the ship in extreme situations. New recommend values for $\overline{GM}$ are set to minimize the human sickness, known as kinetosis. An advantage of the proposed and developed programming system is its work in interactive mode, in which there is a possibility to change the load on the ship from the command display.

1. INTRODUCTION

The safety of shipping is vital for the marine transport. When sailing each vessel is exposed to external forces like wind, heavy sea, surge and etc. Its safety depends on the seaworthiness qualities – buoyancy and stability. There is a growing need for opportunities for their current assessment in every moment, imposed by the circumstances.

In that matter there are new requirements for the software products on the board of the ship connected to the loading and the evaluation of the stability. After the enforcement of MARPOL Annex I, Regulation 28 and the resolution of Marine Environment Protection Committee [10] - MEPC.248(66) of the International Maritime Organization the ship owners are obliged to provide the necessary software on the board of the ship.

The resolution 66 of the Marine Environment Protection Committee (MEPC) is adopted on 04 April 2014 and entered into force on 01 January 2016. In accordance with the requirements of the resolution:

„All oil tankers shall be fitted with a stability instrument, capable of verifying compliance with intact and damage stability requirements approved by the Administration having regard to the performance standards recommended by the Organization." [4], [8], [9].

Oil tankers constructed before 1 January 2016 shall comply with this regulation at the first scheduled renewal survey of the ship after 1 January 2016 but not later than 1 January 2021.

Also statistics provided by IUMI, Global Marine Disaster Statistics and Lloyd Registry statistics show that the number of marine disasters and the magnitude of financial losses can be greatly reduced by ships modernization and the selection of trained and qualified crew. The use of information systems to assist the command staff in their day-to-day (routine) operations is also an opportunity in this direction.

2. AUTOMATED INFORMATION SYSTEM

The automated information system is based on a new method [2] [6], for the direct check of the ship's stability using the limited curves for the applicate of the center of gravity $\overline{KG}$ and the initial metacentric height $\overline{GM}$. The new method is based on the three-dimensional model of the hull form, mathematical model[7] for calculating the hydrostatic curves and $\overline{KN}$ – curves, the direct building of the static stability curves (SSC) and their normalization with the requirements of ISCode.

2.1. Software development environment

The software is realized in Matlab environment, version R2016b. One of the reasons for this choice is that Matlab is a software development environment that offers high-performance numerical computations (in this case the table of ordinates of the ship) and has a built-in function for 2D and 3D visualization.

2.2. Description of the software product

- The software uses the three-dimensional model of the hull, described by the expanded table of offsets, for receiving the hydrostatic curves. It gives the opportunity of plotting them not only when the ship is in normal condition, but when heeling and trim, leading to more accurate estimate of the stability of the ship. The hydrostatic curves are calculated for the trim range $\pm 1\% Lpp$. The received values could be displayed as graphics or in table form on the main screen of the software.
- The program calculates the $\overline{KN}$ – curves for the following operational trim range $\pm 1\% Lpp$. The received values could be displayed as graphics or in table form on the main screen of the software.
- Using the table of moments, a specific load on the ship could be set. The program calculates the current weight and the coordinates of the center of gravity of the ship for the current loading condition. The table with the new data is presented. There is a possibility of directly changing the load data in the table.
- The program system calculates the parameters of the equilibrium status of the ship and its initial stability. The received data is displayed.
- The righting arms are calculated and the static stability curves are built and displayed on the main screen of the program.
- The resulting data of all the calculations is stored in the programming environment.
- It is used to evaluate the intact stability of the ship in accordance with the requirements of IS-Code.
- The limited curves for maximal acceptable applicate's values of the center of gravity and minimum acceptable values of the initial metacentric height are built. The curves could be displayed at any time.
- The software could work also in an interactive mode. In this case changes could be made in the loading conditions from the command display.
- When the loading data is changed the system automatically updates the parameters of the equilibrium status of the ship and a new evaluation of the stability is made.
- In interactive mode some damage scenario (like flooding of separate cargo spaces) could be specified by the user from the main screen of the program. In this case the system evaluates the damage stability of the ship.

2.3. Description of the test ship used for the numerical research

The ship used for testing the automated system is chosen from the International Towing Tank Conference(ITTC) for the program SIMMAN[11]. The ship has a hull shape of a typical large tanker. (see Table 1).

Table 1. Main dimensions of the test ship

$Lpp = 320.00\ m$	Length between perpendiculars
$L_{WL} = 325.50\ m$	Length of waterline
$B = 58.00\ m$	Breadth of the ship
$D = 30.00\ m$	Depth of the ship
$d = 20.80\ m$	Draught of the ship
$V = 31262.00\ m^3$	Displacement of the ship
$C_B = 0.8098$	The block coefficient
$C_M = 0.9980$	Midship coefficient
$\upsilon_s = 15.50\ kn$	Speed of the ship

The exact 3D geometry of the ship hull is described by an expanded table of offsets. The table contains half-breadths measured at 65 stations and 200 control points (100 for each board) for each station.

On figure 1 is shown a 3D visualization of the test ship.

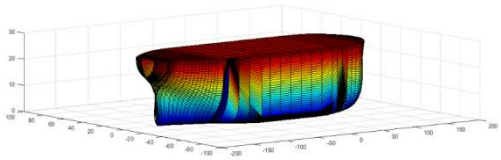

Figure 1. 3D visualization of the test ship

2.4. Validation and verification of the program product

The software calculates all necessary characteristics related to the buoyancy and stability of the ship. The validation of the obtained results is based on a comparison of the ship's seaworthiness quality –

buoyancy with the test ship data. For example, the estimated volume displacement of the ship for its projected draught differs from the one of the test ship by 0.1%, which is within the range recommended for analogue programming systems [3] - 2%.

2.5. Command display of the automated system

The main element of the automated information system is the command display. It consists of three panels. The first one contains tables, the second is graphical and visualizes the current static stability curve, and the third panel can visualize the hydrostatic curves, the $\overline{KN}$ – curves and the diagrams for maximal acceptable applicate's values of the center of gravity $\overline{KG}$ and minimum acceptable values of the initial metacentric height $\overline{GM}$ (see figure 2).

Changes to the table of moments can be entered from the command display (see figure 2). The system automatically checks for data entry irregularities, alerts for errors, and disables correction for light ship's data.

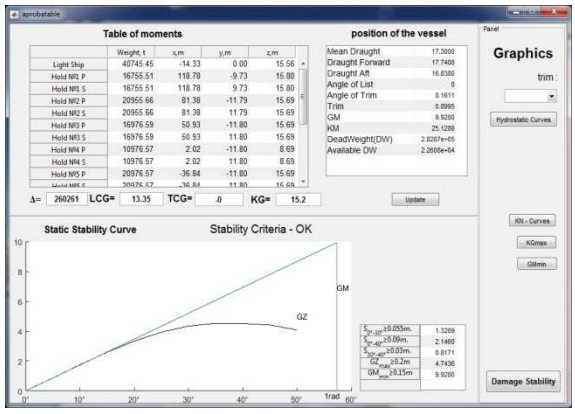

Figure 2. Command display of AIS

The changed loading data for a given compartment could be saved in the program environment after clicking the Update button. The system automatically updates the parameters of the equilibrium status of the ship and a new evaluation of the stability is made. A new SSC is generated according to the new condition. The current SSC of the ship is displayed for the assigned loading and its characteristics in accordance with the requirements of the IS Code.

The trim values ($t = -1, 0, 1, 2\ m$) could be selected from the third panel via drop-down menu and the corresponding hydrostatic curves and the $\overline{KN}$ – curves are displayed. The $\overline{KN}$ – curves for trim $t = 0\ m$ are shown on figure 3.

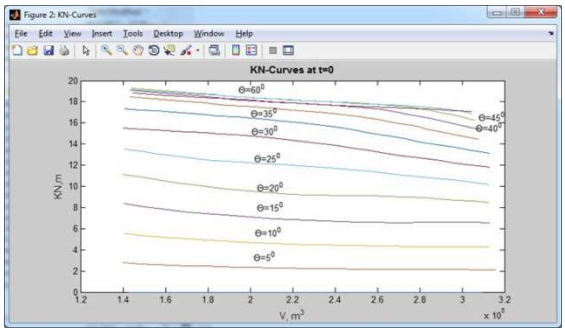

Figure 3. $\overline{KN}$ – curves for $t = 0\ m$

Notwithstanding the possibility of direct evaluation of the ship stability using the direct building of the SSC and its compliance with the requirements of ISCode, in the program system is integrated a program module for direct building of the limited curves for maximal acceptable applicate's values of the center of gravity $\overline{KG}$ (see figure 4) and minimum acceptable values of the initial metacentric height $\overline{GM}$ (see figure 5).

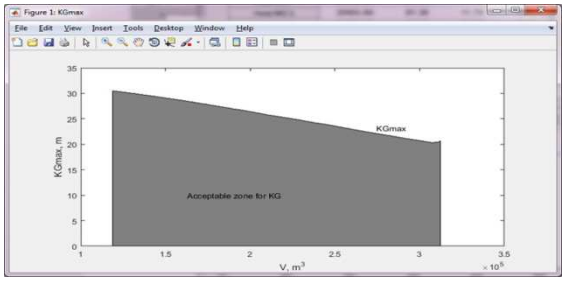

Figure 4. Limited curve for maximal acceptable $\overline{KG}$

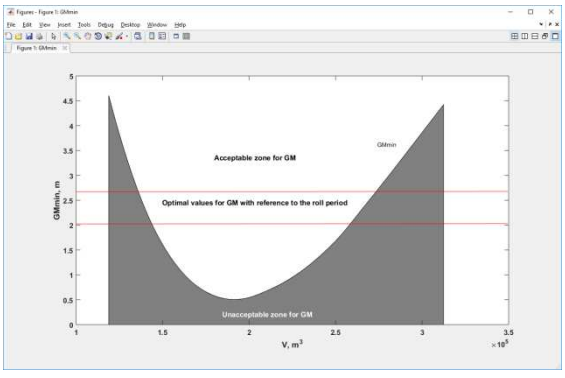

Figure 5. Limited curve for minimum acceptable $\overline{GM}$

If the calculated values for $\overline{KG}$ and $\overline{GM}$ for a given displacement are in the acceptable zones of the corresponding diagrams, the ship is considered to be stable. The limited curves meet all the requirements of ISCode. They give the opportunity for

direct evaluation of the ship stability (without building the SSC) for the chosen loading condition.

The stability of the ship, as one of its important seaworthiness qualities, is closely related to the life aboard the ship. Excessive stability leads to intense and sharp fluctuations during navigation. As a result, there are a number of negative consequences for the human body ("kinetosis"). In maritime practice this state is known as sea sickness. By choosing optimal values of ship characteristics, the kinetic symptoms can be significantly reduced. For the purpose additional curves are built in the programming system, to the abovementioned limiting curve $\overline{GM}$. They are used to define an optimal zone for stability characteristics guaranteeing minimal manifestations of sea sickness.

It's well known that the main problem with the oscillating movements that the ship performs during sailing is the intensity of rolling. The average values of natural roll frequency for different kinds of marine ships are:

Marine transport vessels: 7–12s.
Large passenger ships: 16–20s.
Passenger ship (up to 10000 t.): 10–15s.
Tugboats and fishing vessels: 6–10s.

These values are obtained by (1). The formula presented the direct relationship between the metacentric height and the roll period.

$$T_\theta = \sqrt{\frac{I_x + \lambda_{44}}{\Delta g \overline{GM}}}\,, \qquad (1)$$

where:

T_θ - rolling period,

I_x - the transverse moment of ship inertia,

λ_{44} - the moment of added mass due to water dragging by the rolling hull,

Δ - weight of the vessel.

The values of I_x and λ_{44} are calculated in the table of moments of the AIS.

After applying formula (1), two red straight lines corresponding to $\overline{GM} = 2{,}02\ m$ and $\overline{GM} = 2{,}63\ m$ are build. They are shown on figure 5. The first value is for a roll period $T_\theta = 12\ s$, and the second one for $T_\theta = 7\ s$. Choosing a value for $\overline{GM}$ between the two bars guarantees smooth fluctuating movements with a period in the required range. From the figure it is apparent that it is not possible to select such values for some displacements of the ship.

2.6. Application of the AIS

The program system is applicable to different types of marine transport vessels.

The software is built in a way that takes into account the specifics of a particular ship. It is possible to use it as an OBSS as well as in a separate operating center.

The program system could work in two modes:

- Assessment of stability parameters and ship's equilibrium status for different load cases based on the hydrostatic data, stored in the program environment, including different load cases preview prior to the actual loading of the ship.
- Working in interactive mode. In this case, the changes in the table of moments might be inputted from the command display, including imitation of extreme situations associated with flooding of individual compartments and tanks in the ship.

Expansion of the capabilities of the programming system is foreseen by an additional module allowing the capture of signals from sensors located in the ship's hull and receiving the data for the current ship's loading.

3. CONCLUSION

The system is applicable to different types of marine transport vessels and the software is built in a way that takes into account the specifics of a particular ship.

The programming system enables the assessment of buoyancy and stability during the exploitation and simulates extreme situations.

The program system allows users to choose an optimal value for $\overline{GM}$ with reference to the roll period, guaranteeing minimal manifestations of sea sickness.

An advantage of the proposed and developed programming system is its work in interactive mode, in which there is a possibility to change the load on the ship from the command display.

The software could be used as an OBSS, in a separate operating center and in the educational program for marine cadets.

References

[1] *A. Biran and R. Pulido, "Ship Hydrostatics and Stability", 2nd edn, Butterworth-Heinemann, 2013*

[2] *M. Eremieva, V. Sabeva, M. Nikolova, and E. Koleva, "Method for calculating the stability at moderate and big heeling angles of a vessel"", XLVII International Scientific Conference on Information, Communication and Energy Systems and Technologies ICEST 2012, Proceedings of papers, vol.1,p.263-264.*

[3] *Guidelines for Loading Computer Systems, Germanischer Lloyd SE, Hamburg, 2013*

[4] *International Code on Intact Stability, 2008*

[5] *E. Koleva, Doctorate thesis: Automated information system for evaluation the stability of marine transport vessels , 2017*

[6] *E. Koleva, M. Nikolova, M. Eremieva, and V. Sabeva, "An algorithm and a program module for calculating the border height of the mass centre of a vessel", XLVII International Scientific Conference on Information, Communication and Energy Systems and Technologies ICEST 2012, Proceedings of papers, vol.1,p.159-162.*

[7] *E. Koleva, M. Lefterova, and M. Nikolova, "Evaluation of Ships Stability using Matlab" Days of Mechanics, Varna, 2017, Journal "Mechanic of machinery", book 1, Technical university - Varna, p.94- 98, 2017*

[8] *MSC.1/Circ.1229 "Guideline for Scope of Damage Stability Verification on new oil tankers, chemical tankers and gas carriers"*

[9] *MSC.1/Circ.1461 "Guidelines for verification of damage stability requirements for tankers", 8 July 2003*

[10] *MEPC.248 (66) – Marine Environment Protection Committee (MERC)*

[11] *www.simman2008.dk*

DETECTING CONTOURS OF PATHOLOGICAL FORMS IN COLONOSCOPY IMAGES USING A HYBRID METHOD

Veska Georgieva, Plamen Petrov

Technical University of Sofia, Bulgaria
Sofia 1000, 8 Kl. Ohridski Blvd.
T. +359 (2) 965-3293;
E. vesg@tu-sofia.bg, ppetrov@tu-sofia.bg

Szilvia Nagy, Brigita Sziová

Széchenyi István University, Hungary
H-9026 Győr, Egyetem tér 1.
T.+36 (96) 613 773; F.+36 (96) 613 694;
E. nagysz@sze.hu, szi.brigitta@sze.hu

Abstract

As colonoscopy is needed for screening colorectal polyps, and the first step of classification these polyps is recognizing them, it is worth to research, whether the colonoscopy databases could be improved by image processing and contour detection. In the following considerations a reflection filtering and background subtraction with large-sized mean filter is used as image preprocessing tools, and hybrid method for segmentation of pathological forms, based on template matching and active contour model as contour fitting for segmentation of the image is made.

1. INTRODUCTION

As in the past couple of decades colorectal cancer advanced to one of the leading cause of death, it would be very useful if population wide screening could be carried out. As types of colorectal cancers [1] all develop from polyps inside the bowel, and these warts can be seen by colonoscope at very early stage, colonoscopy is probably the best and least intrusive method for detecting colorectal polyps. The alternatives, capsular endoscopy [2] and virtual colonoscopy are either much harder to process or have higher risk. Colonoscopy nowadays has several image enhancing tools, such as chromoendoscopy or narrow band imaging [3]. If the polyps are found, the medical experts can determine whether biopsy or removing of the polyp is necessary based on their shape [4,5], colour and Kudo's pit pattern classification scheme [6-8]. In the past years several groups started to develop tools for the medical staff in order to help drawing their attention to those domains of the endoscopy picture, where some pathological forms, such as polyps are likely [9]. Some of them made their databases available [9-12], too. These databases consist of pictures, which are taken by colonoscopies also there are masks, corresponding to the pictures and showing the areas of the polyps.

There are number of polyp segmentation methods, which have been reported in the literature [13]. Canny operator and the Radon transform are used to detect polyp boundaries [14]. Using structural entropy a fuzzy decision method for finding polyps is developed [15]. An adaptive deformable model is used to present segmented polyps [16]. Geodesic active contours with a modified speed function on the colon surface are evolved to detect polyp neck regions [17]. By using level-set method and active contour model without edges the polyp mass region is extracted [18, 19].

In the following considerations first the image preprocessing stage is presented in Section 2, then a brief survey about the proposed hybrid method, based on template matching and active contour model is given, and as a last step, in Section 4, some results of segmentation are presented.

2. CALCULATION OF THE REFLECTION DOMAINS AND THE BACKGROUND FOR SUBTRACTION

For the present study images of database built at ETIS Larib [10] are used, as these images have high resolution and low noise. As it can be seen in Fig. 1, the image is mainly of pinkish colour, its histograms have large empty domains between the important information of the image, i.e., the middle

region and the absolutely light (reflections) and absolutely dark (frame) ends in all three colour channels. The first step of pre-processing is to remove the black frame of the picture in a rectangle, the corners remain black. This can be seen in Fig.1. The cropped image is studied in the followings.

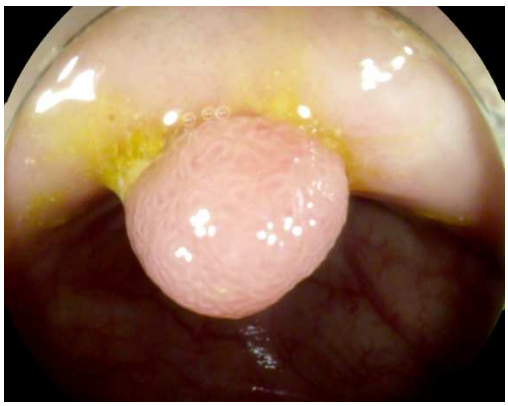

Figure 1. The original colonoscopy image number 66 of ETIS Larib [10]

Next, using the histogram, an automatic threshold is set both in the dark and in the light end of the histogram at the point it starts to increase after the first peak. At these new thresholds the histograms of R,G and B channels are cut, and the 3 histograms are renormalized to the 0- 255 domain. These histograms are presented in Fig. 2.

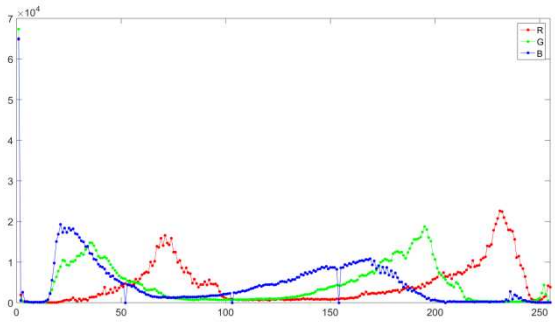

Figure 2. Histograms of the image

Those points, which used to have darker shades than the minimum of the new histogram, are collected to a mask for the black points, and the ones that used to have lighter shade then the maximum of the new histogram are collected in the white mask. The masks are treated together, when average is calculated, i.e., all the masked points are excluded from the averages. Both masks are extended in such a manner, that if points differ more than a threshold from their neighbours' average, then they are given to the masks. If the brightness value of a point is higher than the masked average of the environment, then the point will belong to the white mask, if lower, to the black mask.

As a next step, the white mask is used for creating the matrix, which has to be subtracted from the histogram-stretched image so, that the obtained image would be reflection-free. This mask image is presented in Fig. 3. The resulting image, which was obtained after mean filtering around the masks, is presented in Figure 4.

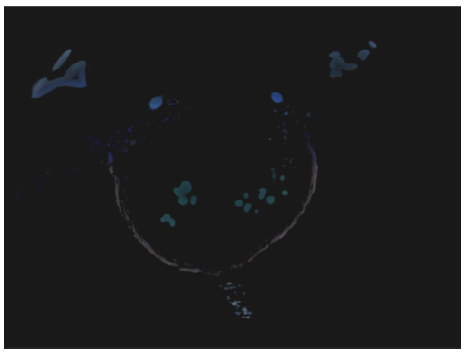

Figure 3. The white mask

Figure 4. Reflection-free image

As a last step, the images are filtered with a very large mean filter (not masked) in order to receive the background and this background is subtracted from the reflection-free image. The background is shown in Fig. 5, while the final result is given in Fig. 6.

Figure 5. Background of the image

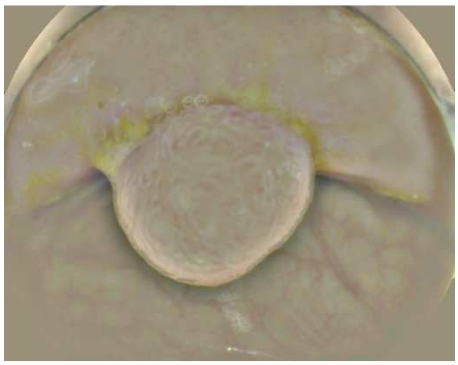

Figure 6. The background subtracted version of the image

3. CONTOUR DETECTION OF THE POLYPS BY HYBRID METHOD

The colorectal polyp segmentation is made by the implementation of the Chan and Vese active contour model [20]. In this case, the stopping term does not depend on the gradient of the image, as in the classical active contour models, but is instead related to a particular segmentation of the image. This method of segmentation is based on active contour without edges. We propose to use the given mask from database, which corresponds to the image and showing the area of the polyp. This mask is a template for the shape form of the initial contour, from which the contour segmentation begins. It is presented in Fig. 7.

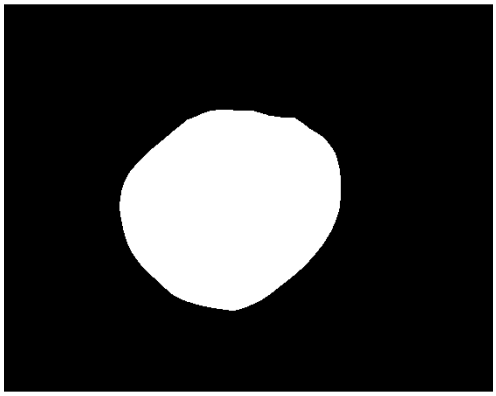

Figure 7. Mask from database showing the area of the polyp

4. RESULTS AND VALIDATION

The formulated stages of processing are realized by computer simulation in MATLAB 7.14 environment by using IMAGE PROCESSING Toolbox. For the experiments 200 images with size 1216x962 pixels in tif format of database built at ETIS Larib are used. The grayscale colorectal image with segmented polyp in yellow colour is shown in Fig. 8. The segmentation is performed by 200 iterations.

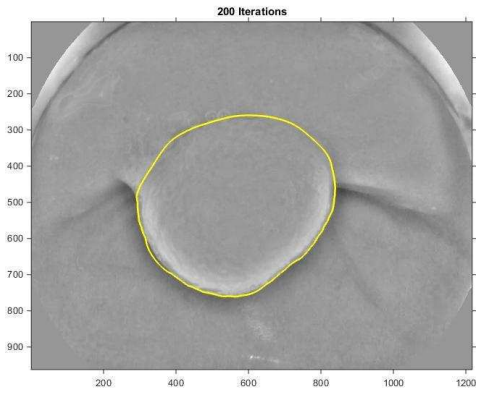

Figure 8. Grayscale colorectal image with segmented polyp

For validation of the segmentation results, we compute the undirected partial Hausdorff distance between the boundary of the segmentation with the hybrid method and the boundary of the manually-segmented ground truth. The obtained results are compared to the results from segmentation without pre-processing stage. The averaging results for the partial Hausdorff distance between automatic segmentation and the manually-segmented ground truth are given in Table 1. The grayscale colorectal image with segmented polyp in yellow colour without using pre-processing stage is presented in Fig. 9.

Table 1. Partial Hausdorff Distance

Method	K [%]
Manually-segmentation without pre-processing stage	72.9
Automatic segmentation by hybrid method without pre-processing stage	76.5
Manually-segmentation with pre-processing stage	92.3
Automatic segmentation by hybrid method with pre-processing stage	95.7

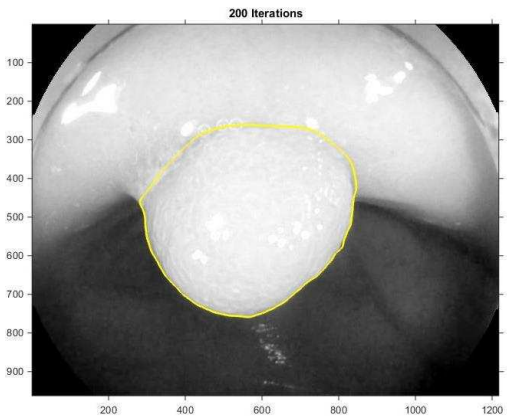

Figure 9. Grayscale colorectal image with segmented polyp without pre-processing stage

These results have indicated that the segmentation is better in the case of the proposed approach

compared to manually segmentation. On the other hand, the application of the pre-processing stage with a reflection filtering and background subtraction increases the accuracy of defining the contour of the polyp and allows visual observation of the structure and appearance of its surface.

5. CONCLUSION

In this paper, an effective approach for automatic colorectal polyps segmentation is proposed. The pre-processing stage is applied for calculation of the reflection domains and for background substraction. Then the reflection-free image was processed by mean filter in order to receive the background and this background is subtracted from the reflection-free image. The contour of the polyp was detected using hybrid method. It is based on template matching and active contour model without edges.

The proposed approach can be applied for screening of early colorectal carcinoma, especially by sigle colorectal polyps. It can be used also in monitoring the disease progression.

References

[1] *K. Soreide, B.S. Nedrebo, A. Reite et al., "Endoscopy Morphology, Morphometry and Molecular Markers: Predicting Cancer Risk in Colorectal Adenoma", Expert Rev. Mol. Diagn, Volume 9, Taylor&Francis, London, 2009, pp. 125-137.*

[2] *J. J. W. Tischendorf, H. E. Wasmuth, A. Koch, H. Hecker, C. Trautwein, and R. Winograd, "Value of magnifying chromoendoscopy and narrow band imaging (NBI) in classifying colorectal polyps: a prospective controlled study", Endoscopy, Volume 39, Thieme, Stuttgart-New York, 2007, pp. 1092-1096.*

[3] *I. Rácz, M. Jánoki, and H. Saleh, "Colon Cancer Detection by 'Rendezvous Colonoscopy': Successful Removal of Stuck Colon Capsule by Conventional Colonoscopy", Case Rep. Gastroenterol., Volume 4, Karger, Basel, 2010, pp. 19–24.*

[4] *J. R. Jass, "Classification of colorectal cancer based on correlation of clinical, morphological and molecular features", Histopathology, Volume 50, Wiley, Hoboken, 2006, pp. 113–130.*

[5] *I. Rácz, A. Horváth, M. Szalai, et al., "Digital Image Processing Software for Predicting the Histology of Small Colorectal Polyps by Using Narrow-Band Imaging Magnifying Colonoscopy", Gastrointestinal Endoscopy, Volume 81, Elsevier, New York, 2015, p. 259.*

[6] *S. Kudo, S. Hirota, T. Nakajima, et al., "Colorectal tumours and pit pattern". J Clin Pathol, Volume 47, BMJ Journals, London,1994, pp.880-885.*

[7] *S. Kudo, S. Tamura, T. Nakajima, et al. "Diagnosis of colorectal tumorous lesions by magnifying endoscopy". Gastrointest Endosc, Volume 44, Elsevier, New York, 1996, pp. 8-14.*

[8] *S. Kudo, C.A. Rubio, C.R., Teixeira, et al. "Pit pattern in colorectal neoplasia: endoscopic magnifying view". Endoscopy, Volume 33, Thieme, Stuttgart-New York, 2001, pp. 367-373.*

[9] *Jorge Bernal, et al., "Comparative Validation of Polyp Detection Methods in Video Colonoscopy: Results from the MICCAI 2015 Endoscopic Vision Challenge". IEEE Transactions on Medical Imaging, Volume 36, IEEE, Piscataway, 2017, pp. 1231–1249.*

[10] *J.S. Silva, A. Histace, O. Romain, et al., "Towards embedded detection of polyps in WCE images for early diagnosis of colorectal cancer", Int J Comput Assisted Radiology and Surgery, Volume 9, Springer, Berlin, 2014, pp. 283-293.*

[11] *J. Bernal, F. J. Sanchez, F. Vilarino. "Towards Automatic Polyp Detection with a Polyp Appearance Model", Pattern Recognition, Volume 45, Elsevier, New York, 2012, pp. 3166–3182.*

[12] *J. Bernal, F. J. Sanchez, G. Fernández-Esparrach, et al., "WM-DOVA maps for accurate polyp highlighting in colonoscopy: Validation vs. saliency maps from physicians", Computerized Medical Imaging and Graphics, Volume 43, Elsevier, New York, 2015, pp. 99-111.*

[13] *V. B. Surya Prasath, "Polyp Detection and Segmentation from Video Capsule Endoscopy: A Review", Journal of Imaging, vol.3, issue 1, pp.1-15, 2017.*

[14] *A.K Jerebko, S.Teerlink, M. Franaszek, R.M. Summers, "Polyp segmentation method for CT Colonography computer-aided detection", SPIE Medical Imaging, 5031, pp.359–369, 2003.*

[15] *S. Nagy, F.Lilic. L.Koszy, "Entropy based fuzzy classification and detection aid for colorectal polyps", IEEE AFRICON 2017, Cape Town, South Africa pp.78-83, 2017.*

[16] *J. Yao, R.M Summers, "Adaptive deformable model for colonic polyp segmentation and measurement on CT Colonography", Medical physics 34, pp. 1655–1664, 2007.*

[17] *S. Tan, S., Yao, J., Ward, R.M., Summers, "Linear measurement of polyps in CT Colonography using level sets on 3D surfaces", In: Engineering in Medicine and Biology Society, Annual International Conference of the IEEE, pp. 3617–3620, 2009.*

[18] *J.J.Näppi, H.Frimmel, A.H. Dachman, H.Yoshida, "Computerized detection of colorectal masses in CT Colonography based on fuzzy merging and wall-thickening analysis", Medical physics 31, pp. 860–872, 2004.*

[19] *V.Georgieva, P.Petrov," An Approach for Colorectal Polyp Segmentation", 12th International Conference on Communications, Electromagnetics and Medical Applications (CEMA'17), Sofia, Bulgaria, pp. 1-5, 2017.*

[20] *T. Chan, L.Vese, "Active Contours Without Edges", IEEE Transactions on Image Processing, vol.10, № 2, pp.266-276, 2001.*

GUI FOR SPLEEN SEGMENTATION FROM ABDOMINAL MRI SEQUENCES

Antonia Mihaylova

Technical University of Sofia, St. Kliment Ohridski 8
e-mail: antonianankova@gmail.com

Abstract

Nowadays the medical images processing is an important step to the modern computer aided medical diagnostic. Specialists such as radiologists, surgeons and other are able to use several of medical image diagnostics in their work. But not always the medical equipment has the image processing tools that the doctors need. For that reason a Genuine User Interface (GUI) for Spleen Segmentation of abdominal MRI sequences is proposed in this paper. It works in the MATLAB environment and uses its Image processing toolbox. The interface is giving a choice between different techniques of segmentation based on active contours without edges and other image processing tools. The main advantage of the GUI is the possibility of automatic segmentation of a whole abdominal MRI sequence that is loaded from the user. Other important operations are image pre-processing (Optional), 3D visualisation of the results and validation of the segmentation, if their ground true images are available.

1. INTRODUCTION

The shape and volume of the human organs are very important for studying their functionality, making statistical representation of the normal and disordered organs by the human populations. By epidemiological studies and in the daily work radiologists are sometimes forced to do hundreds of manual segmentations per hand. That is way a tool for automatic or semi-automatic spleen segmentation could be very useful in such cases.

The form of the human spleen is very variable by the different individuals. So the visualization of this organ is very interesting and helpful by studying its shape, functionality and disorders. The spleen has the same relationship to the circulatory system that the lymph nodes have to the lymphatic system [1]. A wide range of diseases can affect the spleen. MR imaging is an excellent tool for diagnosis and evaluation of focal lesions and pathologic conditions of the spleen. Also for studies of health, because of the harmless magnetic field that is used by MRI.

There are a lot of segmentation techniques, but not all of them are giving good results in the different cases. Because of the partial volume effect, the gray level of the spleen and grayscale similarity of the adjacent abdominal fat, spleen segmentation has always been a problem [2]. In this case an active contour method for segmentation has been chosen. The "Active Contours Without Edges" by Chan and Vese, that ignores edges completely [3].

The performance of the image and video segmentation algorithms is judged mainly on how well the region is segmented. Generally there exists no segmentation algorithm which can be commonly applied on all the domains [20].

The outline of the research paper is organized as follows: Section 2 discusses about image segmentation based on "Active Contours Without Edges" by Chan and Vese, also presents combination of the active contour model with other segmentation methods, such as K-mean clustering as primary segmentation, atlas template method with automatic match of the used template and demonstrates the results. Section 3 describes the proposed GUI for image segmentation and its functionalities. The results of the relative evaluation methods are illustrated in section 4 and section 5 finally draws the concluding remarks of the paper.

2. SPLEEN SEGMENTATION METHODS

2.1. The active contour model by Chan and Vese

All of the methods in the GUI are based on the segmentation via active contours without edges. The active contour model of Chan and Vese is used for the next two stages of segmentation. It is a gray level based method and is a special case of the Mumford–Shah function.

We consider f to be the given grayscale image on a domain Ω to be segmented. Mumford and Shah approximate the image f by a piecewise-smooth function u as the solution of the minimization problem. The Chan - Vese model has an additional term penalizing the enclosed area and a further simplification that u is allowed to have only two values,

c_1 where x is inside C and c_1 where x is inside C, where C is the boundary of a closed set and c_1, c_2 are the values of u respectively inside and outside of C [8]. By the method of Chan – Vese the purpose is to find among all u of this from the one that best approximates f.

2.2. Hybrid approach for spleen segmentation

For the fully automated mode of the GUI is used a hybrid method for spleen segmentation from MRI sequences that is presented in a previous work [21]. The approach is combining K-mean clustering for primary segmentation of the image sequence and an atlas template method is used for the primary segmentation of the primary image of the sequence, where the segmentation begins.

K-means clustering can be used because it is simple and has relatively low computational complexity [15]. So we can obtain two clusters. The first cluster image presents the background and some small structures extracted from the image. The second one presents the MR image with extracted organs and tissues. This cluster image shows a better differentiation between the spleen and the surrounding area. The goal of a clustering method is to find cluster centers $CC = \{c_1, \ldots c_K\}$ in feature space such that the distance of all samples to their center is minimal [11]:

$$CC_{min} = \arg\min_{CC} d_{CC}(f) = \arg\min_{CC} \sum_{i=1}^{M} ||f_i - c(f_i)||$$

where $c(fi)$ delivers the cluster center c_k, which is closest to f_i.

Two atlas models of the spleen have been made and one of them is used for initial contour in the segmentation of the initial image. They are created up of 10 abdominal MRI images, which are our training data and are different from the test data. First, the spleen was manually segmented from these 10 images. After that we get 10 binary images. In the next step the spleen is surrounded in a rectangle and cut off. These cuts are rescaled to 50x50 pixels. Then we find the intersection and union of the scaled images, which presented two atlas models given in Fig. 1.

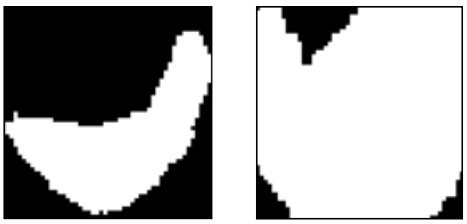

a b

Figure 1. Spleen atlas models: a) obtained after intersection of the scaled images; b) obtained by union of the scaled images

2.3. Automatic segmentation of the whole sequence

The sequence is processed in two directions (forwards and backwards from the initial image). That means we can build two loops: one incrementing and other decrementing to craw the array of images with spleen in the sequence. This approach is appropriate, because in the most cases the spleen is getting smaller in these two directions in the sequence. Each image could be primarily pre-processed and pre-segmented using the methods descrybed in the previous subsection 2.2, if the user chooses this kind of segmentation. If not an initial contour could be chosen in the initial image as a rectangle without a template or as a polygonal figure closer to the spleen. Each subsequent image uses as mask for its segmentation with active contours without edges the result of the segmentation of the previous image [14]. For termination condition we use the difference between the segmentation result in the initial image and the segmentation in each processed image in the sequence. This is made on the base of the correlation function. This function gives the statistical correlation between random variables, contingent on the spatial or temporal distance between those variables. By value of 1 there is 100% matching between the images. In our case we select the value of the threshold equal to 0.65.

The segmented spleen is visualized with yellow contour on the original images from the entire sequence. The result is a new sequence of binary images of the segmented spleen, saved in a new file folder in the folder of the original file with the sequence.

3. FUNCTIONALITY OF THE GUI FOR SPLEEN SEGMENTATION

A view of the GUI is given in Fig. 2. The main algorithm of the GUI is presented in Fig. 3 [01]. It describes the flowchart of the main interactions without observation of the different segmentation abilities and other optional options of the GUI.

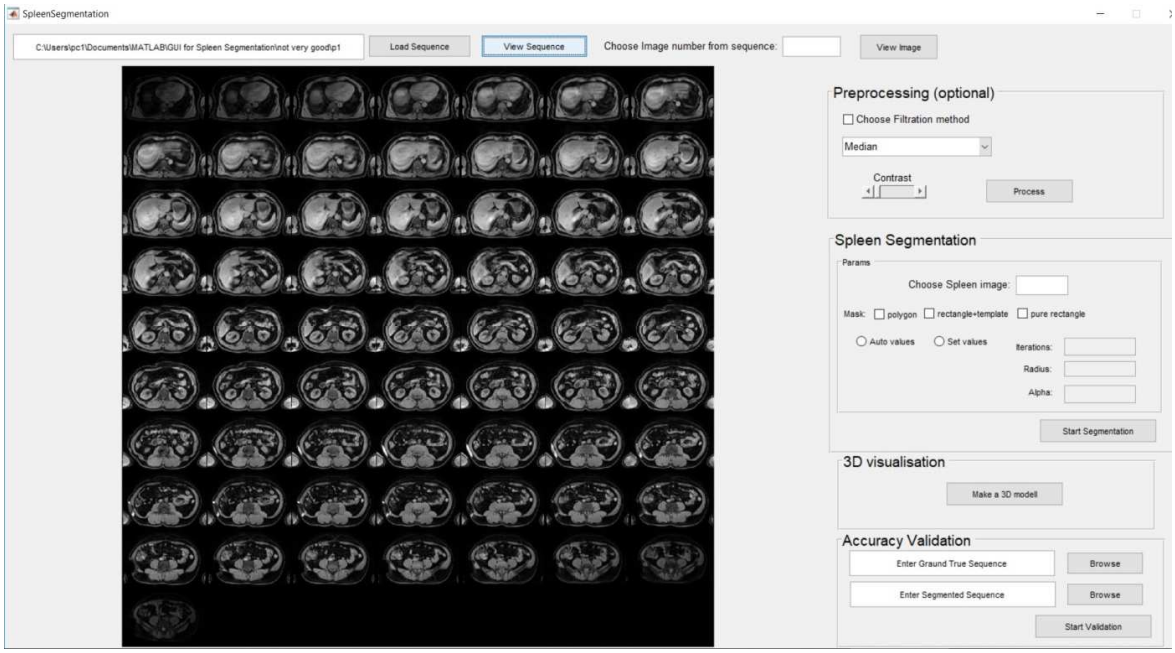

Figure 2. Main view of the GUI

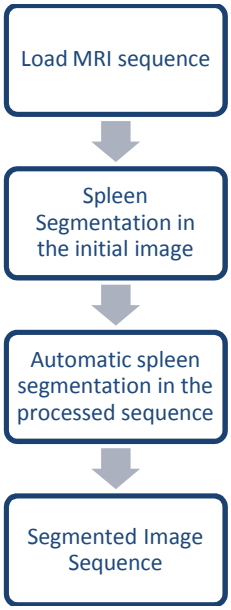

Figure 3. Flowchart of the main algorithm

The first step in the segmentation process is to load an abdominal MRI-sequence from a file that should be segmented. This happens by pushing a button "Load sequence" on the upper left corner in the GUI. After that the sequence should be visualized with the button "View sequence" next to the previous one. After this interaction the whole sequence is visualized in the visualisation sector of the GUI. In that way the radiologist can make the important and expert decision in which of the images the spleen is visible and to choose one of them as initial image for the automatic segmentation of the rest of them. The chosen image is given with its number in the "Spleen Segmentation" field next to the visualized sequence.

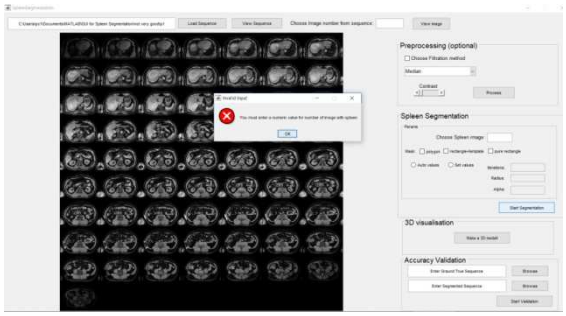

Figure 4. Error report for non existing image number

An error report acquired, when such image is not given and segmentation is tried to be done. There is also an optional field for pre-processing, where various filters could be chosen from the pop-up-menu and contrast enhancement could be provided to all of the images in the sequence before the segmentation step. Other additional fields are "3D visualisation" and "Accuracy Validation".

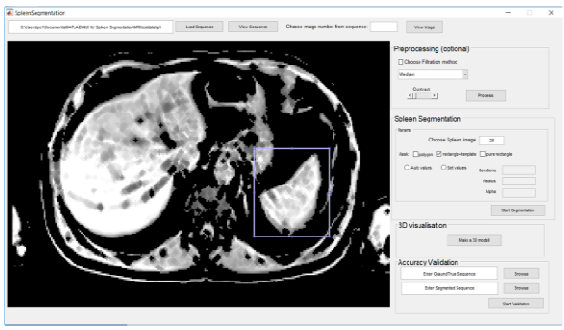

Figure 5. Start of segmentation with chosen option 'rectangle+template'

4. RESULTS AND DISCUSSION

On Table 1 are presented the results after comparing the accuracy of the segmentation results obtained by using the different segmentation methods that could be chosen with check boxes in the GUI.

Table 1. Obtained results for spleen segmentation made by different segmentation options

Segmentation options	Mean Dice for the sequence [%]	Dice for the primary image [%]	Time for processing of the sequence [sec]	Time for processing of primary image [sec]
'rectangle+ template '	89.14	94.06	41.33	20.34
'polygogon'	79.83	95.14	42.72	25.43
'pure rectangle'	75.62	83.45	43.45	53.75

5. CONCLUSION

In this paper is presented an effective GUI for easily automatic spleen segmentation in abdominal MRI sequence images. The proposed GUI represent different approaches for spleen segmentation all based on the active contour model. Hybrid segmentation approach on segmentation methods such as active contours without edges and k-mean clustering is compared with the other segmentation options. The proposed GUI allows extracting in short time the normal spleen, which has a variable form and unstable position at the different images in the MRI sequence. The various options of the GUI could give also the ability of making segmentation of some untypical or pathological forms of the spleen, but more experiments should be done in the future in this direction.

References

[1] *Bai, X.Z. and Zhou, F.G. 'Multi Structuring Element Top-Hat Transform to Detect Linear Features', 10th International onference on Signal Processing, 2010, 877-880.*

[2] *Behrad, A., Masoumi, H., 'Automatic Spleen Segmentation in MRI Images using a Combined Neural Network and Recursive Watershed Transform', IEEE 10th Symposium on neural network applications in Electrical Engineering, Belgrade, Serbia, 2010.*

[3] *Bland, JM, Altman, DG., 'Statistical methods for assessing agreement between two methods of clinical measurement', Lancet 1:307–310, 1986*

[4] *Chan T., Vese L., 'Active Contours without Edges', IEEE Transactions on Image Processing, 10(2):266-276, 2001.*

[5] *CMicrotek[online]http://cmicrotek.com/wordpress_ 159256135/ Retrieved 12August 2015.*

[6] *Farraher, F., Jara, H., Chang, K., Hou, A., Soto, B., ' Liver and Spleen Volumetry with Quantitative MR Imaging and Dual-Space Clustering Segmentation', From the 2003 RSNA Annual Meeting, pp. 322-328, 2004.*

[7] *Firoz, R., Shahjahan, Md., Ali, M. Nasir Uddin Khan, Khalid Hossain, Khairul Islam, Shahinuzzaman, 'Medical Image Enhancement Using Morphological Transformation', Available from: https://www.researchgate.net/publication/288496902.*

[8] *Georgieva, V. , "An Influence of the Structuring Element on Morphological Filtering for Medical Image Enhancement", Proceedings ICEST'2009, Vol.2, pp. 435-438, V. Tarnovo, Bulgaria, 2009*

[9] *Georgieva, V., Ermakov, S., 'GUI for CT Image Segmentation via Active Contours', IEEE 4th International Black Sea Conference on Communications and Networking (BlackSeaCom), DOI: 10.1109/BlackSeaCom.2016.7901555, pp.1-5, 2016.*

[10] *Getreuer P., 'Chan and Vese Segmentation', In: Image Processing On Line, IPOL 2012-08-08, Yale University, 2 012, p. 214-224.*

[11] *Hegenscheid K., Kühn J. P., Völzke H., Biffar R., Hosten N., Puls R., 'Whole-Body Magnetic Resonance Imaging of Healthy Volunteers: Pilot Study Results from the Population-Based SHIP Study', Rapid Communication, Georg Thieme Verlag KG Stuttgart · New York, DOI 10.1055/s-0028-1109510, 2009; 181: 748–759.*

[12] *Jiang H., Ma Z., Zhang B., Zhang, Y., 'A Spleen Segmentation Method Based on PCAISO', **IEEE** 6th International Conference on Computer Sciences and Convergence Information Technology (ICCIT) Seogwipo, South Korea, pp 928-933, 2011.*

[13] *Mihaylova, A., Georgieva, V., 'A Brief Survey of Spleen Segmentation in MRI and CT Images', International Journal of Advances in Computer Science and Technology (IJACST) 2016, 5(7):72-77.*

[14] *Mihaylova, A., Georgieva, V., 'Spleen segmentation in MRI sequence images using template matching and active contours', Proceeding of International Congress of Information and Communication Technology (ICICT 2018), China, in print*

[15] *Ng, H.P., Ong, S.H., Foong, K.W.C., Goh, P.S., Nowinski, W.L., 'Medical Image Segmentation Using K-Means Clustering and Improved Watershed Algorithm', Available from: https://www.researchgate.net/publication/4243554.*

[16] *Osher S., Sethian J.A., 'Fronts propagating with curvature-dependent speed: Algorithms based on Hamilton-Jacobi formulations', Journal of Computational Ph ysics, 1988, 79(1):12- 49.*

[17] *Pohle, R., Computer-aided image analysis for the evaluation of medical image data, habilitation writing to obtain the Venia legendi for Computer Science, accepted by the Faculty of Computer Science of the Otto von Guericke University Magdeburg, 2004.*

[18] *Toennies, K. D., 'Guide to Medical Image Analysis, Methods and Algorithms', Advances in Computer Vision and Pattern Recognition, Springer 2012, ISSN 2191-6594*

[19] *Völzke, H., 'Cohort Profile: The Study of Health in Pomerania', International Journal of Epidemiology ,2011, 40:294–307*

[20] *Anuradha.S.G, K.Karibasappa, B.Eswar Reddy, 'Target Seg: A GUI for Image Segmentation using Morphogical Watershed and Graph cut Techniques', International Journal of Signal Processing, Image Processing and Pattern Recognition Vol.9, No.3 (2016), pp.167-178 http://dx.doi.org/10.14257/ijsip.2016.9.3.15*

[21] *Antonia Mihaylova, Veska Georgieva and Plamen Petrov (2018) 'Multistage approach for automatic spleen segmentation in MRI sequences', IJRIS'18 - in print.*

THE DIGITAL IMAGE CLASSIFICATION BASED ON CALCULATION OF RENYI DIVERGENCE

V. D. Sergeev

Saint-Petersburg State University, Math.& Mech. faculty,

Email: vlad.sergeev.spbgu@gmail.com

Abstract

The method of analysis and classification of images based on the calculation of alpha-divergences (or Renyi's divergences) is considered. For each image we construct a discrete measure distribution and finite sequence of its direct multifractal transforms. The resulting vector is a characteristic of the image structure. For two images, the α-divergences between these vectors are calculated. We perform experiments and provide results with several classifiers that use these vectors as training and testing datasets.

1. INTRODUCTION

Image analysis and classification play a special role in biology and medicine because this is the one of the main ways to observe the system under investigation. The results of observations can be saved as digital images.

The characteristics of a digital image can naturally be determined in terms of intensities of its constituent pixels. One of the well-known methods consists of dividing the image into cells and calculating certain measures defined on this partition. The easiest way to determine the measure of a cell is to calculate the sum of its pixel intensities, but it is also possible to apply different filters. The measure for color images may be defined for any of the palette component.

The measure distribution in cells allows the use of entropy characteristics for the analysis and classification of images. The natural characteristic is the entropy of the partition [3], which is defined as $-\sum_i \mu_i \ln\mu_i$, where i — is the number of elements in the partition, and $\boldsymbol{\mu_i}$ is the measure of i*th* cell. The entropy of a partition is sometimes called the entropy of a probability vector or the Shannon entropy. This entropy is a special case of the class of Renyi entropies — a set of characteristics depending on a real parameter. The Renyi entropies are widely used both in image analysis, and as objective functions in solving problems of isolated extremums [2,4].

The calculation of entropy allows us to obtain certain digital characteristic of an image. At the same time, it should be noted that the entropy value does not depend on the order of the component of the probability distribution vector. Therefore images with different structures may have different distribution vectors, but if one vector is a permutation of components of another, the entropies of these vectors will be the same.

To find the difference in the structure of the compared images one may calculate Renyi's divergence. The Kulbak-Leibler divergence is the most commonly used. It is not enough to obtain one numerical characteristic for image classification, so the methods which allow us to obtain several numerical characteristics are more preferable. Resulting vectors allow us to find rather subtle differences in the structure of images.

In this paper, we consider a method of obtaining vector characteristics – vectors containing Renyi divergences between initial measures and their direct multifractal transforms, and the application of the method to image classification. We used three well-known classification models: support vector machine, decision tree and random forest. The classification was performed for some classes of medical images.

The work has the following structure. The next section describes Renyi entropy and direct multifractal transform. In the section 3 we give brief description of the used classification methods. The next section contains the results of experiments performed for the class of images of kidney tissue.

2. MAIN DEFINITIONS

This image comparison method is based on calculation of the Renyi divergence (or α-divergence).

The method consists in obtaining a certain discrete measure for each image, which is calculated for a given partition. The measure of each cell is defined as the sum of pixel intensities. Then the measure is normed that results in obtaining the probability measure distribution. We also consider a finite sequence of direct multifractal transforms of the initial distribution (the number of such transforms is determined empirically). The α-divergence vector is calculated between the resulting sets of measures for two compared images, which we consider as a characteristic of the similarity-difference of image structures

For two given distributions $\boldsymbol{p} = \{\boldsymbol{p_i}\}$ and $\boldsymbol{q} = \{\boldsymbol{q_i}\}$ which characterize two compared images, the Renyi divergences for the variable parameter > 0 , $\boldsymbol{\alpha \neq 1}$ are defined as

$$D_{\propto}(p,q) \;=\; \frac{1}{\alpha - 1} ln \sum\nolimits_{1}^{n} p_i^{\alpha}\, q_i^{1-\alpha} \qquad (1)$$

This value is non-negative, and the divergence is a non-decreasing function of α.

In the particular case when $\boldsymbol{\alpha = 1}$, this transformation is determined by the formula:

$$D_1(p,q) \;=\; \sum\nolimits_{1}^{n} p_i \, ln \frac{p_i}{q_i} \qquad (2)$$

and is called the Kullbak-Leibler divergence.

For a given distribution $\boldsymbol{p} = \{\boldsymbol{p_i}\}$, the direct multifractal transform of the initial distribution is determined by the formula:

$$f_k(p) = \frac{p^k}{\sum_i \, p_i^k} \qquad (3)$$

where k — is a real value.

Direct multifractal transform acts on a set of discrete probability measures corresponding to the images. These transforms form a group, and the set of measures decomposes into disjoint classes of transitivity. Each class contains some initial measure corresponding to the given image, and its subsequent transformations. In fact, the resulting class of measures characterizes the selected image in a certain way.

Experiments show that this method allows us to divide the images into groups according to their actual (expert) classification [1].

3. CLASSIFICATION MODELS

The task of image classification is of the great importance in many subject areas. Usually to solve this problem supervised, unsupervised and deep learning models are considered. We select supervised models because they are easier to measure and verify. In this work 3 classifiers are used: support vector machine (SVM), decision tree and random forest.

SVM is a binary classification algorithm. Among the most large-scale problems that were solved using SVM (and its modified implementations) are the display of advertising banners on sites, the recognition of sex on the basis of photography and the splicing of human DNA.

In classification tasks decision tree model assumes that the predicted result is the class to which the data belongs. The model is simple in understanding and interpretation and allows evaluating the model using statistical tests. This gives us an opportunity to estimate the reliability of the model.

Random forest model is a composition of decision trees. The final result of a random forest classification will be the class for which the majority of the trees voted. We suppose that one tree has one voice. If a model with 500 trees is created for binary classification problem, among which 100 trees point to the zero class, and the remaining 400 point to the first class, the model will predict the first class as a result. This model has high parallelism and scalability.

All implemented models are developed using Java 8 with Apache Spark MLlib algorithms[5].

SVM is configured to use stochastic gradient descent with 500 iterations and different seed values, that optimize model training. L1 an L2 regularization method is used to prevent overfitting of model.

Decision tree has a lot of parameters to configure. In our experiments we use two impurity measures for classification: Gini impurity and entropy. Maximum depth of decision tree is 30.

Random forest also has a lot of parameters and most of them are equal to decision tree model, so we use the same values for them. We configure 200 trees and different seeds for tree generation algorithm.

4. RESULTS OF EXERIMENTS

We performed several experiments using two classes of biomedical images. Images were split by experts to groups according to the information they describe: healthy (14 images) and diseased kidney (15 images). Calculation of divergence is not symmetric operation, so for two images we calculated divergence vectors twice. We calculated Renyi divergence vectors for each pair from the group. For each class of images around 200 feature vectors were obtained. Then one group was marked as 1, and the other as 0.

Renyi divergence was calculated for α={0.25, 0.5, 1, 2} in grayscale palette. Each image was partitioned into cells with size 100x100 pixels for probability distribution calculation. For each cell we calculated measure as the sum of pixels intensity divided by the sum of intensities for whole image. Multifractal transforms were calculated with power from 1 to 10, which means that each divergency vector has the size 10.

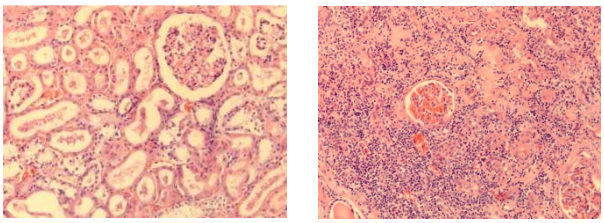

(a) (b)

Fig. 1. Examples of kidney images where (a) is healthy image and (b) with disease

We got 4 groups of vectors and then performed models calculation for each group of vectors according to α values. Then we combined all vectors for healthy kidneys and did the same for kidneys with diseases, and train models over these two big datasets.

Before running dataset (union of positive and negative vectors) over each classifier, dataset was divided in two parts: 70% of dataset was used for training model and 30% for testing of the trained model.

4.1. SVM

Main estimation for SVM classification model is area under ROC-curve. Seed value is used for SGD optimization, so that we could obtain same results on the same dataset.

Seed value / α	0.25	0.5	1	2	All
64	0.5	0.5	0.9	0.84	0.68
97	0.5	0.5	0.88	0.84	0.71
34	0.5	0.5	0.9	0.85	0.71

Table 1. SVM classification results for L1 regularization

Seed value / α	0.25	0.5	1	2	All
52	0.74	0.67	0.81	0.76	0.67
68	0.86	0.85	0.91	0.88	0.71
38	0.84	0.71	0.87	0.84	0.69

Table 2. SVM classification results for L2 regularization

As we can see from results above L2 regularization provides better classification results. Sparsity refers to that only very few entries in a matrix (or vector) is non-zero. L1-norm has produces many coefficients with zero values or very small values with few large coefficients, that can provide worse result.

4.2. Decision tree

Quality of the decision tree model can be measured by the frequency of an error which occurs in classification of model. It is calculated as a number of negative predicted test vectors divided by a total number of test vectors.

α=0.25	α=0.5	α=1	α=2	All
0.2	0.09	0.26	0.27	0.23
0.19	0.10	0.24	0.26	0.23
0.18	0.15	0.29	0.31	0.24

Table 3. Decision tree classification results for Gini impurity

α=0.25	α=0.5	α=1	α=2	All
0.23	0.12	0.18	0.2	0.26
0.19	0.13	0.17	0.21	0.24
0.19	0.07	0.19	0.24	0.24

Table 4. Decision tree classification results for entropy impurity

Classification results can be improved with better α values. In general the both impurity measures provide the same averaged result.

4.3. Random forest

Quality of the random forest model can be estimated by the same way as for decision tree. To improve classification accuracy over a single decision tree, the individual trees in a random forest need to differ. This difference is achieved by introducing randomness in the generation of the trees. The randomness is influenced by the seed, and

what is the most important is that using the same seed should always generate the same result.

Seed value / α	0.25	0.5	1	2	All
54	0.18	0.1	0.22	0.27	0.24
57	0.24	0.08	0.22	0.18	0.23
90	0.17	0.15	0.2	0.25	0.22

Table 5. Random forest classification results for Gini impurity

Seed value / α	0.25	0.5	1	2	All
94	0.19	0.11	0.18	0.22	0.22
61	0.2	0.17	0.21	0.21	0.23
70	0.18	0.09	0.16	0.22	0.22

Table 6. Random forest classification results for entropy impurity

As we can see, decision tree model classification results could be improved with better selection of α values. But in average both measures provide the same averaged result.

5. CONCLUSION

There are a lot of parameters that we can tune in Renyi divergence calculation. We can increase the power of multifractal transform, select α from widely range for specific images and change cell size for probability distribution calculation. Parameters tuning depends on the class of images and is performed empirically.

Experiments showed that SVM model has better results in classification divergence vectors for α={1, 2}. For α={0.25, 0.5} decision tree and random forest have better classification, but for union of all feature vectors obtained for α={0.25, 0.5, 1, 2} random forest has better estimation of classification quality.

Thus, using Renyi divergence provides good results in specified configuration for medical images, and in conjunction with other features may increase classification models output quality.

References

[1] Ampilova N.B., Sergeev V.D., Soloviev I.P. Digital image analysis based on direct multifractal transform. Humanities and Science University Journal 19(2016), c.23-32,http://submit.uni-journal.ru/article/8850

[2] N. Ampilova, I. Soloviev. On Application of Entropy Characteristics to Texture Analysis, WSEAS Transactions on Biology and Biomedicine, ISSN / E-ISSN: 1109-9518 / 2224-2902, Volume 11, 2014, Art. #25, pp. 194-202.

[3] B. Hasselblat, A. Katok. Introduction to the Modern Theory of the Dynamical Systems, M.,Factorial,1999

[4] V. Vstovsky. Elements of information physics, M.,2002.

[5] https://spark.apache.org/docs/latest/ml-guide.html

OBJECT RECOGNITION VIA CCTV BY NEURAL NETWORK USING

Liljana Emilova Docheva, Ivo Nikolaev Dochev, Stoycho Velizarov Manev

Department of Radio ommunications and Video technologies, Faculty of Telecommunications
Technical University of Sofia
8 Kliment Ohridski blvd., 1000 Sofia, Bulgaria

idochev@tu-sofia.bg, docheva@tu-sofia.bg, smanev@tu-sofia.bg

Abstract

One of the major issues in processing large amounts of video information is the detection of certain objects or events that interest us. Monitoring by a human operator the video streaming information does not always lead to good results. This problem can be solved by using neural networks for video recognition.

This paper describes an opportunity for objects recognition by using the neural network and Closed Circuit TeleVision (CCTV) in industry, disasters, household and medicine. A block diagram for images recognizing using a neural network and operation algorithm are proposed. Forest fire detection is performed and the obtained results are presented.

Keywords – CCTV, objects to recognition, neural network

1. INTRODUCTION

The video surveillance systems are very often used in practice. Monitoring by a human operator systems are not as effective as automated systems. Automated systems recognise better very small, unclear or emerging objects.

Neural networks are widely used for object recognition [1], [2]. Their adaptability, noise resistance and efficiency make them preferable in a wide area of applications such as face recognition, digits recognition, object classification, etc.

This paper describes an opportunity for objects recognition by using control system that consist of Closed Circuit TeleVision, neural network and signalling and control device. The system can be used in security, video surveillance, industry, medicine, and more.

2. SYSTEM BLOCK DIAGRAM

Figure 1 shows the system block diagram. The each element choice is important and can affect the performance of the entire system.

The video camera selection is most often done based on its resolution. This parameter specifies the ability to capture tiny details that may have a crucial impact in object recognition. The image high resolution should be kept also when records one, otherwise the camera advantage may be lost. In other words to create a high-quality database, the compression method for image recording is no less important than the resolution of the camera.

The type of neural network, the number of neurons in its layers, and the learning algorithm that is used are important elements in its selection and have a direct impact on the learning quality.

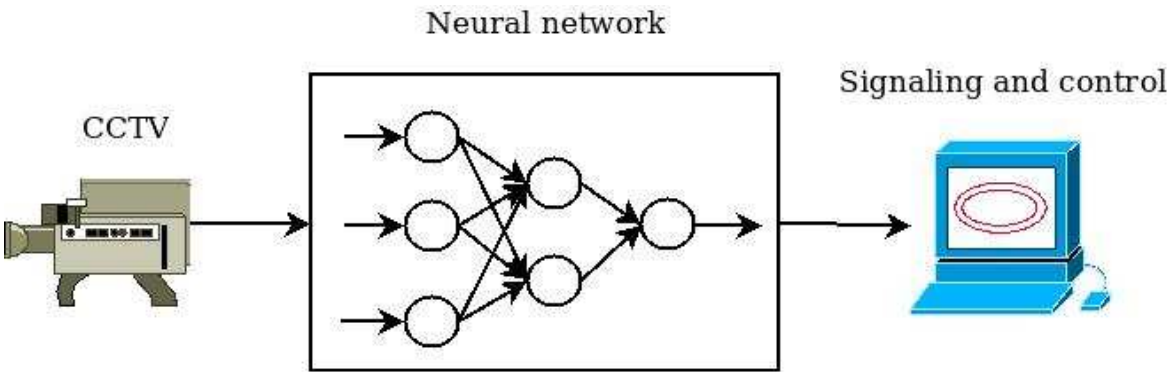

Figure 1. System block diagram

The signalling and control device configuration is last but not least by importance. Its choice have an impact on the timely signalling and the adequate system control.

The algorithm (fig. 2) starts with database creating. The database includes positive (fig. 3) and negatives objects. The two categories are described in separate files. The next step is a vector file creating [3], [4], [5].

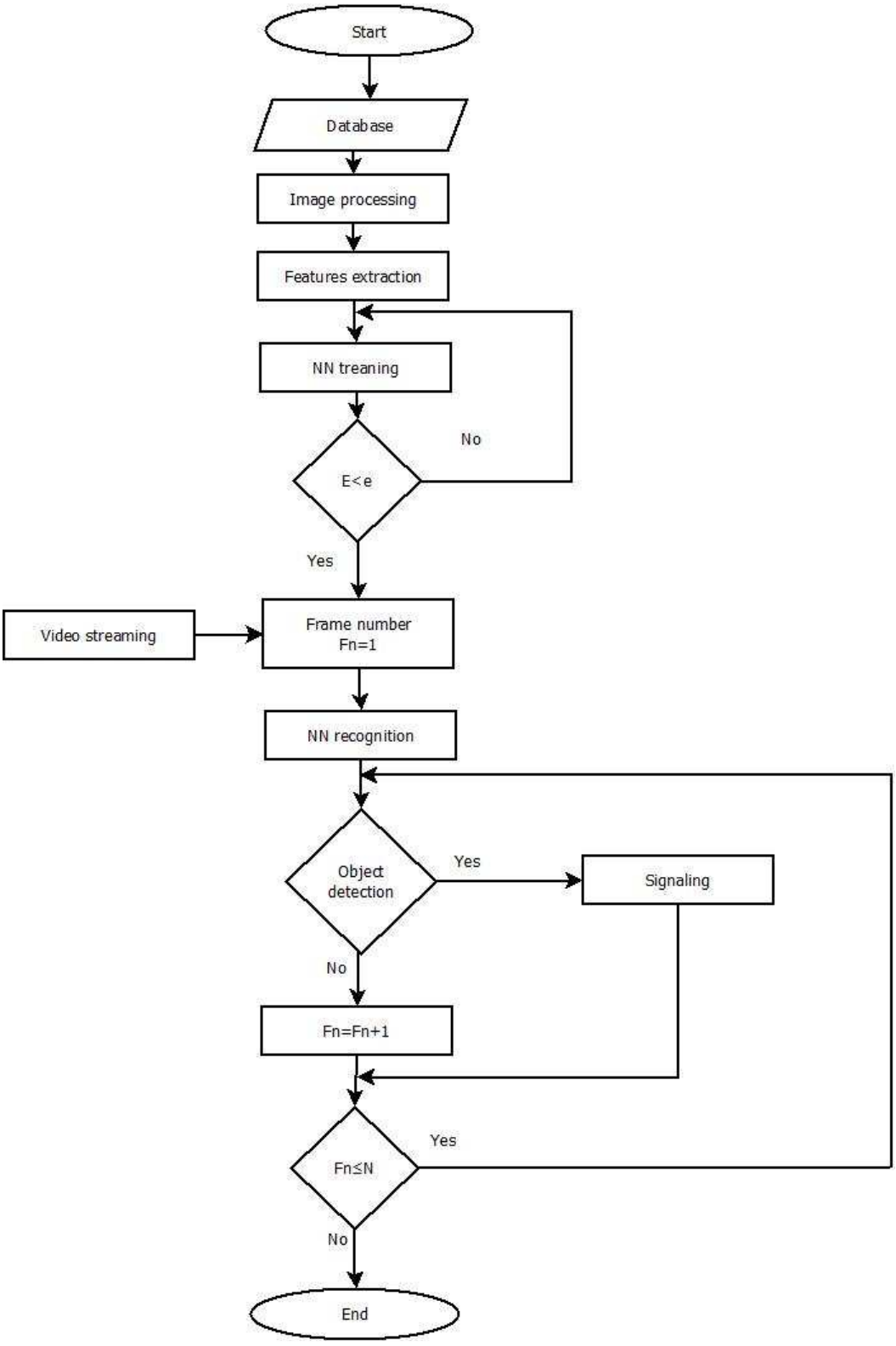

Figure 2. Object recognition algorithm

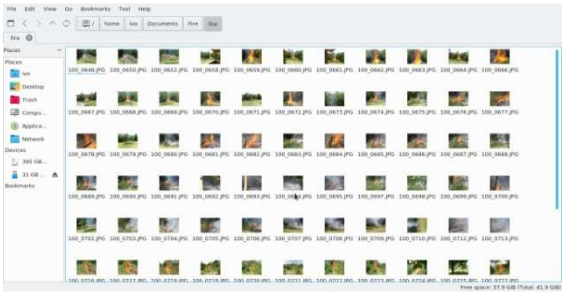

Figure 3. Data base of positive objects

3. OBJECT RECOGNITION ALGORITHM

For some applications preliminary image processing is needed. The most appropriate preliminary image processing is selected experimentally by the lowest neural network learning error.

The extracted image characteristics are passed at the neural network input, then the neural network is trained. The most commonly used criterion for stop neural network training is the least square error. The training of the neural network continues until the error value e is not reached.

Once the neural network is trained, the recognition phase follows. The captured film is fed to the neural network. By means of the **Fn** constant the frames are fed one by one on the neural network. Each frame is checked for the presence of the object that is searched. When the object is detected, the system for signalling and control is activated. After this recognition process continues with the next frames. When the last frame **N** is reached recognition process stops.

On figure 4 and figure 5 are shown a correct recognized object and few false recognized objects. It can be seen that false object recognition occurs in areas of sharp change in brightness. The number of false recognized objects decreases with data base increasing. Not only the number is important, but also the type of the samples. They have to be chosen so that to train the neural network of all possible variants of the object. The choice of the samples in the negative database is also important too. Some of them should contain details of the surrounding environment of the positive ones. The right choice of the system components, the proper database selection, and the correct implementation of the neural network training algorithm ensure object recognition without false recognized objects (fig. 6).

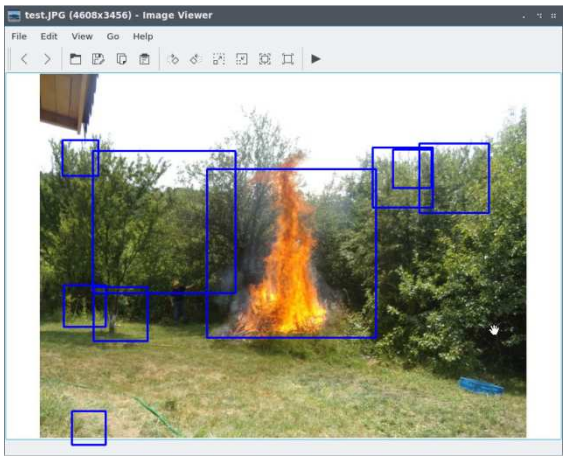

Figure 4. Fire recognition with a correct recognized object and few false recognized objects

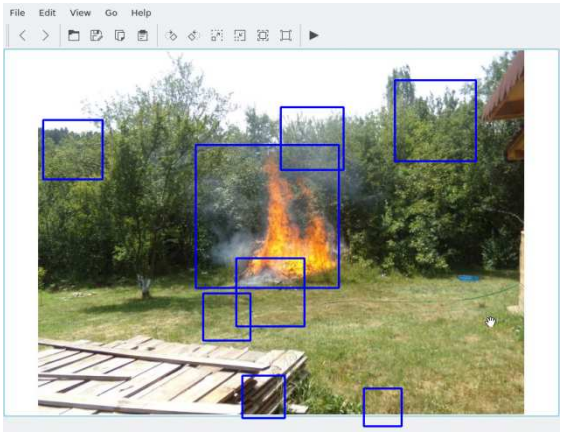

Figure 5. Fire recognition with a correct recognized object and few false recognized objects

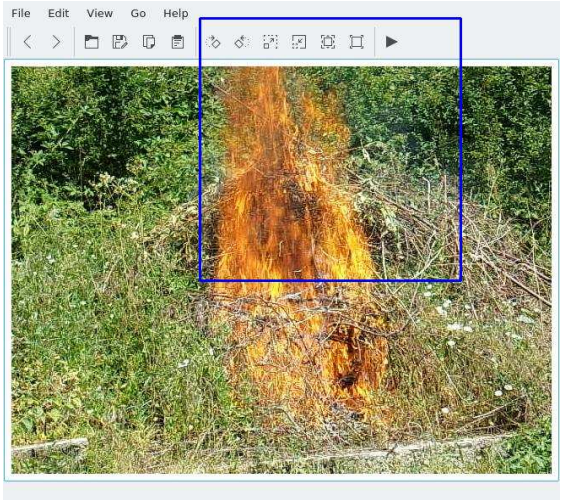

Figure 6. Fire recognition without false recognized objects

4. CONCLUSION

A control system using objects recognition is describe in this paper. It consist of Closed Circuit TeleVision, neural network and signalling and con-

trol device. A block diagram of the system and operation algorithm are proposed. The requirements of the system components choice, the database selection, and the neural network training algorithm are considered.

This system can be used in wide area of application: security, video surveillance, industry, medicine, and more.

References

[1] *C. Bishop, Neural Networks for Pattern Recognition, Oxsford university press, New York, 2005.*

[2] *O. Omidvar J. Dayhoff, Neural Networks and Pattern Recognition, Academic Press, 1997.*

[3] *Training a better Haar and LBP cascade based Eye Detector using OpenCV https://www.learnopencv.com/training-better-haar-lbp-cascade-eye-detector-opencv/*

[4] *OpenCV - Cascade Classifier Training https://docs.opencv.org/3.3.0/dc/d88/tutorial_traincascade.html*

[5] *(Open Source Computer Vision Library – Homepage: https://opencv.org/*

DEVELOPMENT OF AUDIO-VISUAL MODEL AND ALGORITHM FOR HUMAN CONTROL OF MOBILE ROBOT MOTION WITH COMBINED RECOGNITION OF VOICE AND GESTURE COMMANDS

Snezhana Pleshkova, Zahari Zahariev, Aleksander Bekiarski, Shima Senati Dehkharghani

Technical University of Sofia, Bulgaria, St. Kliment Ohridski 8

Tel.: +359 965 3300; E-mail: snegpl@tu-sofia.bg

Abstract

The existence of audio and visual sensors in the intelligent robots, is the real challenge to develop audiovisual models and algorithms for human control of mobile robot motion with recognition of voice and gesture commands. There are a lot of developments in this area of researches. Usually they consider separately only audio or only visual information from human voice or gesture commands to control mobile robots motion, but the precision is not sufficient. Therefore, the goal of the article is to extend this precision applying together the recognized voice and gesture commands with the proposed model and algorithm for human mobile robots motion control. The results for achieved precision in the mobile robots motion control, using together the recognized human voice and gesture commands, are presented and demonstrated from carried out a lot of experiments.

1. INTRODUCTION

There exists two types of interactions between mobile robot and human. They can be considering separately or in combinations:

- mobile robot follow human movement, voice or gestures [1];
- human commands send to control mobile robot motion [2, 3].

This paper considering the second type of interactions between mobile robot and human. This task can be solved using different methods, but in all of them is necessary to take in account the existing and mounted sensors [4] on the mobile robot platform like tactile, ultrasound, GPS, sound, image, wheel sensors, etc. Only the sound and image sensors are useful in the special cases of human mobile robot interactions and there are a lot of developments in this area of researches [5]. Most of them consider separately only audio or only visual information from human voice [6] or gesture commands [7] to control mobile robots motion, but the precision is not sufficient. In this article the goal is to increase this precision applying and analysing together the recognized audio and visual information in human voice and gesture commands. To do this it is proposed a suitable model and corresponding algorithm for mobile robots motion control. The experiments, to test the proposed model and algorithm, are carried out using the mounted on for mobile robot, the embedded IoT module myRIO [8] and with connected to it sound and image sensors, i.e. microphone and camera. The programmer code for realizing the proposed model and algorithm is developed using visual programming language LabView [9], which is compatible and can be embedded in myRIO module.

The achieved precision in the experiments of human mobile robots motion control is presented using together both the recognized human voice and gesture commands and is compared with the precision achieved in the cases of using separately only voice of only gesture commands for mobile robot motion control.

2. THE PROPOSED AUDIO-VISUAL MODEL FOR HUMAN CONTROL OF MOBILE ROBOT MOTION

The general view of the proposed audio-visual model for human control of mobile robot motion with combined recognition of voice and gesture commands is presented on Figure 1. Audio-visual information for voice and gestures commands is received from Microphone and Camera mounted on the Mobile Robot Platform.

The main parts in the proposed audio-visual model are the Voice and Gesture Command Recognition blocks.

The recognized voice and gesture commands are transformed in the next Voice and Gesture Commands Combined Interpretation block as corresponding motor control signals. Then, from these signals, the next Mobile Robot Motor Control block

prepare the necessary execution signals from each of the motors on the wheels of the Mobile Robot Moving Platform, shown on Figure 1.

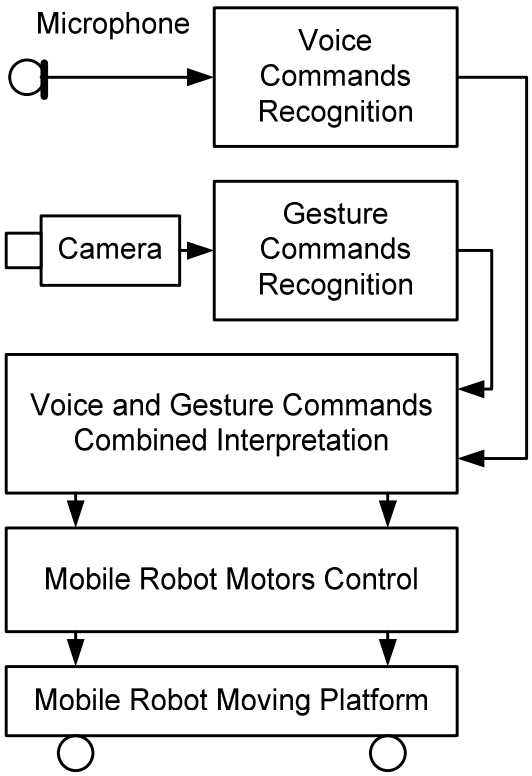

Figure 1. General audio-visual model for human control of mobile robot motion

3. DEVELOPMENT OF ALGORITHM FOR AUDIO-VISUAL HUMAN CONTROL OF MOBILE ROBOT MOTION

The developed algorithm for audio-visual human control of mobile robot motion is presented as audio (Figure 2), video (Figure 3) parts and its combination (Figure 4). Usually the voice only recognition part of algorithm, shown on Figure 2, is started first, because the voice human interaction with mobile robot is more natural and more common used.

After definition of initial or current mobile robot position is necessary to check the voice existence for activate the voice recognition. When the voice command recognition is correct, mobile robot do movement, according to recognized voice command.

If the recognition of voice command is not correct, mobile robot do not movement, increasing the collected number of voice error by one. In this case the algorithm can go to wait for new voice command or, depending to human decision, go to try the algorithm for recognition of the same not recognized voice command, but as a gesture command.

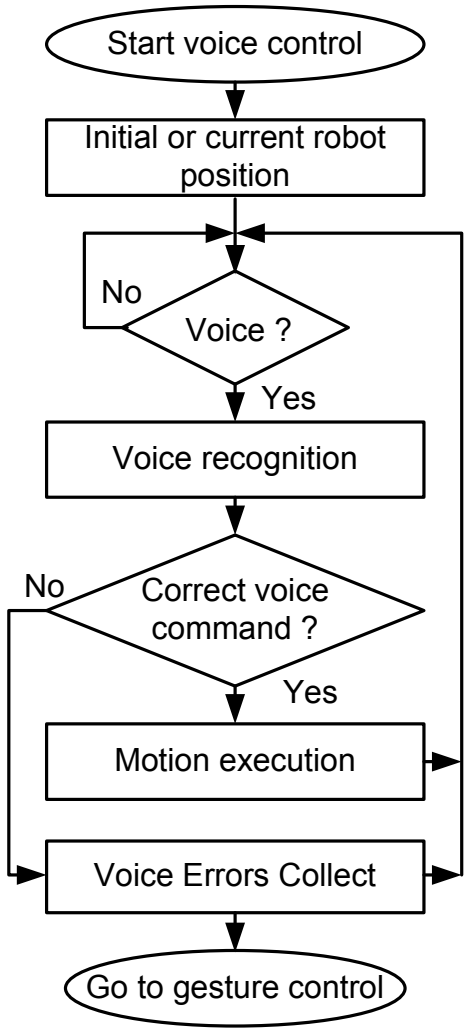

Figure 2. Algorithm for voice only human control of mobile robot motion

The algorithm for gesture only commands recognition (Figure 3) is similar, except that in the case, when the recognition of gesture command is not correct, the algorithm can go to wait for new gesture command or, depending to human decision, go to try the algorithm for combined voice and gesture human control of mobile robot motion.

The algorithm for combined voice and gesture human control of mobile robot motion is presented on Figure 4. In this algorithm are carried out at the same time the voice and gesture commands recognition and if some of them is not correct recognized, then it can go to wait for new not recognized, but as the opposite, gesture or voice command.

Also, if the voice and gesture commands are correctly recognized, they are checked for matching. If the matching fail, then the collected number of combined voice and gesture error is increased by one, mobile robot do not movement and algorithm go to wait for other voice or/and gesture com-

mands. In the case, when the matching of the voice and gesture commands is successful, then mobile robot do movement, according to the recognized voice and gesture commands or the algorithm is ending, if there is a recognized voice and gesture stop commands, or if it is the time to stop motion of mobile robot, depending to human decision.

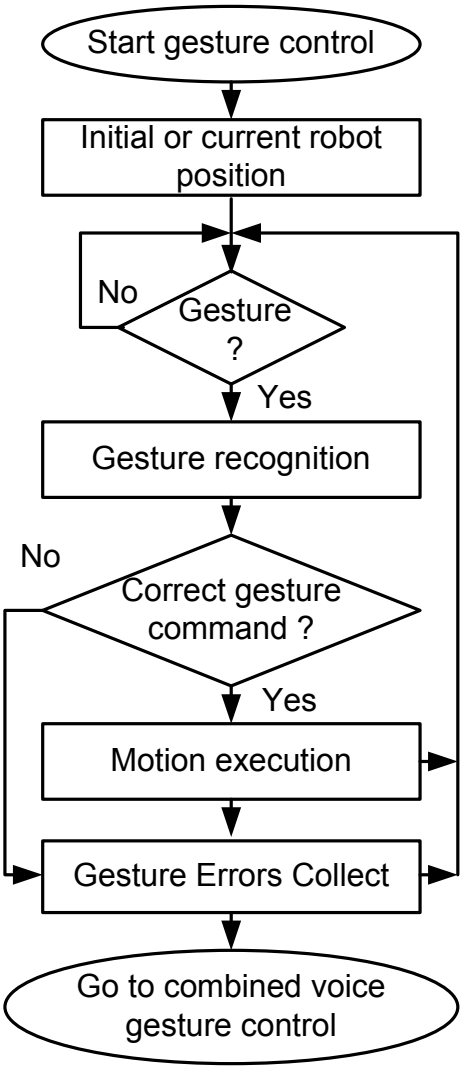

Figure 3. Algorithm for gesture only human control of mobile robot motion

4. EXPERIMENTAL RESULTS

In the experiments are defined different, but with the constant number N_S of moving steps (for example N_S=*60*), tasks for mobile robot to follow the predefined trajectories of motion. The number of collected and averaged errors for voice only EN_V, gesture only EN_G and combined voice and gesture EN_{VG} commands are shown on Table 1. In accordance with the collected errors, in Table 1 are presented also the determined in percentage average precision of human mobile robots motion control using only voice recognized, or only gesture recognized commands, or together recognized voice and gesture commands.

Table 1. Determined average numbers of error and precision

Tests	Errors	Precision,%
Voice only	EN_V =*12*	82
Gesture only	EN_G =*16*	78
Combined voice and gesture	EN_{VG} =*9*	93

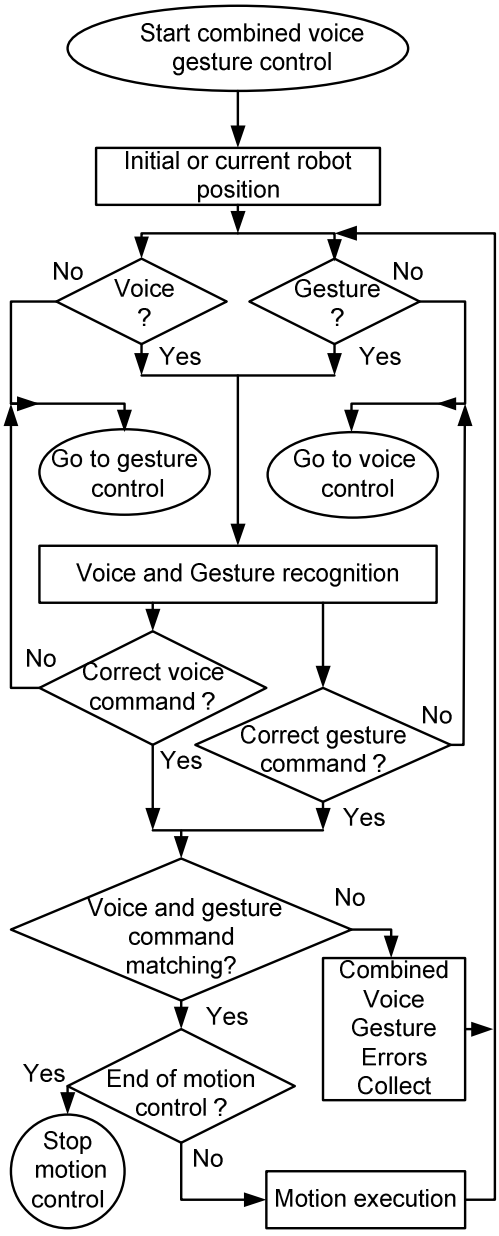

Figure 4. Algorithm for combined voice and gesture human control of mobile robot motion

5. CONCLUSION

As the conclusion the results, summarized in Table 1, can be are analysed in the following comparative way:

- there exists relationship between the collected and averaged recognition errors and the precision of human mobile robots motion control;
- the precision of human mobile robot motion control with voice only commands recognition is greater than the precision of the control with gesture only commands recognition, may be because the gesture recognition is more difficult to realize and is the source of more erroneous recognitions of gestures;
- the precision of human mobile robot motion control with combined voice and gesture commands recognition is superior than the precision of both voice only and gesture only commands recognition.

References

[1] *N. Bellotto, and H. Hu, "Multisensor-Based Human Detection and Tracking for Mobile Service Robots", IEEE Transactions on Systems, Man, and Cybernetics - Part b: Cybernetics, Vol. 39, no. 1, February 2009, pp. 167-181.*

[2] *M. Kim, J. Lee, and S. Kang, "A Self-Organizing Interaction and Synchronization Method between a Wearable Device and Mobile Robot",* Sensors *2016,* 16*(6), 842, pp. 1-15.*

[3] *Sn. Pleshkova, Al. Bekiarski, Sh. Sehati, and K. Peeva, "Perception of Audio Visual Information for Mobile Robot Motion Control Systems", Chapter 6 from the Book Perception of Audio Visual Information for Mobile Robot Motion Control Systems, Springer, June 2014.*

[4] *L. Pérez, Ín. Rodríguez, N. Rodríguez, R. Usamentiaga, and D. García, "Robot Guidance Using Machine Vision Techniques in Industrial Environments: A Comparative Review", Sensors, 2016, Volume 16, 335, pp.1-16.*

[5] *K. Kosuge, "Human-Robot Interaction", IEEE International Conference on Robotics and Biomimetics, Shenyang, China, 22-26 August 2004.*

[6] *R. Jain, and S. Saxena, "Voice Automated Mobile Robot", International Journal of Computer Applications, Volume 16– No.2, February 2011, pp.32-35.*

[7] *K. Cekova, N. Koceska, and S. Koceski, "Gesture Control of a Mobile Robot using Kinect Sensor", International Conference on Applied Internet and Information Technologies, 2016, pp. 251-258.*

[8] *Embedded Device myRIO. National Instruments. http://www.ni.com/en-rs/support/model.myrio-1900.html*

[9] *LabView. National Instruments. http://www.ni.com/en-rs/shop/labview/labview-details.html*

A COMPARATIVE ANALYSIS OF THERMOPILE SENSORS FOR BIOMEDICAL APPLICATIONS

Kalin Dimitrov, Lyubomir Laskov

Technical University of Sofia, Faculty of Telecommunications,
Department of Radiocommunications and Videotechnologies
8 Kliment Ohridski Blvd., 1000, Sofia, Bulgaria

Tel.:+35929653145; Fax:+35929653095;
E-mail: kld@tu-sofia.bg, llaskov@tu-sofia.bg

Abstract

This paper presents a comparative analysis which integrates the field of view (FOV) characteristics of several sensors currently popular on the market. We use thermopile-type thermal sensors which detect the infrared radiations from the human body and then convert them to signal. In order for the temperature to be calculated correctly, in-depth knowledge of the sensor characteristics is necessary. This allows the creation of suitable systems for various biomedical applications such as diseases detection, controlling of physiotherapy processes, etc.

1. INTRODUCTION

Measurement of temperature has been of interest to mankind since antiquity. The beginning of modern understanding of temperature measurement is considered the end of the 16th century. Then Galileo, the first temperature-measuring device, was created based on the idea of expanding and shrinking gases. An important step in the development of temperature measurement methods is the introduction of the first temperature scale by Fahrenheit in the early 18th century. In the middle of the 18th century, Celsius offers a decimal temperature scale. In the early 19th century, Lord Kelvin offers a universal absolute thermodynamic temperature scale that has become the standard in today's temperature measurement [1].

The reasons for the tremendous interest in measuring temperature develop in several major lines.

To ensure high-performance industry, one of the measured quantities characterizing the processes and condition of the equipment is the temperature. This is an important feature of almost every production process that determines the variety of methods and tools used [2].

One of the most important factors for determining a person's health is their body temperature [3-6]. Body temperature is a magnitude characteristic of the degree of heat that is determined by the internal kinetic energy of the thermal movement of the molecules. Therefore, temperature can be regarded as a conditional statistical magnitude, proportional to the average kinetic energy of body molecules [3].

Therefore, it is extremely important to know what the measured temperature depends on, in what limits it varies. Of course, the methods of measurement are varied. In order to accurately measure temperature in a particular setting, it is necessary to properly build its corresponding measurement system, taking into account all (as far as possible) influencing factors.

This paper examines a small part of the temperature measurement techniques used in diagnostic and therapeutic systems [7-10].

The use of non-contact sensors also increases due to the ban on the use of mercury thermometers in the countries of the European Union.

2. THEORETICAL BACKGROUND

It is well known that the temperature measurement methods are divided into two basic groups: contact and non-contact. In contact methods, the exchange of energy between the medium and the thermometer is based on thermal conductivity, and on non-contact – heat radiation.

There are three basic physical principles used in temperature measurements [1]:

I. Determination of the temperature by measuring some of the physical characteristics depending on it; 2. By measuring some temperature-dependent

physical characteristics of thermometric bodies placed in the environment and receiving their temperature by heat exchange; 3. Measurement of heat radiation of heated bodies. This method is used to measure the temperature of the different surfaces.

Here we will mainly concentrate on the third method [8-10]. Clearly, the final results should be comparable and usable with previous research by other authors. That is why we will use the international temperature scale (ITS). It is a practical realization of the theoretical thermodynamic scale adopted in the middle of the 20th century with the most accurate approximation. The thermodynamic scale starts from absolute zero. It coincides with the scale of a gas thermometer filled with ideal gas that is calibrated at the triple point of the water [1].

ITS has undergone several adjustments and uses multiple reference points that are reproducible with high enough accuracy.

The interpolation between the reference points of the temperature scale is calculated on the basis of formulas illustrating the ratio of temperature to standard thermometer readings. Various thermometers are used in different areas of the temperature scale.

The practical application of the thermopile for non-contact temperature measurement is increased. This is an electronic device that converts thermal energy into electrical energy. It is composed of several thermocouples connected usually in series or, less commonly, in parallel [2, 9, 11-13].

Ideally the output from the thermocouple pair will be a voltage that is directly proportional to the temperature difference across the thermal resistance layer and also to the heat flux through the thermal resistance layer. Adding more thermocouple pairs in series and making a thermopile increases the magnitude of the voltage output. The output of a thermopile is usually in the range of tens or hundreds of millivolts [9].

3. GENERAL SET-UP

We will take a look at the basic ideas for using thermopile sensors for biomedical purposes. Naturally, we start with the idea of static observation of the object.

It is important to note that we will assume that we are considering the simplest form of energy transfer between the object and the sensor. That is, the energy spreads in the so-called viewing angle. This approximation is possible due to the relatively small distances between the object and the sensor. They are in the order of centimeters.

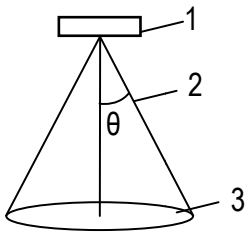

Figure 1. General set-up for observation (1-sensor, 2-FOV, 3-sensed area)

For this reason, we do not use additional optical elements and we do not calculate MTF [14].

However, we note that in the viewing angle the distribution is not uniform. This distribution is given by many manufacturers in the relevant company documentation. Here we will look at data from four such sensors.

In the following figures (Fig.2 – a,b,c,d), we present the dependence of the normalized voltage received by the sensor on the angle of the four different sensors available on the market at the moment. We use sensors as follows – a-TP339, b-TS318, c-TMP007, d-MLX90616 [15-18].

In order to effectively use these catalog data, we have processed them as a set of discrete numerical values U(θ).

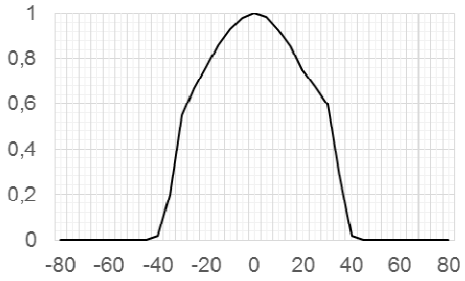

a

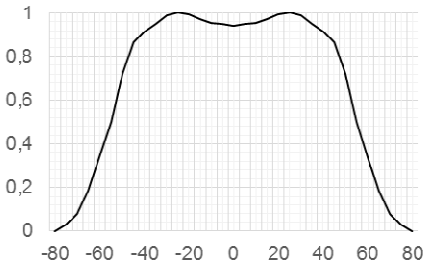

b

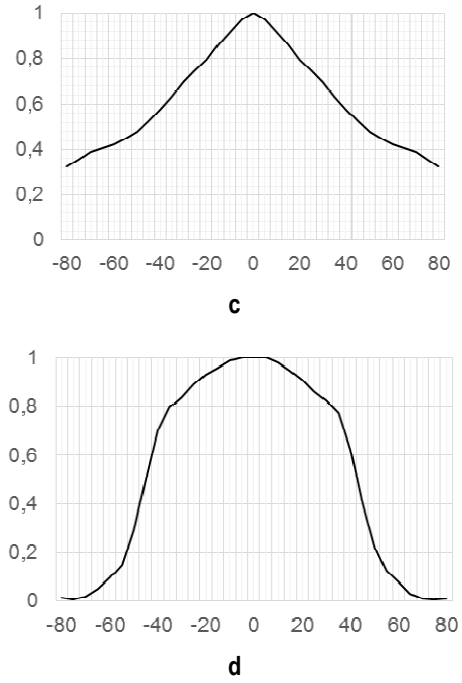

Figure 2. Approximated data for FOV for different sensors, x axis is the angle θ in degrees, and the axis is the normalised output. The sensors are a-TP339, b-TS318, c-TMP007, d-MLX90616

The difference in the viewing angle is essential if we try to receive 2-dimensional results based on the xy sensor movement. Then, in a non-flat object, it is necessary to consider the distance between position 1 and 3 in Fig.1 [19]. Such scenarios can be used with the simultaneous application of physiotherapy and temperature control. Of course, two-dimensional imaging can be used with a multi-point sensor and a suitable optic. In this case we have no possibility to add a second distance correction sensor. The main issues with single sensor systems are lower data acquisition speed (compared to array) and problems of a mechanical nature.

4. NUMERICAL EXPERIMENTS

Again, we will look at the layout of Figure 1. We use the classical approach for deriving solid angle with integration of unit surface element in spherical coordinates [19]

$$\Omega = \int_0^{2\pi} \int_0^{\theta} \sin\theta' \, d\theta' \, d\varphi \, . \qquad (1)$$

After integration we derive

$$\Omega = 2\pi(1 - \cos\theta) \, . \qquad (2)$$

It should be noted that the observed area presented on Fig.1 as pos.3 is relatively small.

We now calculate the normalized integral energy for the four sensors in question. We use the data from the guidelines by integrating (2) numerically for different angles

$$\int_{\theta_1}^{\theta_2} U(\theta) d\theta \qquad (3)$$

As a point of focus, the relationship between integration for the different sensors and an idealized sensor without angular dependence is of interest.

The results are presented graphically in Figures 3-a and 3-b.

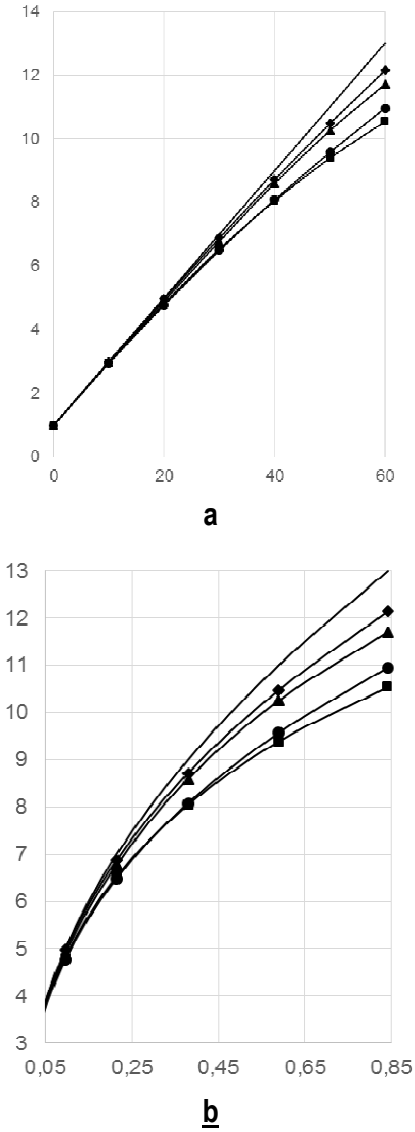

Figure 3. Results from numerical integration, a – x axis is the angle θ in degrees, b – x axis is the solid angle Ω in steradians (lines without marks – ideal sensor; curves with diamond marks – MLX90616; curves with triangle marks – TS318; curves with circle marks – TMP007; curves with square marks – TP339;)

5. CONCLUSION

When measuring body temperature in areas with a shape other than the plane, it makes sense to adjust the data from infrared sensors. Nowadays, this can be achieved relatively cheaply with mechanical scanning and addition of a second distance sensor. The work may have biomedical applications, such as skin temperature control in hand-held laser therapy and more.

6. ACKNOWLEDGMENTS

We would like to thank the Scientific Research Sector of TU-Sofia for the financial support.

References

[1] *T. McGee, Principles and Methods of Temperature Measurement, John Wiley & Sons, 1988*

[2] *H. Steiner, S. Cerimovic, T. Glatzl, F. Kohl, M. Schlauf, T. Schalkhammer, F. Keplinger, T. Sauter, "Flexible Flow Sensors for Air Conditioning Systems Based on Printed Thermopiles", Procedia Engineering, vol. 168, Elsevier, 2016, pp. 830-833*

[3] *Y. Houdas, E.F.J. Ring, Human Body Temperature: Its Measurement and Regulation, Springer Science & Business Media, 2013*

[4] *S. Sruthi and M. Sasikala, "A low cost thermal imaging system for medical diagnostic applications", 2015 International Conference on Smart Technologies and Management for Computing, Communication, Controls, Energy and Materials (ICSTM), 2015, pp. 621-623.*

[5] *R. Ananda Natarajan, Biomedical Instrumentation and Measurements, PHI Learning Pvt. Ltd., 2016*

[6] *G. Zouridakis, Biomedical Technology and Devices, Second Edition, CRC Press, 2014*

[7] *Xiubao Sui∗, Qian Chen, Guohua Gu, Micro-scanning system using flat optics for resolution improvement of infrared images, Optik, vol. 124, Elsevier, 2013, pp. 2292– 2297*

[8] *M. Henini, M. Razeghi. Handbook of Infrared Detection Technologies. Elsevier, 2002*

[9] *A. Rogalski, Infrared Detectors, CRC Press, 2010*

[10] *M. Vollmer, K. Möllmann, Infrared Thermal Imaging: Fundamentals, Research and Applications, John Wiley & Sons, 2011*

[11] *S. Singh, M. Yadav, S. Khandekar, Measurement issues associated with surface mounting of thermopile heat flux sensors, Applied Thermal Engineering, Vol. 114, 5, Elsevier, 2017, pp. 1105-1113*

[12] *S.Thapa, S. Tangutooru, E.Guilbeau, N. Crews, The thermopile: An anisotropic temperature sensor, Sensors and Actuators A: Physical, vol. 187, Elsevier, 2012, pp. 132-140*

[13] *E. Sebastian, C. Armiens, J. Gómez-Elvira, Infrared temperature measurement uncertainty for unchopped thermopile in presence of case thermal gradients, Infrared Physics & Technology, vol. 54, Issue 2, Elsevier, 2011, pp. 75-83*

[14] *H. Budzier, G. Gerlach, Thermal Infrared Sensors: Theory, Optimisation and Practice, John Wiley & Sons, 2011*

[15] *Datasheet for Thermopile Infrared Sensor TP339, http://www.roithner-laser.com/datashe ets/pd/TP339x.pdf, visited 09.2018*

[16] *Datasheet for Thermopile Infrared Sensor TS318-11C55, https://www.te.com/commerce/DocumentDelivery/DDEController?Action=srchrtrv&DocNm=TS318-11C55&DocType=DS&DocLang=English, visited 09.2018*

[17] *Datasheet for Thermopile Infrared Sensor TMP007, https://www.digikey.com/catalog/en/ partgroup/tmp007-infrared-thermopile-sensor-breakout-board/49493, visited 09.2018*

[18] *Datasheet for Thermopile Infrared Sensor MLX90616ESF-HCA, ttps://www.melexis.com/ en/documents/documentation/datasheets/datasheet-mlx90616, visited 09.2018*

[19] *J. R. Mahan, Radiation Heat Transfer: A Statistical Approach, John Wiley & Sons, 2002*

ADVANCED SIGNAL PROCESSING METHODS FOR ANALYSIS OF HIGH DYNAMIC RANGE ACOUSTIC PHENOMENA

T. Trifonov[1,2], I. Simeonov[1], N. Yordanov[1]

[1]Vasil Levski National Military University, Veliko Tarnovo, Bulgaria
76, Bulgaria Blvd., 5000
Tel. +35962 618724, Fax. +359 62 618899,
E-mail: ivanov_ivan@nvu.bg, nkyordanov@nvu.bg

[2]St. Cyril and St. Methodius University of Veliko Tarnovo,
Department of Computer Systems and Technologies, Veliko Tarnovo, Bulgaria
E-mail: tihomirtrifonov55@gmail.com

Abstract

The present work explores a number of modern methods for the processing of acoustic signals with a large dynamic range. As it is known, a number of difficulties arise in recording and analyzing them. Therefore, a specialized platform and a measuring microphone with the required features are used. The actual processing is performed in Matlab environment. Examples of seemingly highly different areas are considered: acoustics on the battlefield, musical acoustics - studying the bell ringing and archaeoacoustics - study of sacred Thracian sites on the territory of the Republic of Bulgaria.

The methods of Fourier analysis and Wavelet analysis were used. For the visualization of the scalograms, a method of transforming them through the conformal method, described in an earlier work by two of the co-authors is proposed.

It should be emphasized, that an analogy has been made in the mathematical description of the acoustic and electromagnetic waves, and that the proposed methods could also be used for the study of electromagnetic tasks in the two-dimensional field.

The results can be used in various areas of acoustics, electrodynamics, image processing in medical diagnostics, systems of detection and localization of terrorists, tactical firing systems on the battlefield, etc.

1. INTRODUCTION

There are a great number of sources of sound (including ultrasound and infrasound). The human hearing is not sensible for ultrasound and infrasound (too less or very high frequencies).

On the other hand the dynamic range of some sound sources exceeds the human hearing harmless limit of 120 dB. For example, a bell ringing and gunfire of machine gun have the similar characteristics in acoustic sense. These characteristics require the use of special measuring and analyzing equipment as well as appropriate microphones.

Combination of the acoustic equipment with special software enables obtaining of visual representation of important characteristics of the sound sources both for military and civil applications [1,5].

For acoustic waves, soft (Dirichlet) or hard (Neumann) boundary conditions are imposed on scattering objects located in a homogeneous non-viscous medium. The absence of viscosity is justified for a fluid (such as air and water) in the linear approximation, [2].

The radiation and diffraction theory of acoustic waves is scalar, and it is simpler than the vector theory of electromagnetic waves. Because of this, we investigate acoustic problems. The obtained results can be used in similar electromagnetic phenomena.

This facilitates the study of electromagnetic problems.

It is known that from a mathematical point of view, all two-dimensional diffraction problems have identical solutions for acoustic and electromagnetic waves, [2,3].

2. SOME WAVE REPRESENTATIONS AND ANALOGIES IN THE HELMHOLTZ EQUATION AND MAXWELL EQUATIONS

In [2] it is shown many analogies between acoustic and electromagnetic wave behavior that simplified electromagnetic vector theory calculations.

In the linear approximation, the velocity potential u of harmonic acoustic waves satisfies the Helmholtz wave equation

$$\nabla^2 u + k^2 u = I \qquad (1)$$

Here $k = \frac{2\pi}{\lambda} = \frac{\omega}{c}$ is the wave number, λ the wavelength, ω the angular frequency, c the speed of sound, and I the source intensity characteristic. The time dependence is assumed to be harmonic $e^{-i\omega t}$.

The following analytic expressions for velocity potential determined acoustic pressure p and the velocity v of fluid particles, caused by sound waves

$$p = -\rho \frac{\partial u}{\partial t},\ \vec{v} = \nabla u \qquad (2)$$

where, ρ - mass density of a fluid.

The power flux density equals

$$\vec{P} = p\vec{v} = p\nabla u \qquad (3)$$

It is the analog of the Poynting vector for electromagnetic waves. Its value averaged over the period of oscillations T equals

$$\vec{P}_{av} = \frac{1}{2}\mathrm{Re}(p^*\vec{v}). \qquad (4)$$

In scattering problems, the quantity u plays the role of electric field intensity $\vec{\mathrm{E}}$ or magnetic field $\vec{\mathrm{H}}$, depending on the polarization of electromagnetic waves intensity. Their power flux density, or the Poynting vector, is defined as

$$\vec{\mathrm{P}} = \vec{\mathrm{E}} \times \vec{\mathrm{H}} = \frac{1}{2}\mathrm{Re}\left(\vec{\mathrm{E}} \times \vec{\mathrm{H}}^*\right).$$

Therefore the acoustic problems can be expressed with scalar Helmholtz equation, as well as Maxwell equations – electromagnetic case. In two-dimensional case the lasts can be written in the form as two independent equations for electric field intensity $\vec{\mathrm{E}}$ and magnetic field $\vec{\mathrm{H}}$ with the following formulas, [3]

$$\nabla^2\vec{\mathrm{E}} + k^2\vec{\mathrm{E}} = 0$$

$$\nabla^2\vec{\mathrm{H}} + k^2\vec{\mathrm{H}} = 0.$$

3. SOME CHARACTERISTICS OF THE SOUND

Below we show three of the most important characteristics: damping of the sound, its spectrum and scalogram. For example it will regard sound record from unique bronze bell from XIII century 1211-1216 year, tower-belfry on the metropolitan church of St. Nicholas, Melnik, [1]. One of situations that illustrate the problems in acoustic propagation scenario is shown in Fig. 1.

Figure 1. Measuring microphone toward XIII century bell disposition.

Here is represented the experimental setup with the two unique bronze bell in the museum hall of the National Historical Museum in Sofia, [6]. It can be seen the position of measuring microphone 4193 Brüel&Kjær, [9] and the distances.

- damping of the sound – the change of the dynamic range is shown on fig. 2,3;
- spectrum – shows the distribution of the frequencies.

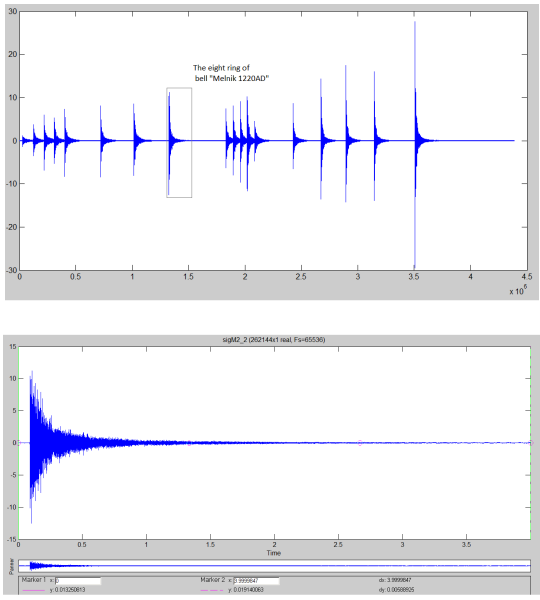

Figure 2. One waveform of Bulgarian bell stroke (XIII cent.), on the second it is separated only one bell ring (the eight), where $\mathbf{F_{samp.}} = \mathbf{2^{16}}$Hz, $\mathbf{N_{samp}} = \mathbf{2^{18}}$

The calculations was produced in MatLab where signal's power spectral density (PSD) was analyzed with the nonparametric method of Discrete Fourier Transform by Fast Fourier Transform algorithm (FFT).

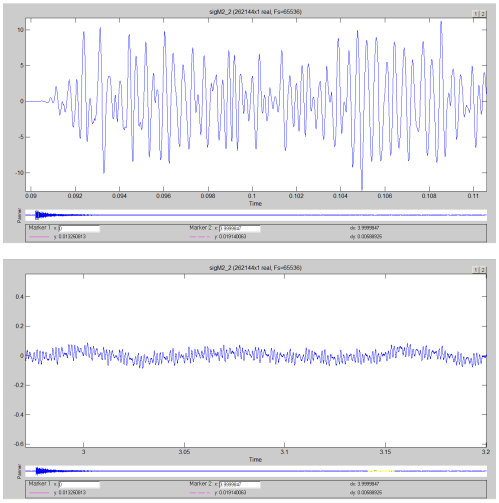

Figure 3. The front and the tail of signal from one bell ring, the eight one fig. 2.

For above example it can be note that the bell is a complicated sound source with a very wide frequency range and a unique dynamic range of the transmitted signal. Its spectrum consist many partials. The biggest spectral components are seen in Table 1.

Table 1. The biggest spectral components of the bell "Melnik 1220AD"

Number	Frequency, (Hz)	Magnitude, (dB)
1	635,6Hz	-25,59
2	755,3	-21,67
3	981,4	-22,27
4	1374,8	-23,46
5	1813,6Hz	-23,68
6	1841,5Hz	-24,03
7	2306,5Hz	-25,41
8	2479,2Hz	-26,13

– scalogram – continuous wavelet transform (CWT).

Starting with Haar's functions and today Daubechies and other families of wavelets [4] this time-scale analysis become very useful tool in advanced digital signal processing.

More precisely, suppose that $a \in \mathbb{R}^+, b \in \mathbb{R}$, or (a, b) determine one point in right-half plane, then the continuous wavelet transform (CWT) of a continuous, square-integrable function is expressed by:

$$\mathrm{CWT_f}(a,b) = \langle \mathrm{f(t)}, \psi_{a,b}\, \mathrm{f(t)} \rangle = \frac{1}{\sqrt{a}} \int_{-\infty}^{\infty} \mathrm{f(t)} \psi^* \left(\frac{\mathrm{t}-b}{a} \right) \mathrm{dt}, \quad (5)$$

where $\langle , \rangle$ denotes the inner product.

The wavelet transform of a one-dimensional signal is a two-dimensional time-scale joint representation, [7].

We turn our attention to the scalograms. Especially, to change their rectangular shape to another one - this will be more convenient for further investigations, see [5]. If we make known conformal mapping, the rectangular graph will be transformed to a circular graph.

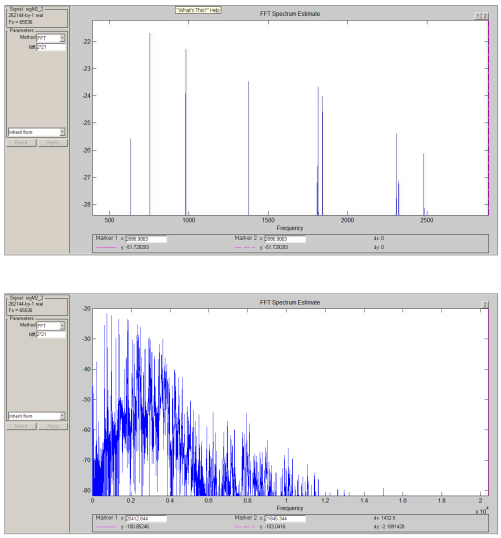

Figure 4. The log magnitude spectra of signal the Bulgarian bell ring, f=1,...,2500Hz and f=1,...,20000Hz.

4. EXAMPLES OF EXPERIMENTS AND SCALOGRAM TRANSFORMATIONS

The battlefield is a disorienting place and it is very hard to identify where enemy is located. Acoustic sensors are very convenient in this situation.

The data from the training range, collected during the tactical exercises, were exported from PULSE platform as mat files (or ASCII files), to be processed in MATLAB®. The signals, captured from the microphone, are analyzed in time-frequency domain and time-scale domain [5,6].

In figure 5 we show example for two 14.5mm-caliber KPVT waveforms, where KPVT is an abbreviation for "Krupnokaliberniy Pulemyot Vladimirova Tankoviy" Russian, i.e. large-caliber tank machine gun.

Figure 5 shows a typical acoustic signal waveform of KPVT machine gun shots, recorded from the exercise area and exported to MatLab. The corresponding calculated scalograms, or CWT, are illus-

trated on Figure 6, where scale parameter a = 1,...,64. The scalograms, transformed into circular ring (sound print) are shown on Figure 7.

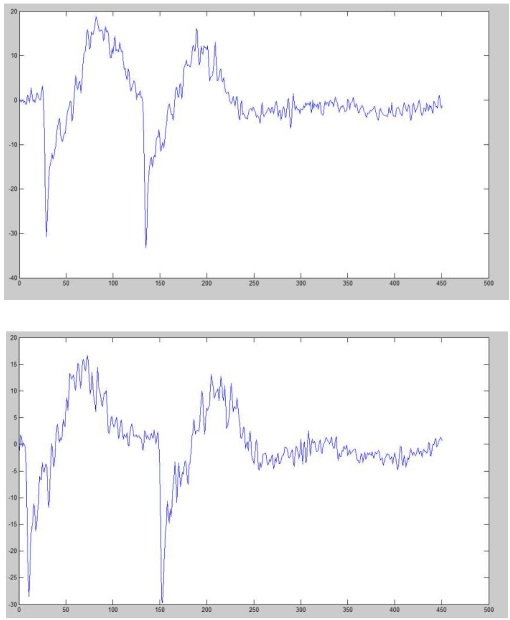

Figure 5. Waveforms from large-caliber tank machine-gun, 14,5 mm KPVT

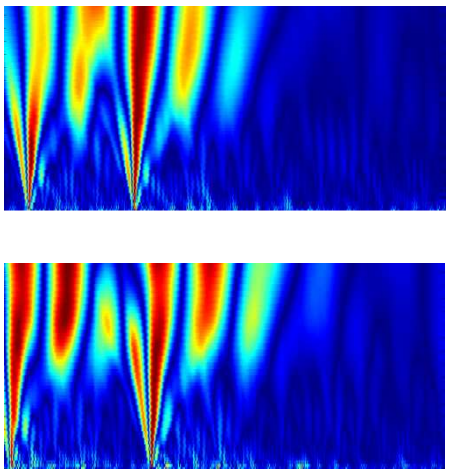

Figure 6. Calculated scalograms for 14,5 mm KPVT waveforms correspondingly to fig. 5., a=1,...,64, Daubechies db3.

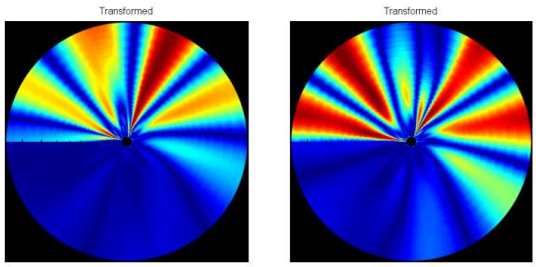

Figure 7. Calculated scalogram transformations (sound prints) for 14,5 mm KPVT correspondingly to fig. 5 and 6, a=1,...,64, Daubechies db3.

Figure 8 shows an experiment in the chamber of the Thracian tomb in Sveshtari, where the world-famous Bulgarian musician Theodosii Spassov participated. Figure 9 shows the spectral components. Preliminary analyzes of the acoustic studies of this and other sacred Thracian sites show that despite the small volume of the rooms, they have very good parameters in the reproduction of low frequencies (in the range of 100 and below 100 Hz). According to some scientists who works on project "Thracians - genesis and development of ethnicity, cultural identities, interactions and civilizational heritage of antiquity", [8] this is due to the fact that rituals have been performed in these rooms exclusively by men whose voices are known to be located in the low-frequency sound range. The interpretation and analysis of raw data is continued.

Figure 8. Record of kaval- ancient Bulgarian flute "in situ" in Thracian Tomb near the village of Sveshtari (Ginina mound).

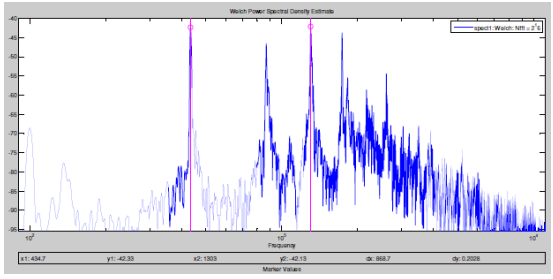

Figure 9. Spectral components of the flute in current time

5. CONCLUSION-FUTURE RESEARCH

It should be noted that the methods, used for analyzing and presenting acoustic results can very easily be adapted to analyze electromagnetic tasks.

As highlighted above, in the two-dimensional area the mathematical description of acoustic and electromagnetic wave is practically analogous (of course, taking into account the polarization of electromagnetic phenomena and boundary conditions).

In the end, it is worth to remark that the scalogram conformal mapping gives better visualization of the special features of the acoustic signal. The conformal transform gives adaptation to the different scales and sound prints of different sound sources could be collected to create records in database which will facilitate the recognition of the unknown records.

References

[1] *The Bell Project-Research and Identification of Valuable Bells of the Historic and Culture Heritage of Bulgaria and Development of Audio and Video Archive with Advanced Technologies, http://www.math.bas.bg/bells/belleng.html*

[2] *Pyotr Ya. Ufimtsev Fundamentals of the Physical Theory of Diffraction, 2nd Edition, , Wiley-IEEE Press, May 2014*

[3] *Shenderov, E.L, Volnovie zadachi gidroakustiki (Wave Problems of Hydroacoustics), Leningrad: Sudostroenie, 1972.*

[4] *Daubechies, Ingrid, Ten Lectures on Wavelets (CBMS-NSF regional conference series in applied mathematics; 61), SIAM 1992.*

[5] *Dimkov G., T. Trifonov, I. Simeonov "Improving the Visualization of Scalograms by Means of Transformation in the Complex Plane", Proc. of the Forty Second Spring Conference, of the Union of Bulgarian Mathematicians, Borovetz, April 2–6, 2013, p.218. online at address http://www.math.bas.bg/smb/2013_PK/tom_2013/pdf/218-221.pdf.*

[6] *Trifonov T., I. Simeonov, R. Dzhakov Features of Time-Frequency Analysis Visualization of Large Dynamic Range Signals, XLVII International Scientific Conference on Information, Communication and Energy Systems and Technologies (ICEST 2012), Veliko Tarnovo, June 2012, pp. 155-158, online at address: http://www.icestconf.org/wp-content/uploads/2016/proceedings/ icest_2012_02.pdf.*

[7] *Alexander D. Poularikas, The Transforms and Applications Handbook, Second Edition, CRC Press, 1999*

[8] *Fol, V., György, G., Trifonov, T., Alexiev, A., Ivanov I.S., Acoustic Characteristics of Sacral Thracian Sites. AIS 2016 - 11th International Symposium on Applied Informatics and Related Areas, November 17, 2016, Székesfehérvár, Hungary, 84-87.*

[9] *Brüel&Kjær, www.bksv.com.*

QOS-ENABLED MQTT IMPACT ON RESILIENT COMMUNICATION IN INTERNET OF THINGS SYSTEMS

Paulina Kuojaite[1], Rasa Bruzgiene[1], Lina Narbutaite[2], Tomas Adomkus[3]

[1]Faculty of Electrical and Electronics Engineering, Department of Electronics Engineering
[2]Faculty of Informatics, Department of Software Engineering
[3]Faculty of Informatics, Department of Computer Sciences

[1,2,3]Kaunas University of Technology
Studentu str. 50-452, Kaunas, Lithuania, LT- 51368
E-mail: rasa.bruzgiene@ktu.lt

Abstract

Autonomous systems and networks, together with ongoing communication between devices in it, are becoming an integral part of the current industry. The development of networks and systems is based on the innovative solutions that allow efficient processing of data from end-points at any place and reliable transmission of it to any device in the world connected to the Internet. And Internet of Things (IoT) plays a key role in this, as it allows to create a communication environment, in which various technologies, devices and sensors, can communicate with one another. However, this is very complicated and challenging to guarantee that different systems will properly communicate with each other and the interoperability between different areas will be achieved. Moreover, the use of Internet of Things doesn't guarantee, that environmental sustainability, flexibility, efficiency, reliability and resilience in all industry areas will be ensured. One of the reasons for this is the connectivity in Internet of Things systems. Due to that, this paper will focus on the use of lightweight communication protocol - Message Queue Telemetry Transport (MQTT) – in various Internet of Things systems with the goal of characterizing the data delivery process in focus of it's behavior by different MQTT Quality of Service (QoS) levels and impact to the resilience of communication in wireless networks. An approach for modeling the Internet of Things systems and MQTT-based publish/subscribe communication environment will be presented in this paper, as well as the investigations of data delivery process and it impact to the overall stability of the system performance.

1. INTRODUCTION

Every year, the number of devices connected to the Internet grows at a high rate, so the Internet of Things is expanding rapidly around the world [1]. At a present, the server/client architecture is mostly used for connection and communication between various IoT nodes on the network [2]. However, the rapidly growing number of IoT nodes becomes a challenge in current IoT systems, where millions of different devices are involved. Even more, when the number of devices will exceed the billions, the centralization in the communication way will turn into a bottleneck [3]. In this case, the decentralized communication with a possibility to have a broker between the communication parts becomes more sufficient solution in large scale Internet of Things systems. The insertion of the broker into the IoT architecture and the change of all communication process breaks all end-to-end communication principles and changes the networking in Internet of Things systems. Message Queue Telemetry Transport (MQTT) protocol allows to create an architecture with a publish-subscribe communication method based on the TCP/IP protocol [4]. MQTT protocol has a high efficiency of a bandwidth, thus helps to reduce the resources of IoT equipment on the network. Data receivers can easily understand the data they receive, even without knowing who was the sender in such MQTT-based publish-subscribe architecture. The reason for this is the topic of data, subscribed by the receivers. In this case, the whole control of data transmission process goes to the hands of data receivers. In contrast to it, the sender has one-sided control of data transmission in the traditional server/ client architecture of the network. As already mentioned, since the MQTT protocol is based on topics, each client, who publishes the data to the MQTT broker must include a topic in the message that becomes the information for a data route from broker's side (Fig. 1).

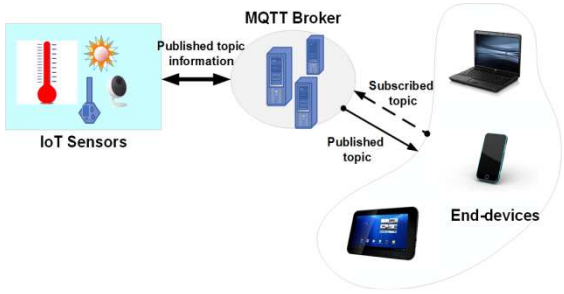

Figure 1. MQTT publish-subscribe architecture in IoT

MQTT broker is the main communication node of the network in charge of sending messages between sender and receiver. A client, who wants to receive data, must subscribe to the relevant topic, so that the broker can send a data from client-publisher to the client-subscriber. For this reason, clients do not need to know each other, because they only interact on topics. If a publisher publishes a data on topic "*something*", the data will be delivered to all subscribers, which requested such data with the topic "*something*". Moreover, MQTT-based publish-subscribe communication way in the network can help in discarding the unsolicited or illegal network traffic such as SPAM (undesired electronic messages) or denial of service (DoS) attacks, because receiver is the main, who decides what type of data to get from the sender.

However, the use of broker and subscribe/publish communication model has also problematic issues related with the guarantee of a reliable and stable data delivery process in Internet of Things systems. The key (and still open) question is how to provide a resilient communication and ensure end-to-end reliability in IoT-based network, where the end nodes are separated and end-to-end communication is impossible. Due to this, the task of this paper was to investigate the influence of MQTT-based architecture on data delivery process in IoT system and analyze the impact of it to the resilience and overall stability of the such system performance.

The paper is organized as follows. Section 2 describes the vulnerabilities of IoT system on the basis of MQTT publish/subscribe architecture. The details of authors' created model for a smart house, based on interoperability between different Internet of Things systems, the investigations and results along with the insights for the resilience of Internet of Things systems, where communication is performed on MQTT publish/subscribe method are presented in Section 3. Section 4 gives the conclusions.

2. BASIC CONCEPTS OF MQTT AND VULNERABILITY OF IT BASED SYSTEM

MQTT is mostly preferred in such networks, where connectivity between the network devices should be as simple as possible. In this case, it's usedness is mostly desirable in IoT applications. This protocol was created on the top of TCP/IP with the ability to increase the reliability of the vulnerable wireless links.

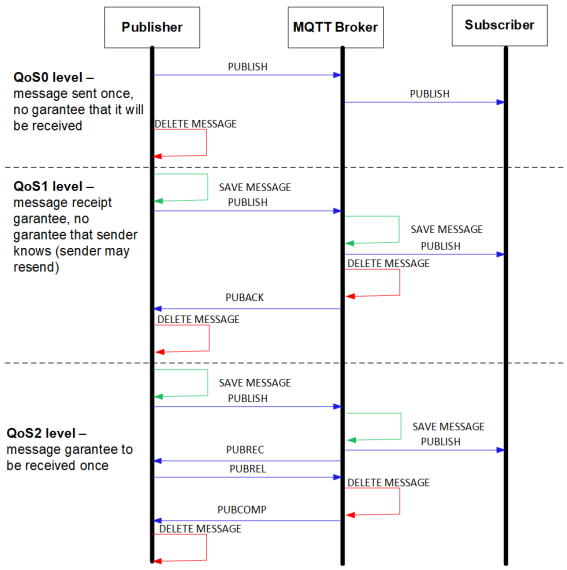

Figure 2. MQTT QoS levels [modified from [5]]

The demand for a reliable delivery of a data from sender to receiver should be satisfied with the different levels of QoS (Quality of Service), as it is a part of MQTT specification. MQTT uses QoS0, QoS1 and QoS2 levels (see Figure 2). These levels should be implemented in the MQTT Broker's side. However, it means that MQTT QoS can impact a higher resilience in MQTT broker, but it doesn't mean a higher resilient in sender or receiver sides. Also, centralized MQTT broker can limit a scale of a connected devices on a network. The data delivery process in MQTT-based IoT systems can be affected of many disruptions, caused by a damage or failures in a publisher's side, lost communication over a wireless link, delay or low bandwidth of a data transmission, subscriber can be overloaded with a received data due to too high data frequency on subscribed topics or cyber-attacks [6-8] and *etc.* Due to this, it is still an open question, how the different MQTT QoS levels can impact the data delivery in Internet of Things systems and the resilience of the whole system performance.

3. SIMULATION OF DATA DELIVERY PROCESS AND RESULTS

In relation with the problems, described above, the authors created a model of a smart house, based on interoperability between different Internet of Things systems. The graphic structure of designed smart house is shown in the Figure 3. The detailed architecture of MQTT-based IoT systems in this house is presented in Figure 4. Communication between nodes in IoT systems was based on MQTT communication protocol.

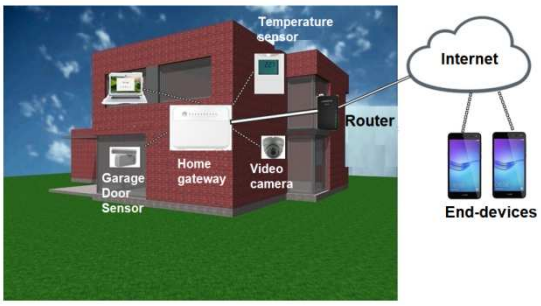

Figure 3. Graphical view of designed smart house

A network simulation tool *Cisco Packet Tracer 7*, *CloudMQTT* (as globally distributed MQTT broker) and open source *Mosquitto* software was used for the investigations. The authors investigated, how the different QoS levels (QoS0, QoS1 and QoS2) of MQTT protocol influence the data delivery process on Internet of Things system and what impact it has to the resilience and overall stability of the system performance. The investigations were done by sending data from a publisher to a subscriber using three different MQTT QoS levels. The results of these investigations are presented in Figures 5-7.

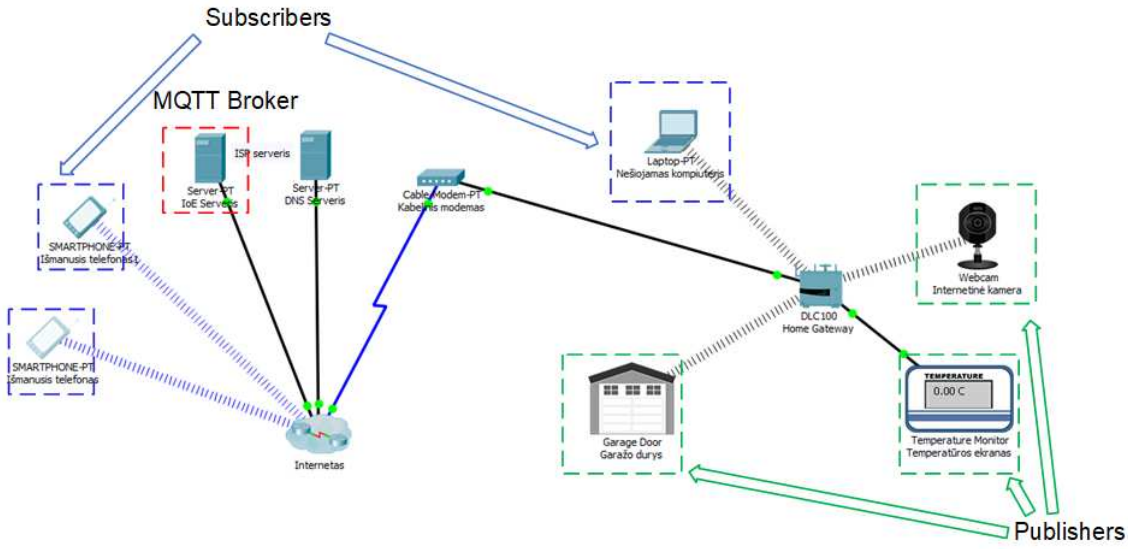

Figure 4. Detailed architecture of IoT systems in designed smart house

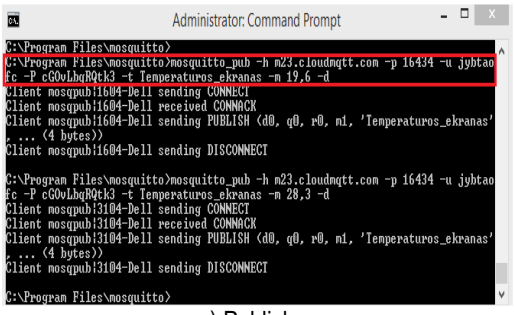

a) Publisher

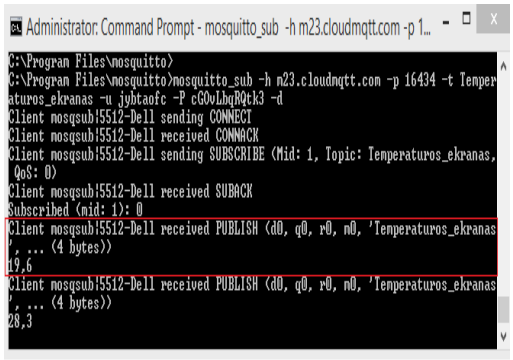

b) Subscriber

Figure 5. Data delivery process using MQTT QoS0

At the beginning of the command (Fig. 5 a)) the *Mosquitto* certificate is assigned to the device that orders to receive information on the desired topic is entered as "*mosquitto_sub*", and the device, that sends the information as "*mosquitto_pub*". Other marks in the command:

-h: *CloudMQTT* server located online;
-p: the port number on server;
-u: the login name;
-P: the login password;

-t: the title of the topic, according to which the sender can send data, and the recipient must subscribe to the relevant topic in order to receive that data;

-m: a message that can only be sent by the sender - in this case, mosquitto_pub (publisher) - and received only by those devices that are subscribed to receive messages for relevant topics;

-d: the function enables the ability to see the sending information;

-q: quality of service (QoS). At the lowest level, it does not need to be specified, but to QoS1 or QoS2 it should be specified.

The Fig. 5 b) indicates, that the subscriber receives the data from MQTT broker according to requirements for the publishing and the message size is displayed as well.

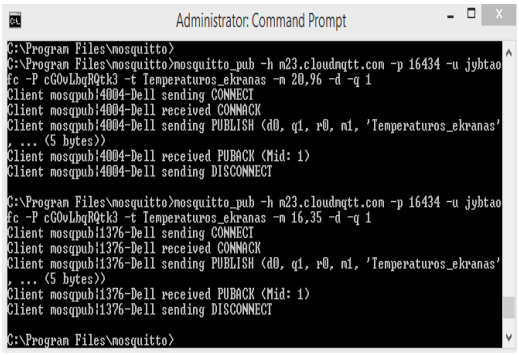

a) Publisher

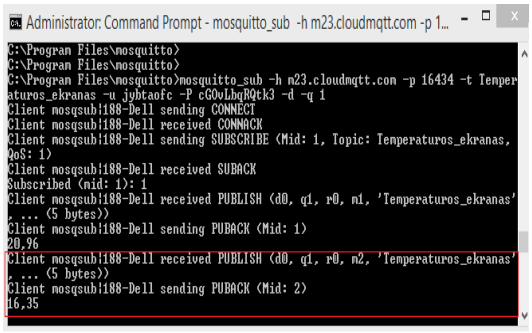

b) Subscriber

Figure 6. Data delivery process using MQTT QoS1

Figure 6 shows the differences on the data delivery process in comparison with MQTT QoS0. It could be seen, that different QoS level is specified as *q1.* Moreover, QoS1 gives one step to a confirmation, that the receiver received the data from MQTT broker (in contrast to QoS0). However, it doesn't mean, that the data couldn't be lost over the delivery process. In contrast to it, if QoS2 level is used, the data cannot be lost, as it allows to have 3 steps to the confirmation of a received data (Fig. 7) or re-ask to send it again.

Although QoS0 is the most unreliable, it can be used in cases where large data flows are sent and the communication between sender and receiver is very strong, but it is not important whether any part of the data can be lost. QoS1 can guarantee the confirmation of a received data, but it has no avoidance of a data duplication. That means, if the receiver sends a "PUBACK" message not in time because of the increased device's delay, the MQTT broker may repeat the sending of the message, causing the receiver to receive too much unnecessary data. And this could affect the stability of the IoT system's performance.

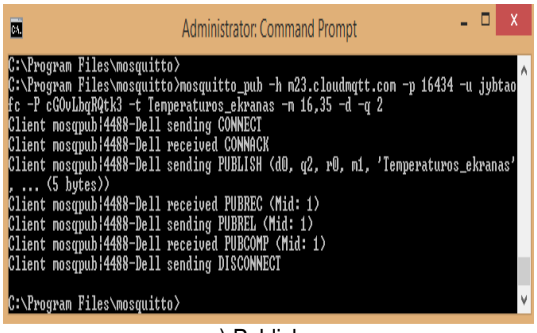

a) Publisher

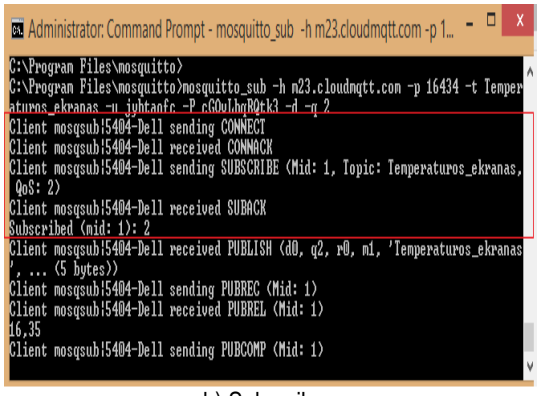

b) Subscriber

Figure 7. Data delivery process using MQTT QoS2

The lack of QoS2 is different than QoS1 or QoS0. Since it ensures that data reaches the receiver and the whole communication process has a possibility to re-ask data from MQTT broker in several times more than in QoS1, the entire data will be sent much longer than using other levels of MQTT quality.

Figure 8 shows the authors' insights based on the results of the investigations for the resilience of Internet of Things systems, where communication is performed on MQTT publish/subscribe method.

The higher QoS level is implemented in IoT endpoints, the more reliable delivery process will be achieved, since QoS0 does not receive any response about receipt of the data, while QoS1 receives an answer that the data has successfully reached the recipient and QoS2 gives even more - the opportunity to retransmit the data. The functioning of Internet Things system is most reliable and resilient at MQTT QoS2 level, since this quality level not only ensures the reception of the data, but also its repetition, while at other QoS levels, devices cannot guarantee that data will not be lost, what would affect the stability of the entire system's per-

formance, as the IoT devices may not perform the required functions.

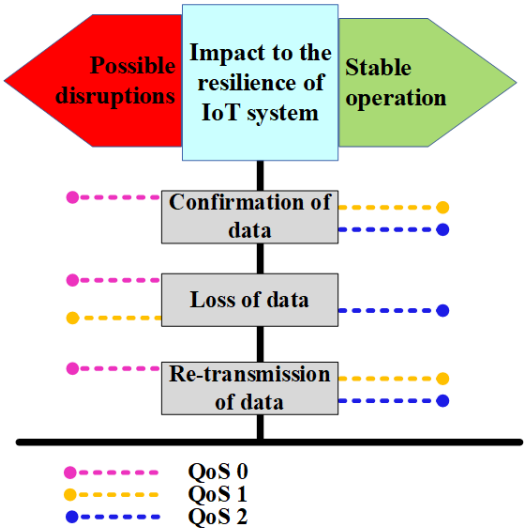

Figure 8. Impact to the resilience of MQTT-based IoT system

4. CONCLUSIONS

The reached results showed, that:

1) the higher QoS level is implemented in IoT endpoints, the more reliable delivery process will be achieved.

2) the functioning of Internet Things system is most reliable and stable at MQTT QoS2 level.

ACKNOWLEDGMENT

This paper is based upon work from COST Action CA15127 ("Resilient communication services protecting end-user applications from disaster-based failures — RECODIS") supported by COST (European Cooperation in Science and Technology).

References

[1] *M. Wollschlaeger, T. Sauter, and J. Jasperneite, "The future of industrial communication: Automation networks in the era of the internet of things and industry 4.0," IEEE Industrial Electronics Magazine, vol. 11, no. 1, pp. 17–27, 2017.*

[2] *P. P. Ray, "A survey on internet of things architectures," Journal of King Saud University-Computer and Information Sciences, vol. 30, no. 3, pp. 291–319, 2018.*

[3] *K. Angrishi, "Turning internet of things (iot) into internet of vulnerabilities (iov): Iot botnets," arXiv preprint arXiv:1702.03681, 2017.*

[4] *M. Version, "3.1. 1 oasis standard, 29 October 2014," 2017.*

[5] *Stanford-Clark, A., Hong Linh Truong. MQTT For Sensor Networks (MQTT-SN). In Protocol Specification, vers. 1.2, pp. 1-28, Nov., 2013.*

[6] *S. N. Firdous, Z. Baig, C. Valli, and A. Ibrahim, "Modelling and evaluation of malicious attacks against the iot mqtt protocol," in Internet of Things (iThings) and IEEE Green Computing and Communications (GreenCom) and IEEE Cyber, Physical and Social Computing (CPSCom) and IEEE Smart Data (SmartData), 2017 IEEE International Conference on, pp. 748–755, IEEE, 2017.*

[7] *R. Atmoko, R. Riantini, and M. Hasin, "Iot real time data acquisition using mqtt protocol," in Journal of Physics: Conference Series, vol. 853, p. 012003, IOP Publishing, 2017.*

[8] *S. Lee, H. Kim, D.-k. Hong, and H. Ju, "Correlation analysis of mqtt loss and delay according to qos level," in Information Networking (ICOIN), 2013 International Conference on, pp. 714–717, IEEE, 2013.*

ON THE ESTIMATION OF MAGNETOTHERAPY CURATIVE SESSIONS EFFECTS

N. Ampilova, F. Uvarichev, I. Soloviev

St. Petersburg State University, Comp. Sci. Dept.
n.ampilova@spbu.ru, ufispb@gmail.com, i.soloviev@spbu.ru

Abstract

Low frequency and low intensities magnetic and electric fields are used in physiotherapy for a long time. But due to the fact that the action of these fields on living tissues is very complicated and at the moment insufficiently studied, nowadays there is no simple method to measure their curative effect. In practrice the natural way of investigations is the experimental one: to observe the state of a patient during curative sessions and collect statistical data. We propose to combine practical approach with the study of processes in external environment when low intensity magnetic fields act. With this purpose we calculate and visualize the trajectories of ions in electromagnetic field generated by a magnetotherapy device. Such an approach leads to obtaining a series of images that show trajectories depending of the choice of the parameters of the device. That results in visual representation of typical phase portraits generated by the applied mathematical model. Visual perception helps to compare the number of procedures, parameters of the used device and the changing of patient state, and thus to form an expert knowledge in this area.

1. INTRODUCTION

For better understanding of the problem of effects of low intensity magnetic field on living organism one may use mathematical and computer modeling. The most simple model is a distribution of intensities of magnetic field generated by a coil. This model is based on the superposition principle: in this case due to constant current value the induction and self-induction are supposed to be negligible quantities and the common magnetic field is the sum of the fields generated by the contours of a coil. For several coils the magnetic field is the sum over all the coils. What is important that we really perform calculation for non-uniform magnetic field, in other words for fields changing in the space. The case of different position of coils in 3D and visualization of the resulting field were considered in [1,3,4], where the results of calculation were applied to a special magnetotherapy device — “magneto-bed” which is actively used in medical practice.

The next step in the studying processes in an environment when electromagnetic field acts is to consider the model of the movement of charged particles (ions or cations) in this environment. In the first approximation we may use the model where an ion moves in accordance with the Newton second law, and the Lorentz force acts on it. The problem is to calculate and visualize the trajectories of different ions for given configuration of electric and magnetic fields.

One may assume that the motion is in air environment. However practice shows that the action of magnetic field in mineral water improves the curative effect for patients with diabetes. To model the magnetic field distribution in mineral water we should use the magnetic permeability of this environment in formulas for calculation of magnetic induction. But at the moment we do not know how the permeability depends on mineral water composition. So, to make the problem easier it was assumed that the magnetic permeability of mineral water is approximately the same as of ordinary water, which is a natural assumption in the frame of given mathematical model.

Thus, to model an ion motion we used the method of calculation of the magnetic field of a coil, which is described above. The field is calculated in the points of a space grid. We also approximated differential equations of the ion movement by discrete ones by using a second order difference scheme. If a next point of trajectory is not in the grid of points for which values of magnetic field are calculated, a linear interpolation is performed to calculate the value of the field in the point. Various cases of configuration of electrical and magnetic fields were modelled, in particular periodic effects of the fields. In this regime there are two cases — commensurable and incommensurable frequencies. The most complex phase portraits were obtained for incommensurable ones.

It should be noted that the proposed difference scheme leads to the solving linear system by Cramer's method, which is simpler than numerical integration by the Runge-Kutta method. All calculations were compared with calculation in MATLAB package. The results are similar. All the experiments were applied to a special device used in clinics.

Such a method allows us to select a set of parameters and obtain visualization of ion movement. For visualization we used ParaView package and MATLAB. In fact, an imitation model has been designed that may be used for construction some medical devices and choice the most appropriate parameters. The model includes performing the calculations, saving obtained data in files of a required format, call the ParaView to visualize magnetic field or combine visualization of the field and the ion trajectory.

This approach may help to estimate the effectiveness of the magnetotherapy by monitoring the patient state and comparing obtained data with the parameters of the device. Visualization makes this analysis more clear. Moreover, in doing so we model the processes in the external environment, where electromagnetic field acts, and this study contributes to a better comprehension of processes in internal environment – living tissue. This is practical and useful method.

To develop this technique we have to consider more complex models which take into account the interaction between particles and the structure of the environment. There are a lot of problems including physical and chemical hydrodynamics, electrochemistry, biophysics. The questions concerning the influence of geomagnetic and artificial magnetic fields on transfer processes in aqueous media such as electrolytes and biological objects are discussed in the monography [2]. Our future investigations suggest a more detailed study of this subject.

2. MATHEMATICAL MODEL DESCRIPTION

The detailed derivation of equations for the movement of charged particle in electrical and magnetic fields is given in many textbooks, for example in [5]. We describe them briefly. Consider a charged particle with a charge q and mass m. Let $\overrightarrow{E}(x,y,z,t)$ be the intensity of electrical field in the point (x,y,z) at the moment t, and $\vec{B}(x,y,z,t)$ be the magnetic field induction. The force acting the ion in electrical field is equal to $q\vec{E}$, and the Lorentz force in magnetic field equals $q\vec{v}\times\vec{B}$. Then writing the second law of Newton we obtain $m\frac{d\vec{v}}{dt}=q(\vec{E}+\vec{v}\times\vec{B})$. Assuming that $\vec{B}$ is co-directed with Oz, and hence $B_z=B, B_x=B_y=0$, we obtain the following system of equations

$$\begin{cases} m\ddot{x}=q\big(E(x,y,z,t)\sin\gamma\cos\beta+\dot{y}\,B(x,y,z,t)\big)\\ m\ddot{y}=q(E(x,y,z,t)\sin\gamma\sin\beta-\dot{x}B(x,y,z,t)) \\ m\ddot{z}=qE(x,y,z,t)\cos\gamma. \end{cases} \quad (1)$$

The positions of vectors electric and magnetic fields are illustrated in Fig.1

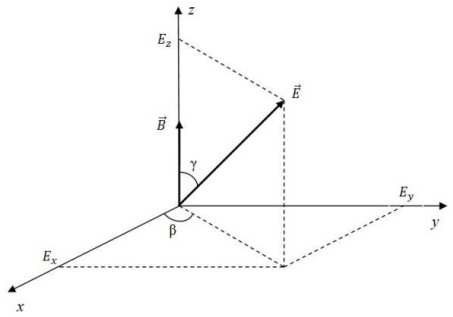

Figure 1. The disposition of vectors $\vec{B}$ and $\vec{E}$

It is well known that system (1) is integrable if there is no electrical field and magnetic field is uniform and constant. Then the trajectory of an ion is screw line. But for non-integrable cases we have to apply approximate calculations. We use the second order difference system. Let $[t_0,T]$ be the time interval on which a trajectory is calculated, $t_i=t_0+ih, i=0,\dots n, x(t_i)=x_i, y(t_i)=y_i,\quad z(t_i)=z_i$. Assume that

$$\ddot{x}\approx\frac{x_{i+1}-2x_i+x_{i-1}}{h^2},$$

$$\ddot{y}\approx\frac{y_{i+1}-2y_i+y_{i-1}}{h^2}, \quad (2)$$

$$\ddot{z}\approx\frac{z_{i+1}-2z_i+z_{i-1}}{h^2},$$

and

$$\dot{x}\approx\frac{x_{i+1}-x_{i-1}}{2h},$$

$$\dot{y}\approx\frac{y_{i+1}-y_{i-1}}{2h}, \dot{z}\approx\frac{z_{i+1}-z_{i-1}}{2h} \quad (3)$$

Substituting (2) and (3) in (1) we obtain the second order system of difference equations

$$\begin{cases} x_{i+1} - K_i y_{i+1} = 2x_i - x_{i-1} - K_i y_{i-1} + L_i \sin\gamma \cos\beta \\ K_i x_{i+1} + y_{i+1} = 2y_i - y_{i-1} + K_i x_{i-1} + L_i \sin\gamma \sin\beta \\ z_{i+1} = 2z_i - z_{i-1} + L_i \cos\gamma, \end{cases} \quad (4)$$

where $K_i = \frac{qh}{2m} B(x_i, y_i, z_i)$ if current is constant, and $K_i = \frac{qh}{2m} B \cos\omega t_i$ in the case of variable current with frequency ω. By analogy $L_i = \frac{qh^2}{m} E(x_i, y_i, z_i)$, if electrical field depends on the point, and $L_i = \frac{qh^2}{m} E \cos\omega t_i$ for periodic field. The system (4) is linear, coordinates of z are found independently from x and y, and on every step x_{i+1}, y_{i+1} may be calculated by Cramer method, because $\Delta = 1 + K_i^2 \neq 0$.

3. EXPERIMENTS AND RESULTS

We applied the implemented program to model ion trajectories both for arbitrary value of parameters and in a special magnetotherapy device. The device has two coils which are active simultaneously. One may add electric field. Magnetic and electrical fields may be periodic with commensurable and incommensurable frequences.

3.1. Results for the device

Device parameters are the following: coils have external radius 58 mm, height 34 mm; current intensity is 3A, the number of turns is 20, the number of windings is 25. The size of the region (in mm) is 600x300x500, the size of a cell of the lattice (in mm), where magnetic field is calculated is 4x4x4, the step on time *h* (in sec) is 10^{-6}.

The beginning of the first coil has coordinates (0, 150, 250), the axis direction is (1, 0, 0). The beginning of the second coil has coordinates (600, 150, 250), the axis direction is (-1, 0, 0).

Figure 2. Magnetotherapy device

The experiments were performed for various types of ions and combination of magnetic and electrical fields.

3.1.1. Natrium ion in magnetic field

Natrium ion has mass m=3.817$*10^{-23}g$, charge q=1 . We take $B = 10^{-3}T$. Calculate the ion trajectory with initial data

$(x_0, y_0, z_0) = (100,150,250)$,
$(x_1, y_1, z_1) = (100,150,250.01)$

when only magnetic field generated by 2 coils acts.

Calculation was performed for 200000 points.

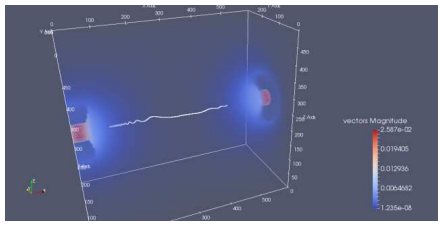

Figure 3. The trajectory of natrium ion in magnetic field

3.1.2. Natrium ion trajectory when magnetic and electrical fields act

Modify the previous example and add electrical field. Assume that vector $\vec{E}$ has coordinates (0.1, 0, 0) and
$(x_0, y_0, z_0) = (x_1, y_1, z_1) = (100,150,240)$.

The number of points is 3709.

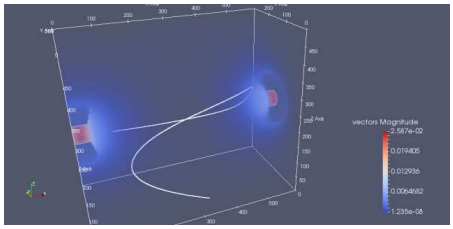

Figure 4. The trajectory of natrium ion in magnetic and electrical fields

3.1.3. Natrium ion in periodic magnetic field

Now we consider periodic magnetic field with frequency 10 Hz,
(x_0, y_0, z_0) =(100,150,250), $(x_1, y_1, z_1) = (100,150,250.01)$.

The number of points is 73688.

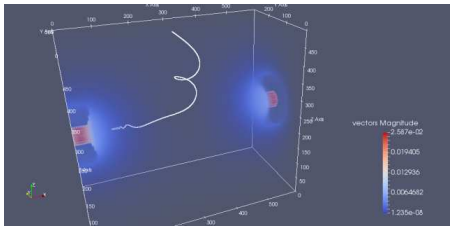

Figure 5. The trajectory of natrium ion in periodic magnetic field

3.1.4. Sulfate ion in magnetic field

Consider the motion of sulfate ion with mass m=16*10^{-23}g, q=-2 in magnetic field.

The number of points is 200000.

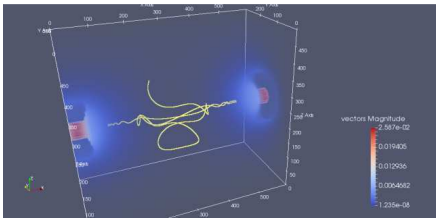

Figure 6. The trajectory of sulfate ion in magnetic field

3.2. Natrium ion in periodic magnetic and electrical fields

Now we consider periodic magnetic field with frequency 200π, and electric field with frequency 80π. The number of points is 150000.

On Fig.7 we present the results of calculations performed in accordance with system (4).

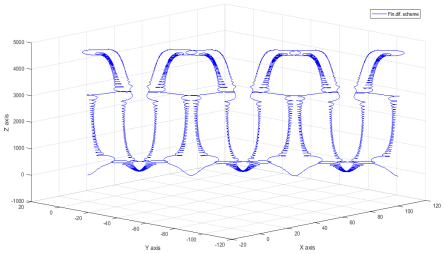

Figure 7. Natrium ion in periodic fields: commensurable frequences

The next picture shows the results when the frequency of magnetic field is 200π, and the frequency of electrical field is $2\pi \cdot 20e$. Note that such a motion we may observe on rather long distance on z-coordinate (near 6 m). Hence in real device we would see only small part of the trajectory and the difference between these cases will not be considerable for visual perception.

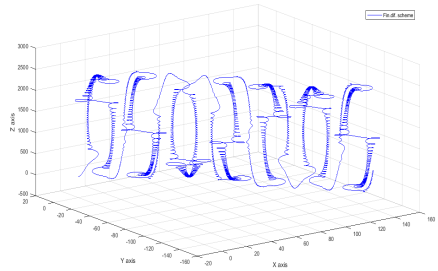

Figure 8. Natrium ion in periodic fields: incommensurable frequences

4. CONCLUSION

The designed and implemented program is the imitation model for calculation of distribution of electric and magnetic fields and the motion of ions in these fields in magnetotherapy devices. It allows us to calculate trajectories and visualize the typical trajectories calculated for different ions. The obtained set of images may help in matching of given parameters to the results of monitoring the patient state. The studying the state of environment under action of magnetic field requires to take into account not only an ion motion, but also the interaction between particles, boundary condition and other. This problem is the subject of our future investigations.

5. ACKNOWLEDGMENTS

This work was partially supported by the grant Erasmus + International Mobility (KA107) / National Technical University of Athens — St. Petersburg State University.

The authors would like to thank Prof. D. Dimitrov from Technical University of Sofia for the problem state and many fruitful discussions.

References

[1] *N. Ampilova, D. Dimitrov, B. Kudrin, "Mathematical modeling of low frequency magnetic field in systems for magnetotherapy ", Proc. 8 Int. Conf. CEMA13, 17-19 Oct. 2013, Sofia, Bulgaria, pp. 48-51.*

[2] *E. Gak. "Magnetic fields and aqueous electrolites in nature, scientific research and technologies", St. Petersburg, 2013. (in Russian)*

[3] *B. Kudrin, I. Soloviev, "On interpolation methods of low frequency magnetic field in systems for magnetotherapy", Proc. 9 Int. Conf. CEMA14, 16-18 Oct. 2014, Sofia, Bulgaria. KING 2001, pp.154-157, ISSN 1314-2100.*

[4] *B. Kudrin, V. Nikolov, "On a visualization of low-frequency magnetic field in magnetotherapy", Journal of Applied Electromagnetism , vol. 18, no. 2(2016), pp. 14-22.*

[5] *B. Lennert, "Dynamics of charged particles", North Holland, 2004.*

AUTHOR INDEX